

Radiation effects in oxides used in nuclear applications

by

P. Jegadeesan

Enrolment No.: PHYS 02 2012 04 013

Indira Gandhi Centre for Atomic Research, Kalpakkam, India.

A thesis submitted to

The Board of Studies in Physical Sciences

In partial fulfillment of requirements for the Degree of

**DOCTOR OF PHILOSOPHY
of
HOMI BHABHA NATIONAL INSTITUTE**

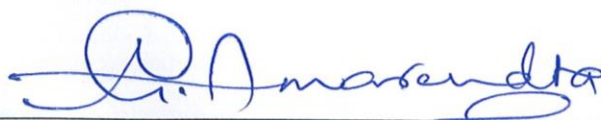


August, 2019

Homi Bhabha National Institute

Recommendations of the Viva Voce Committee

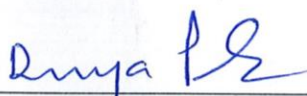
As members of the Viva Voce Committee, we certify that we have read the dissertation prepared by P. Jegadeesan entitled "Radiation effects in oxides used in nuclear applications" and recommend that it may be accepted as fulfilling the thesis requirement for the award of Degree of Doctor of Philosophy.



Nov 5, 2019

Chairman: **Dr. G. Amarendra**

Date:



5/11/19

Guide/ Convener: **Dr. B.K. Panigrahi**

Date:



5/11/19

External Examiner: **Prof. D.K. Avasthi**

Date:



Member 1: **Dr. Sharat Chandra**

Date:

5/11/19



5/11/19

Member 2: **Dr. Arup Dasgupta**

Date:

Final approval and acceptance of this thesis is contingent upon the candidate's submission of the final copies of the thesis to HBNI.

I hereby certify that, I have read this thesis prepared under my direction and recommend that it may be accepted as fulfilling the thesis requirement.

Date: 5/11/19

Place: Kalpakkam



Dr. B. K. Panigrahi

(Guide)

Statement by Author

This dissertation has been submitted in partial fulfillment of requirements for an advanced degree at Homi Bhabha National Institute (HBNI) and is deposited in the Library to be made available to borrowers under rules of the HBNI.

Brief quotations from this dissertation are allowable without special permission, provided that accurate acknowledgement of source is made. Requests for permission for extended quotation from or reproduction of this manuscript in whole or in part may be granted by the Competent Authority of HBNI when in his or her judgment the proposed use of the material is in the interests of scholarship. In all other instances, however, permission must be obtained from the author.

Date:

5/11/19

Place:

Kalpakkam



(P. Jegadeesan)

Declaration

I, hereby declare that the investigation presented in the thesis has been carried out by me. The work is original and has not been submitted earlier as a whole or in part for a degree / diploma at this or any other Institution / University.


(P. Jegadeesan)

List of Publications

(a) Journal

1. Aggregation and ordering of helium in thoria
P. Jegadeesan, S. Amirthapandian, B.K. Panigrahi, Gurpreet Kaur, D. Sanjay Kumar, P. Magudapathy, K. Ananthasivan
Journal of Alloys and Compounds **743** (2018) 196-202
2. Characterization of M-O bonds in $Y_2Ti_2O_7$ and Y_2TiO_5 with EELS
P. Jegadeesan, S. Amirthapandian, Gurpreet Kaur, Sharat Chandra, B.K. Panigrahi
Physica Status Solidi B, **252** (2015) 206–211
3. Ion irradiation induced crystallization in iron phosphate glass – TEM investigations
P. Jegadeesan, S. Amirthapandian, Kitheri Joseph, C. David, B.K. Panigrahi, K.V. Govindan Kutty
Advanced Materials Letters, **6** (2015) 224–227

(b) Conferences:

1. Formation of faceted krypton bubble in ThO_2
P. Jegadeesan, D. Sanjay Kumar, S. Amirthapandian, P. Magudapathy, B.K. Panigrahi, K. Ananthasivan
International Conference on Electron Microscopy (EMSI-2017), Bhubaneswar, India, July 18-20 July, 2018
2. Ion irradiation effects in thoria – EELS analysis
P. Jegadeesan, S. Amirthapandian, P. Magudapathy, D.K. Avasti, K. Ananthasivan and B.K. Panigrahi
International Conference on Electron Microscopy and Allied Techniques (EMSI-2017), Mahabalipuram, Tamilnadu, India, July 17-19, 2017
3. Low energy krypton ion irradiation effects in yttrium titanates – TEM study
P. Jegadeesan, S. Amirthapandian, P. Magudapathy, B.K. Panigrahi
International conference on Ion Beams in Materials Engineering and Characterizations (IBMEC-2016), Inter-University Accelerator Centre, New Delhi, September 28-October 1, 2016
4. Effects of helium ion irradiation in thoria,
P. Jegadeesan, S. Amirthapandian, D. Sanjay Kumar, P. Magudapathy, K. Ananthasivan, B.K. Panigrahi,
International conference on electron microscopy (EMSI-2016), IIT-BHU, Varanasi, June 2-4, 2016.

5. A comparison between experiment and DFT calculation - EELS of $Y_2Ti_2O_7$ and Y_2TiO_5
P. Jegadeesan, S. Amirthapandian, Gurpreet Kaur, Sharat Chandra, B.K. Panigrahi
Indo-UK Workshop on Modeling and Simulation of Safety and Materials for Nuclear Applications (MSMNA-2015) Kalpakkam, India, December 16-17, 2015
6. Electron microscopy studies on the effect of ion irradiation in glasses – nuclear waste immobilization materials
S. Amirthapandian, **P. Jegadeesan**, C. David, Kitheri Joseph, J.G. Shah, R. Asuvatharaman, B.K. Panigrahi
18th International Conference on Radiation Effects in Insulators (REI-18) Jaipur, India, October 26-31, 2015
7. Electron microscopic investigations on ion irradiated sodium borosilicate glass
P. Jegadeesan, J.G. Shah, S. Amirthapandian, C. David, B.K. Panigrahi
International Conference on Electron Microscopy (EMSI-2015), Mumbai, July 8-10, 2015
8. TEM investigations on ion irradiated iron phosphate glass
P. Jegadeesan, S. Amirthapandian, Kitheri Joseph, C. David, B.K. Panigrahi, K.V. Govindan Kutty,
International Conference on Swift Heavy Ions in Materials Engineering and Characterisation (SHIMEC-2014) Inter-University Accelerator Centre, New Delhi, October 14-17, 2014
9. Electron energy loss spectra of $Y_2Ti_2O_7$ and Y_2TiO_5 : A comparative study between experiments and first principle calculations,
P. Jegadeesan, S. Amirthapandian, Gurpreet Kaur, Sharat Chandra, and B.K. Panigrahi
International Union of Materials Research Societies – International Conference in Asia – 2013 (IUMRS-ICA-2013), Indian Institute of Science, Bangalore, December 16-20, 2013



P. Jegadeesan

I dedicate this thesis to my life partner Mehala.

Acknowledgements

I take this opportunity to thank my guide Dr. B.K. Panigrahi. He has sensibly designed my research program with due care, and amidst his busy schedule, he did have a constant vigil on my research progress. His technical interpretations on the experimental data and the corrections in manuscripts were often very short but always they were the closing remark and the final word on the issue. His profile has grown a lot during the last few years. But, I find the difference only in getting his appointment. His attitude towards research and his personal approach remained as enjoyable as it was earlier.

I am very much grateful to the dedication and enthusiasm shown by Dr. S. Amirthapandian to finish my Ph.D. He literally assumed the role of guide throughout my research career and helped to wade through the tough times during publishing research articles. He directed my thought process all the way while writing thesis. Apart from these technical assistance, I am indebted to him, as my friend, for taking up the tiresome job of visiting Indore to take XAS measurements for my thesis work.

I thank Dr. Sharat Chandra and Dr. Gurpreet Kaur for introducing me to Materials Studio software package and VASP code. They were my reference book for any doubts related to DFT calculations. I gratefully acknowledge the technical guidance of Dr. Sharat Chandra while writing manuscripts and his painstaking efforts on correcting the manuscripts. I am really lucky; he is a member of my doctoral committee.

I thank our senior colleague Mr. P. Magudapathy, for carrying out number of irradiation and XRD measurements. He has shared many technical details of the equipment and the knacks of the experiments; he knows the tricks of the trade.

I express special thanks to Dr. Kitheri Joseph for providing me with the special category of glass specimen, the IPG, and to Dr. K. Ananthasivan and Dr. D. Sanjay Kumar, for providing thoria sample. I gratefully acknowledge the efforts put by Dr. S. Ilango and Mrs. Sunita while repeating the GIXRD measurements. I thank Dr. T.R. Ravindran for his help in understanding the Raman spectra. I thank Dr. D.K. Shukla, Dr. Mukul Gupta for interpreting XAS.

I thank my Section Head Dr.C. David for valuable technical discussions and encouragement and for ensuring conducive environment. I thank all my section colleagues for their cooperation.

I sincerely thank Dr. B.V.R. Tata, the former chairman of the doctoral committee and Dr. G. Amarendra, the present chairman, for their encouragement and constant support.

P. Jegadeesan

Abstract

Oxide materials find applications throughout the nuclear fuel cycle, from actinide-bearing ores and commercial reactor fuels to wasteforms for radionuclide disposal. Many of the critically important materials used in the nuclear industry are oxide based ceramics, like the oxide fuel materials (e.g. urania, thoria), the oxide nanodispersoids (e.g. yttrium titanates in ferritic steel) used for strengthening the metallic structural materials and the glasses used for the disposal of nuclear wastes (e.g. borosilicate glass, iron phosphate glass).

The predominant fuel materials like urania, urania-plutonia mixed oxide fuel (PuO_2/UO_2), and the alternate fuel thoria, are all oxide based ceramic materials. Oxides also find application in strengthening the reactor structural materials. The ‘oxide dispersion strengthened’ (ODS) steels are the candidate structural material proposed for future reactors. These oxide nanodispersoids (yttrium titanates particles) enhances the mechanical strength of the ODS steel and improve its radiation resistance and creep resistance. Oxides find application in the immobilization and the disposal of nuclear wastes also. Oxide based glasses such as borosilicate glass (BSG) and iron phosphate glass (IPG), are used as wasteforms in the nuclear industry. Particularly, IPG is being proposed as the appropriate glass matrix for the disposal of fast reactor wastes.

The radiation response of oxide based ceramics are very different from metals. The fundamental difference is in the nature of bonds and crystal structure. Metals and alloys exist in simple crystal structures like cubic or hexagonal, whereas ceramics have complex crystal structures such as fluorite or pyrochlore. Moreover, the complex crystal structures consist of many sublattices populated by atoms with different masses and valency. So, ceramics show significant difference in their response to radiation, in terms of defect production, defect aggregation and defect recovery.

The present thesis deals with the studies on the radiation stability of oxide ceramics: (i) thorium dioxide or thoria (ThO_2), a nuclear fuel material, (ii) yttrium titanates ($\text{Y}_2\text{Ti}_2\text{O}_7$ and Y_2TiO_5), the oxide-dispersoids used for strengthening the structural material, (iii) Iron Phosphate Glass (IPG), the material proposed for the disposal of high level nuclear waste from the fast reactors.

The behaviour of the inert gas helium inside the oxide fuel thoria was studied by implanting helium using low energy beam (100 keV He^+). The changes in the microstructure were analysed using grazing incidence X-ray diffraction (GIXRD) and transmission electron microscopy (TEM). Both the experiments showed that there is lattice expansion (1.07 %) in isolated nanometric regions in the surface of the sample upon irradiation. First principle calculations showed that the energetics prefer aggregation and ordering of helium in the octahedral interstitial sites in thoria lattice, and the ordered aggregation results in lattice expansion of 1.25%; this value is in agreement with experiments. Thus, the experiments and calculations confirm that the lattice expansion is due to the ordering of helium atoms in the octahedral interstitial sites of thoria.

The stability of both the yttrium titanates were compared by irradiating both the oxide samples with 70 keV Kr^+ ions at room temperature. TEM results showed the presence of stacking faults in $\text{Y}_2\text{Ti}_2\text{O}_7$ and faceted bubbles of krypton in Y_2TiO_5 , upon irradiation at room temperature. Further, the nature and strength of the different Metal-Oxygen bonds in both these oxides were characterized by comparing the pre-edge features in O K-edge in EELS and using the electron charge densities calculated using DFT. The pre-edge features in the O-K edge of transition metal (TM) oxides manifest the effect of crystal field splitting in the Ti $3d$ orbital. EELS analysis showed that the overlap of Ti $3d$ orbital and O $2p$ orbital is less dominant in Y_2TiO_5 compared to $\text{Y}_2\text{Ti}_2\text{O}_7$. The EELS and DFT results showed that Ti-O bonds in $\text{Y}_2\text{Ti}_2\text{O}_7$ is more covalent compared to Y_2TiO_5 and Ti-O bonds are

more covalent than Y-O bonds in both the yttrium titanates. Hence it is suggested that $\text{Y}_2\text{Ti}_2\text{O}_7$ is better radiation resistant than Y_2TiO_5 .

In the case of iron phosphate glass (IPG), irradiation induced relaxation processes were studied by irradiating IPG with 4 MeV O^+ (self) ions. TEM images and electron diffraction patterns showed the formation of nanocrystals of $\text{Fe}_4(\text{P}_2\text{O}_7)_3$, $\text{Fe}(\text{PO}_3)_3$ and P_2O_5 in the glass sample upon irradiation. The mechanism of crystallization was explained based on stress driven crystallization mechanism. Changes in the charge state of Fe atom upon ion irradiation is analysed using X-ray absorption spectra. The analysis of O K-edge and Fe L_{23} -edge clearly showed that the concentration of Fe^{2+} has increased and the concentration of Fe^{3+} has decreased upon 4 MeV O^+ irradiation. The rise in the population of Fe^{2+} implies that the *glass phase* of $\text{Fe}_3(\text{P}_2\text{O}_7)_2$ has increased in the glass matrix upon irradiation. The rise in the population of Fe^{2+} increases the viscosity of IPG, which in turn increases the glass forming ability.

Table of Contents

List of Publications	iii
Acknowledgements	vi
Abstract	viii
Table of Contents.....	xi
List of Figures	xiv
List of tables	xviii

Chapter 1 **Radiation damage in nuclear oxide materials - A**

brief review1

1.1. Motivation.....	1
1.2. Ion-solid interactions.....	4
1.2.1. Energy loss mechanisms – Stopping of ions in solids.....	4
1.2.1.1. Electronic stopping	5
1.2.1.2. Nuclear stopping	6
1.2.2. Ion Range and Straggling in solid	7
1.2.3. Sputtering.....	8
1.2.4. Radiation damage.....	9
1.3. Ion irradiation effects in materials.....	12
1.3.1. Effects of low energy ion irradiation – nuclear processes	13
1.3.2. Irradiation effects due to electronic energy loss	14
1.3.3. Void swelling	16
1.3.4. Ion irradiation induced phase transformations	17
1.3.5. Inert gas bubble formation in materials	20
1.4. Radiation effects in oxide materials.....	22
1.4.1. Radiation effects in oxide based fuel materials.....	22
1.4.2. Radiation response of rare earth titanates.....	25
1.4.3. Radiation damage in oxide glasses used as wasteform.....	27
1.5. Objective and overview of the thesis	30

Chapter 2 **Experimental Techniques.....33**

2.1. Sample preparation methods	33
2.1.1. Solid state reaction method	33
2.1.2. Gel combustion method.....	36
2.1.3. Glass preparation – Melt-Quench method	37
2.2. Accelerator facilities	38

2.2.1.	1.7 MV Tandetron accelerator.....	39
2.2.2.	150 kV ion accelerator	40
2.3.	Diffraction techniques.....	42
2.3.1.	X-ray diffraction	42
2.3.2.	Grazing incidence X-Ray Diffraction	43
2.3.3.	Electron diffraction.....	44
2.4.	Transmission electron microscopy	46
2.4.1.	Energy Dispersive X-ray Spectrometry.....	48
2.4.2.	TEM Sample preparation	48
2.5.	Spectroscopy techniques	48
2.5.1.	Core level spectroscopy techniques	48
2.5.1.1.	X-Ray Absorption Spectroscopy	49
2.5.1.2.	Electron energy loss spectroscopy	50
2.5.2.	Raman spectroscopy	52
2.6.	Computational methods.....	54
2.6.1.	Density Functional Theory	54
2.6.1.1.	Materials Studio - CASTEP	56
2.6.1.2.	Vienna <i>Ab-initio</i> Simulation Package	57
2.6.2.	Molecular Dynamics simulations	58
2.6.3.	CTM4XAS.....	59
2.7.	Summary	60

Chapter 3 Aggregation and ordering of helium in thoria61

3.1.	Introduction.....	61
3.2.	Experimental and computation methods	62
3.2.1.	Sample synthesis.....	62
3.2.2.	Experimental methods	62
3.2.3.	Computation details	64
3.3.	Results.....	66
3.3.1.	XRD analysis.....	66
3.3.2.	TEM analysis.....	68
3.3.3.	DFT calculations	70
3.4.	Discussion.....	74
3.5.	Summary and conclusion	77

Chapter 4 Radiation stability of yttrium titanates79

4.1.	Introduction.....	79
------	-------------------	----

4.2.	Experimental and computational methods	80
4.2.1.	Experimental methods.....	80
4.2.2.	Computational methods	81
4.2.2.1.	Simulation of EEL spectra using DFT	81
4.2.2.2.	Simulation of EEL spectra using CTM4XAS	83
4.2.2.3.	Stacking fault energy calculation	84
4.3.	Results.....	85
4.3.1.	GIXRD analysis	85
4.3.2.	Microstructural analysis – TEM.....	87
4.3.3.	Raman scattering analysis.....	91
4.4.	Characterization of the M-O bonds.....	94
4.4.1.	M-O bonds in $Y_2Ti_2O_7$ and Y_2TiO_5	94
4.4.2.	Analysis of O K-edge and Ti L_{23} edge.....	96
4.4.3.	Electron density difference and Mulliken charge analysis...	101
4.5.	Discussion.....	103
4.6.	Summary and Conclusions	104

Chapter 5 Ion irradiation induced crystallization in iron phosphate glass 106

5.1.	Introduction	106
5.2.	Experimental methods.....	108
5.2.1.	Synthesis of IPG.....	108
5.2.2.	Ion irradiation experiments	108
5.3.	Results.....	109
5.3.1.	GIXRD Analysis.....	109
5.3.2.	TEM analysis of the microstructural changes.....	110
5.3.3.	Analysis of core-level spectra.....	116
5.3.3.1.	O K-edge - XAS and EELS.....	116
5.3.3.2.	Fe L_{23} -edge – XAS and EELS results.....	118
5.4.	Discussion.....	119
5.4.1.	Mechanism of irradiation induced crystallization	119
5.4.2.	Irradiation induced changes in the charge state of Fe	121
5.5.	Summary and conclusion.....	122

Chapter 6 Summary and scope for future work 124

References 128

List of Figures

- Figure 1.1 Schematic illustration of the typical partitioning of energy in between the two energy loss processes (S_n and S_e), as a function of the energy of the incident ion. 5
- Figure 1.2 The schematic representation of (a) the projected range (R_p) and (b) the distribution of implanted atoms, as a function of depth (with, ΔR_p , the straggling). 8
- Figure 1.3 Schematics of cascade regimes (a) single collision regime, (b) linear cascade and (c) thermal spike. 11
- Figure 1.4 Mossbauer spectra from the multilayers of Fe/Ag 85 keV Ar^+ ions (a) at 325 K, ion fluence 3×10^{16} ions/cm² (b) at 110 K, ion fluence of 1×10^{15} ions/cm². 13
- Figure 1.5 TEM images of single ion track in $Gd_2Ti_2O_7$. There is a defect-fluorite shell (Region 1; 1.5 nm thick) that surrounds the amorphous core track (Region 2). (Ref.[34]) 14
- Figure 1.6 Cavities in D9 steel alloys pre-implanted with 100 appm of helium and subsequently implanted with 2.5 MeV Ni^{2+} ions, at (a) 500 °C (b) 550 °C (c) 600 °C (d) 650 °C. The arrows point towards typical cavities. (Ref.[41]) 16
- Figure 1.7 TEM image of an isolated track in an $Fe_{73.5}Nb_{4.5}Cr_5Cu_1B_{16}$ sample irradiated to a fluence of 1×10^{10} cm⁻² with 30 MeV C_{60} . A deformation band which exits toward the sample edge is visible. 19
- Figure 1.8 Bright-field TEM images showing the bubble and the oxide particle complexes in ferritic ODS alloy (PM2000) irradiated with 24 MeV α -particles, at 773 K, (a) at over-focus and (b) at under-focus. (Ref. [68]) 21
- Figure 1.9 W sample irradiated with 15 keV He ions at 773 K up to 1.1×10^{17} ions/cm² to 3 *dpa*. TEM image of a He bubble lattice close to the [111] zone axis with inset showing the corresponding FFT; (b) shows the enlarged region of white dashed box in (a). (Ref.[77]) 21
- Figure 1.10 Diffusion pathways for a helium atom from one octahedral interstitial site to another octahedral interstitial site (a) directly in intrinsic thoria, (b), through an oxygen vacancy (c) and through a thorium vacancy in defective thoria. (d), (e) and (f) are the energy profiles corresponding to the diffusion mechanism (a), (b) and (c) respectively. (adapted from Ref.[91]) 24
- Figure 1.11 Irradiation damage (relative number of displacements – *dpa*) generated by β -decay and α -decay events in typical ceramics containing tank waste of DoE (USA). Courtesy Ref[17]. 28
- Figure 2.1 Schematic illustration of the solid state reaction method used to synthesize $Y_2Ti_2O_7$ and Y_2TiO_5 35

Figure 2.2	The photographs depicting the stages in the synthesis of thoria from the precursors thorium nitrate and citric acid, by citrate gel combustion method. (a) the gel before combustion, (b) combustion and (c) after combustion.	37
Figure 2.3	(a) Photograph of IPG glass melt, while pouring (b) Photograph of the IPG glass sample	38
Figure 2.4	Photograph of 1.7 MV Tandetron accelerator and the beamlines.	39
Figure 2.5	(Top) The schematic diagram and (Bottom) the photograph of the 150 kV accelerator facility.	41
Figure 2.6	Schematic of (a) Bragg-Brentano (θ - 2θ) geometry and (b) GIXRD geometry.	43
Figure 2.7	Schematic diagram showing the scattering geometry in GIXRD	44
Figure 2.8	Schematic illustration of the change in the size of Ewald sphere (in the reciprocal lattice), due to the variation in the wavelength of X-rays and electrons. (Ref.[139])	45
Figure 2.9	The LIBRA 200FE, high resolution transmission electron microscope: the photograph (Left) and the illustration of the electron path in the TEM (right).	47
Figure 2.10	Schematic diagram of polarized light soft X-ray absorption spectroscopy beamline BL01 at INDUS-2	50
Figure 2.11	(a) Schematic diagram of Omega energy filter in TEM for EELS analysis. (b) Typical EELS spectrum containing the zero loss peak, the plasmon peaks and the ionization edges (Ref.[142])	51
Figure 2.12	Block diagram representing the working of Raman spectrometer	52
Figure 3.1	Schematic illustration of the implantation of helium ions and the probe depth of GIXRD.	63
Figure 3.2	The GIXRD patterns of 100 keV He ⁺ ion irradiated thoria samples for the ion fluences of (a) 1×10^{17} ions/cm ² and (b) 5×10^{16} ions/cm ² along with (c) the as-prepared sample and (d) the thoria sample irradiated with 4 MeV Si ⁺ ion up to 2×10^{16} ions/cm ² . The plots (e), (f), (g) and (h) show the magnified view of the (111) peak in the patterns (a), (b), (c) and (d) respectively.	66
Figure 3.3	(a) The high resolution TEM image of the as-prepared thoria; the lattice fringes were indexed to (111) planes (d -spacing: 3.23 Å) and the zone axis was $\langle 110 \rangle$ (b) The electron diffraction pattern of thoria.	68
Figure 3.4	(a) The high resolution TEM image of He ⁺ ion irradiated thoria sample showing the presence of dark patches (b) Histogram of the size distribution of dark patches. (c) close view of one of the dark patches (d) the line profiles of intensities along the lines A, B and C across the dark patch.	69

- Figure 3.5 (a) The unit cell of thoria along with helium atoms in octahedral interstitial positions. (b) Illustration of the sublattice of oxygen and the sublattice of octahedral interstitial sites and Th-vacancy sites. (Thorium atoms are represented by white spheres, oxygen by black spheres and helium by red spheres with label) 72
- Figure 3.6 Total energies fitted to Birch-Murnaghan equation of state to obtain the lattice parameter for (a) perfect unit cell of thoria, (b) thoria with 8.33 *at%* of He (1He/unit cell) and (c) thoria with 33 *at%* of He (4He/unit cell). The lattice parameter increases with helium concentration. (Thorium atoms are represented by white spheres, oxygen by black spheres and helium by red spheres, with label) 73
- Figure 4.1 The unit cell of pyrochlore $Y_2Ti_2O_7$. Chemical environment of all the atomic species of $Y_2Ti_2O_7$ are illustrated individually. 82
- Figure 4.2 The unit cell of orthorhombic Y_2TiO_5 . Chemical environment of all the atomic species of Y_2TiO_5 are illustrated individually. 83
- Figure 4.3 GIXRD patterns of $Y_2Ti_2O_7$ (a) as-prepared and (c) irradiated with 70 keV Kr^+ ion, upto a fluence of 1×10^{17} ions/cm². The diffraction peaks of the unreacted precursors Y_2O_3 and TiO_2 are marked with \$ and *, respectively. Plots (b) and (d) show the expanded view of the prominent peak (222). There is a shift in the (222) peak from 30.5° to 31.1°. 85
- Figure 4.4 GIXRD patterns of Y_2TiO_5 (a) as-prepared and (c) irradiated with 70 keV Kr^+ ion, upto a fluence of 1×10^{17} ions/cm². The diffraction peaks of the unreacted precursors, Y_2O_3 and TiO_2 , are marked with \$ and * respectively. Plots (b) and (d) show the expanded view of the prominent peak (201). FWHM of the peak (201) has increased from 0.19° to 0.26°. 86
- Figure 4.5 (a) TEM image showing $Y_2Ti_2O_7$ particles (b) SAED pattern of $Y_2Ti_2O_7$ (zone axis: $\langle 002 \rangle$); (c) HRTEM image showing the lattice fringes of crystalline $Y_2Ti_2O_7$ (zone axis $\langle 011 \rangle$); (d) composition analysis with EDS. 88
- Figure 4.6 High resolution TEM images of $Y_2Ti_2O_7$ sample irradiated with 70 keV Kr^+ ions, showing the presence of stacking faults. 88
- Figure 4.7 (a) TEM image showing Y_2TiO_5 particles; (b) SAED pattern from a single crystal Y_2TiO_5 particle (c) HRTEM image showing the lattice fringes of crystalline Y_2TiO_5 (zone axis: $\langle 241 \rangle$); (d) composition analysis with EDS. 89
- Figure 4.8 (a) and (b) bright field TEM images of Y_2TiO_5 sample irradiated with 70 keV Kr^+ ions, showing the formation of faceted krypton bubbles. (c) Histogram showing the size distribution of the bubbles 90
- Figure 4.9 (a) and (b) show the Raman spectra of the as-prepared samples of $Y_2Ti_2O_7$ and Y_2TiO_5 respectively. (c) and (d) show the Raman spectra of $Y_2Ti_2O_7$ and Y_2TiO_5 , after irradiation with 70 keV Kr^+ ions. 91

- Figure 4.10 Oxygen K edges of (a) $\text{Y}_2\text{Ti}_2\text{O}_7$ and (b) Y_2TiO_5 , from EELS and DFT calculations. 97
- Figure 4.11 Ti L_{23} edges of (a) $\text{Y}_2\text{Ti}_2\text{O}_7$ and (b) Y_2TiO_5 , from EEL spectra, DFT calculations and from CTM4XAS. 99
- Figure 4.12 2D plot of differential charge density, showing the degree of covalency of the (Ti-O) and (Y-O) bonds in (a) $\text{Y}_2\text{Ti}_2\text{O}_7$ and (b) Y_2TiO_5 . The differential density is plotted along the (101) plane in $\text{Y}_2\text{Ti}_2\text{O}_7$ and along (010) plane in Y_2TiO_5 . The charge density fields are normalized to the number of electrons per \AA^3 . 102
- Figure 5.1 XRD patterns of the as-prepared and 4 MeV O^+ ion irradiated IPG samples. The hump corresponding to the amorphous IPG is seen in both cases. 110
- Figure 5.2 TEM micrographs of the as-prepared IPG sample; (a) The SAED pattern (b) The intensity profile averaged across radial lines in the SAED pattern (c) High resolution TEM image and (d) low magnification TEM image. The sample is perfectly amorphous. 111
- Figure 5.3 TEM micrographs of the IPG sample irradiated with 4 MeV O^+ ions up to the fluence of 5×10^{13} ions/cm²: (a) The SAED pattern containing spotty rings (b) The intensity profile averaged across radial lines of the SAED pattern (c) High resolution TEM image showing lattice fringes and (d) TEM dark field image, where the region with bright contrast corresponds to crystalline phases. Crystalline phases of $\text{Fe}_4(\text{P}_2\text{O}_7)_3$, $\text{Fe}(\text{PO}_3)_3$ and P_2O_5 are identified from the SAED pattern. 112
- Figure 5.4 TEM micrographs of the IPG sample irradiated with 4 MeV O^+ ions up to the fluence of 5×10^{16} ions/cm²: (a) The SAED pattern containing spotty rings (b) The intensity profile averaged across radial lines in the SAED pattern (c) High resolution TEM image showing lattice fringes and (d) low magnification TEM image. Crystalline phases of $\text{Fe}_4(\text{P}_2\text{O}_7)_3$ and P_2O_5 are identified from the SAED pattern. 114
- Figure 5.5 TEM micrographs of the IPG sample heat treated at 900 °C for 48h: (a) SAED pattern with spotty rings, (b) The intensity profile averaged across radial lines in the SAED pattern (c) High resolution TEM image showing lattice fringes and (d) low magnification TEM image. Crystalline phases of $\text{Fe}_4(\text{P}_2\text{O}_7)_3$ and $\text{Fe}(\text{PO}_3)_3$ are identified. 115
- Figure 5.6 O K-edge in the (a) XAS and (b) EEL spectra from the as-prepared and 4 MeV O^+ ions irradiated IPG samples. The relative intensity of A1 peak to A2 (in XAS) decreases with ion fluence. 117
- Figure 5.7 Fe L_{23} -edge in the (a) XAS and (b) EEL spectra from the as-prepared and 4 MeV O^+ ions irradiated IPG samples. 118

List of tables

Table 1.1	Approximate time-scale for the production of defects due to irradiation[28].	10
Table 3.1	Details of ion irradiations: 100 keV He ⁺ and 4 MeV Si ⁺ ions on thoria.	63
Table 3.2	Helium formation energies at different locations in defective thoria system. (Thorium atoms are represented by white spheres, oxygen by black spheres and helium by red spheres. Vacancy is represented by a cube. The arrow mark notifies the position considered for the formation of helium atom.)	70
Table 3.3	The binding energies for different configurations of helium in thoria lattice.	72
Table 4.1	The crystal structure details of Y ₂ Ti ₂ O ₇ (<i>fcc</i> system with the space group 227 (Fd3m), setting 2). The value of the lattice parameter <i>a</i> is 10.09Å (expt.) 10.15Å (calc.).	82
Table 4.2	The crystal structure details of Y ₂ TiO ₅ (orthorhombic with space group Pnma (62)). The experimentally observed lattice parameters (<i>a</i> , <i>b</i> , <i>c</i>) are (10.33, 3.699, 11.18)Å and the calculated values are (10.40, 3.701, 11.31)Å.	83
Table 4.3	The profile of the peaks in the Raman spectra of Y ₂ Ti ₂ O ₇ before and after the irradiation with 70 keV Kr ⁺ ions (1×10 ¹⁷ ions/cm ²).	92
Table 4.4	The peak position and FWHM of the Raman spectra of Y ₂ TiO ₅ before and after the irradiation (70 keV Kr ⁺ ions, ion fluence: 1×10 ¹⁷ ions/cm ²).	93
Table 5.1	Details of the irradiation experiments on IPG and the damages for different ion fluences.	109
Table 5.2	Comparison of the d-spacing of the heat treated and the ion irradiated IPG samples with ICDD database.	113
Table 5.3	The pre edge features of the O K-edge in XAS of the as-prepared and 4 MeV O ⁺ ion irradiated IPG samples.	117

Chapter 1

Radiation damage in nuclear oxide materials - A brief review

1.1. Motivation

Oxide materials have remarkable physico-chemical properties such as high strength, low thermal expansion, high thermal conductivity, chemical stability and especially stability against radiation. Hence oxide materials find application in a wide range of fields. Particularly, oxides find applications in the nuclear industry, where the materials are expected to provide extended service under extreme conditions like high radiation, high temperature and high pressure[1–3]. In fact, many of the technologically important categories of materials used in the nuclear industry are ceramic oxides.

Fuel materials are the most important category of materials used in the nuclear industry. The oxide ceramic materials used in the nuclear industry are exposed to intense radiation. In the case of nuclear fuel materials, the energetic fission fragments and the α -particles from α -decay are the main cause of radiation damage, and in any fuel material, inert gas induced swelling is one of the major concern. In addition to the fission gases Xe and Kr, considerable quantity of helium also is produced in the fuel as a result of triple fission, α -decay and interactions between nuclei and fission neutrons[4]. Accumulation of all these inert gases leads to fuel swelling, and results in degradation of thermal conductivity of fuels[5–7]. This ultimately affects fuel performance. If the thermal conductivity is low, the temperature gradient in the radial direction of the fuel pellet increases which results in high temperature at the central part of the fuel pin[8], and it is not desirable. The thermal conductivity of nuclear fuel influences almost all important processes such as fission gas release, swelling, grain growth etc. and limits the linear power[9].

The radiation response of oxide based ceramics are very different from metals[3,10] and the fundamental difference is in the nature of bonds and crystal structure. Metals and alloys exist in simple crystal structures like cubic or hexagonal, whereas ceramics have complex crystal structures such as fluorite or pyrochlore. Moreover, the complex crystal structures consist of many sublattices populated by atoms with different masses and valency. The different atoms in the given material have different displacement threshold energies (E_d) and also the nuclear and electronic stopping ratio differs significantly between the sublattices[11]. Basically, ceramics show difference in their response to radiation induced defect production, defect aggregation and defect recovery. The predominant fuel materials like urania, mixed oxide fuel (PuO_2/UO_2), and the potential alternate fuel thoria, are all oxide based ceramic materials[2,12]. Among them, thoria has drawn attention as a potential source of nuclear energy since the 1950s due to several attractive features of the Th–U²³³ fuel cycle and because of its abundance on earth.

Oxide nanoparticles are used as dispersoid in steel to strengthen the mechanical strength against radiation and creep. Fine particles of Y–Ti–O oxide particles (yttrium titanates) are dispersed in ferritic steel matrix. The strength of these ODS steels, therefore, depends on the stability of these particles under radiation, which eventually depends on the strength and the nature of the metal–oxygen (M–O) bonds in these oxide particles. These stable nanodispersoids are identified as the oxides of $\text{Y}_2\text{Ti}_2\text{O}_7$ and Y_2TiO_5 [13], collectively called yttrium titanates.

Mostly oxide based glass materials are used as wasteforms for the immobilization and disposal of nuclear wastes. Presently, borosilicate glass (BSG) is being used for the disposal of nuclear wastes from thermal reactor[14]. Iron phosphate glass (IPG) is being proposed[15,16] as the appropriate glass matrix for the disposal of fast reactor wastes, which has higher concentration of fission products, minor actinides, noble metals and volatile fission products. In addition,

few more ceramic oxide materials like synroc, titania (glass-ceramic composites) are also proposed as alternative wasteforms[17]. The major concern in glassy wasteforms is the radiation induced relaxation processes like crystallization. Because, the amorphous phase of the glass provides the open space needed to contain the radioactive actinides and reduces its leach rate. Therefore, studies on the radiation induced relaxation processes in the wasteforms helps to improve the material.

It is desired that the materials used in nuclear industry should have high strength, low thermal expansion, good chemical stability and above all better radiation resistance[2,11,18]. The search for radiation-tolerant fuel materials, structural materials and wasteforms has been areas of intense research in recent years[17,19–21].

The radiation response of oxide based ceramics are very different from metals[3,10]. The fundamental difference is in the nature of bonds and crystal structure. Metals and alloys exist in simple crystal structures like cubic or hexagonal, whereas ceramics have complex crystal structures such as fluorite or pyrochlore. Moreover, the complex crystal structures consist of many sublattices populated by atoms with different masses and valency. So, ceramics show significant difference in their response to radiation, in terms of defect production, defect aggregation and defect recovery.

The present thesis deals with the studies on the radiation stability of oxide ceramics: (i) thorium dioxide or thoria (ThO_2), a nuclear fuel material, (ii) yttrium titanates ($\text{Y}_2\text{Ti}_2\text{O}_7$ and Y_2TiO_5), the oxide-dispersoids used for strengthening the structural material, (iii) Iron Phosphate Glass (IPG), the material proposed for the disposal of high level nuclear waste from fast reactors.

In order to study the radiation resistance of the materials, in the present thesis, radiation damage is simulated experimentally on the samples, using ion beams from particle accelerators.

This chapter, gives a summary of ion solid interactions, the energy loss processes and the process of defect generation by ion beams. An introduction to the radiation damage effects in nuclear materials is also given, with emphasis on oxide based ceramics. This chapter further discusses the radiation resistance characteristics of oxide ceramic materials in comparison with that of metals and alloys. Further this chapter discusses the significance of the materials investigated in this thesis; explains the technical details of their applications in nuclear industry and identifies the unresolved crucial questions, thereby motivating the thesis work.

1.2. Ion-solid interactions

Ion beam irradiation is the powerful experimental technique to simulate radiation damages that take place over years, within laboratory time scales. A brief introduction on the basic ion-solid interactions, that produces various radiation effects in materials, is given below.

1.2.1. Energy loss mechanisms – Stopping of ions in solids

Ion irradiation means bombarding energetic ions on a solid material using particle accelerators. Energetic ions interact with solid and lose energy primarily by two mechanisms: interactions that lead to electronic excitation (electronic energy loss) and interactions with target nuclei (nuclear energy loss). Nuclear stopping results in displacement of lattice atoms and electronic stopping leads to ionization. Accordingly, the stopping power (the energy loss per unit length) is termed as nuclear stopping power (denoted by S_n) and electronic stopping power (denoted by S_e). The total energy loss S is a combined effect of both the energy loss processes, *i.e.*, $S = S_e + S_n$, or,

$$\left(\frac{dE}{dx}\right) = \left(\frac{dE}{dx}\right)_e + \left(\frac{dE}{dx}\right)_n$$

Eqn. 1.1

Generally, electronic energy loss dominates when the incident ion has high energies (of the order of 1 MeV/nucleon), whereas nuclear stopping becomes

prominent as the ion slows down (to ~ 1 keV/nucleon). So, in swift heavy ion irradiation, electronic energy loss dominates whereas in the case of low energy ion irradiation, nuclear energy loss dominates. Figure 1.1 shows a schematic of the contributions from both the electronic and nuclear stopping powers as a function of energy of incident ion. Here, the values E_1 (the maxima of S_n), E_3 (the maxima of S_e) and E_2 (the cross-over point), all depend on the target material and the mass and the energy of the projectile.

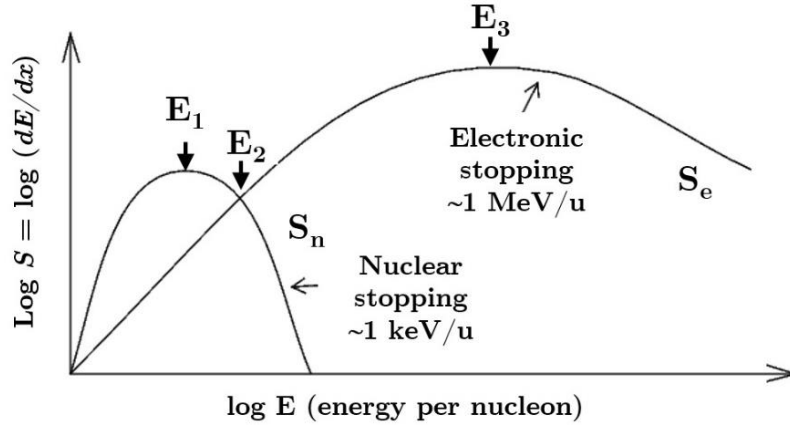


Figure 1.1 Schematic illustration of the typical partitioning of energy in between the two energy loss processes (S_n and S_e), as a function of the energy of the incident ion.

1.2.1.1. Electronic stopping

The electronic stopping includes processes like (1) momentum exchange due to collisions between the incident ion and a free electron in the target, (2) ionization of the incident ion, (3) electron capture by the incident ion, (4) de-excitation of the incident ion, (5) de-excitation of the target atom and (6) ionization of the target atom. The significance of these processes depend on the velocity of the incident ions. The velocity of the ions can be demarcated into three regimes: (a) the low velocity regime, where the ion velocities are below the Bohr velocity v_0 of the target electrons (b) the high velocity regime with $v > \sqrt[3]{Z_1^2} v_0$, where $\sqrt[3]{Z_1^2} v_0$ is the mean velocity of electrons filling a neutral atom, as given by Thomas-Fermi statistical theory[22], and (c) the intermediate regime, which comprises of the velocities of ions in the range $v_0 < v < \sqrt[3]{Z_1^2} v_0$.

In the high energy regime where the ion is stripped of its electrons the electronic stopping cross section S_e is given by[23]:

$$S_e = \frac{2\pi Z_1^2 Z_2 e^4 M_1}{m_e E} \ln \left(\frac{4m_e E}{M_1 I} \right) \quad \text{Eqn. 1.2}$$

where Z_1 and Z_2 are atomic number of projectile and the target atoms, respectively. M_1 is the mass number of projectile ion with energy E , e and m_e are the charge and the mass of electron, I is the ionization energy of target material.

Lindhard and Scharff[24] developed a theory to predict the electronic stopping S_e in the intermediate energy regime.

$$S_e = \xi_e 8\pi e^2 a_0 Z_1 Z_2 \left(Z_1^{2/3} + Z_2^{2/3} \right)^{-3/2} v/v_0 \quad \text{Eqn. 1.3}$$

where ξ_e is a constant of the order $Z_1^{1.6}$ and a_0 ($= 0.053$ nm) is the Bohr radius. Hence, in the intermediate energy regime, the electronic energy loss is proportional to the velocity of the ion.

1.2.1.2. Nuclear stopping

The nuclear stopping is the sum of energy losses of an ion to elastic collisions with the target nuclei. When the ions interact with target nuclei, there is a direct transfer of kinetic energy to the target atoms by elastic collisions between the projectile nucleus and the target nuclei. A common feature for all ions is that the nuclear stopping has a maximum at low energies (~ 1 keV/nucleon) and it decreases as the energy of the ions increases. Depending on the value of the reduced range relative to the Thomas-Fermi screening radius a_{TF} , nuclear stopping is classified into two regimes.

a) High energy elastic collisions regime $\rho \ll a_{TF}$

At high energies, where the interaction between the projectile and the target nuclei can be accurately represented by a coulombic interaction, the nuclear stopping cross section is given as[22]:

$$S_n = \frac{4\pi Z_1^2 Z_2^2 E_R^2 a_0^2}{E} \ln \left(\frac{a_{\text{TF}}^2 E^2}{4Z_1^2 Z_2^2 E_R^2 a_0^2} \right)$$

Eqn. 1.4

where E_R is the Rydberg energy and

$$a_{\text{TF}} = \frac{0.885 a_0}{(\sqrt{Z_1} + \sqrt{Z_2})^{\frac{2}{3}}}$$

Eqn. 1.5

b) Low energy elastic collision regime $\rho > a_{\text{TF}}$

In this case, the nuclear stopping S_n is given by[22],

$$S_n = \frac{8.462 \times 10^{-15} Z_1 Z_2 M_1 s_n(\epsilon)}{M_1 + M_2 (Z_1^{0.23} + Z_2^{0.23})}$$

Eqn. 1.6

where the universal ZBL (Ziegler, Biersack and Littmark[26]) stopping (in reduced notation) is given by,

$$s_n \epsilon = \frac{0.5 \ln(1 + 1.1383\epsilon)}{(\epsilon + 0.01321\epsilon^{0.21226} + 0.19593\epsilon^{0.5})}$$

Eqn. 1.7

The reduced energy ϵ in Equation 1.15 and 1.16 is given as[25],

$$\epsilon = \frac{EM_2/(M_1 + M_2)}{Z_1 Z_2 e^2 / a_{\text{TF}}}$$

Eqn. 1.8

1.2.2. Ion Range and Straggling in solid

In reality, the actual path that an ion follows during implantation would be convoluted. However, the average of the total integrated distance traveled by ions is well defined and is called the range (R). The range is given by,

$$R = \int_E^0 \frac{dE'}{S(E')}$$

Eqn. 1.9

This is the net projected distance an ion travels perpendicular to the substrate surface before coming to rest. Due to the statistical nature of the energy loss processes, different ions stop at different depths, giving rise to a distribution around the mean value of the range, called projected range (R_p) (illustrated in Figure 1.2(a)). The distribution is often approximated to a Gaussian and the half

width of the distribution defines the straggling in the projected range (ΔR_p). The depth profile of the implanted atoms have a Gaussian distribution, as described in Figure 1.2(b). But in single crystals it becomes more complicated because of ion channeling effects. The stopping power, range and straggling of ions are usually calculated using the well-known computer code ‘Stopping and Range of Ions in Matter’ or SRIM[26].

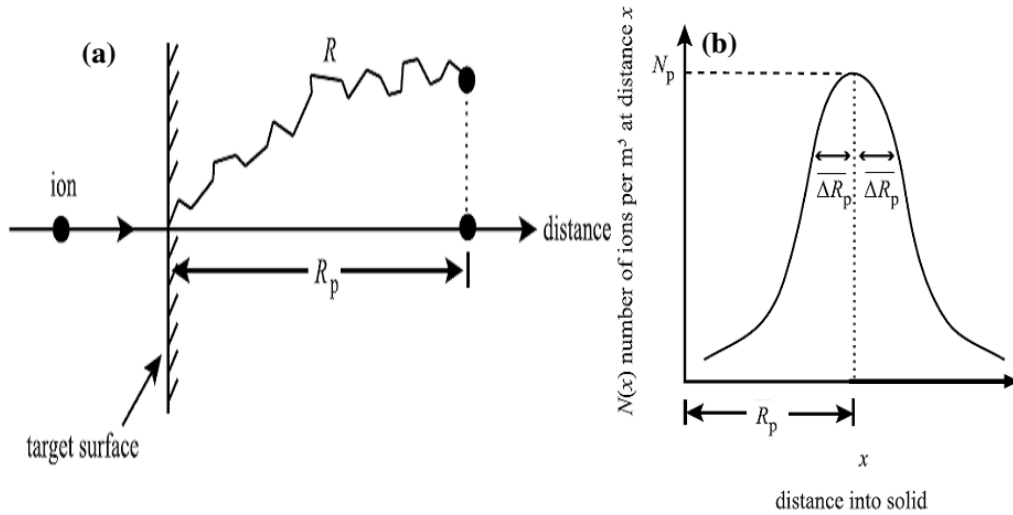


Figure 1.2 The schematic representation of (a) the projected range (R_p) and (b) the distribution of implanted atoms, as a function of depth (with, ΔR_p , the straggling).

1.2.3. Sputtering

It may happen that a target atom in the surface of the material receives momentum which is directed towards the surface. If the kinetic energy of such an atom is high enough to overcome the surface binding energy, it will leave the surface and will be sputtered away. Under continuous irradiation, the surface will be eroded as a whole. This phenomenon is called as sputtering. The theoretical description of sputtering phenomenon is formulated by Sigmund[27]. Here the sputtering yield Y , is defined as the average number of sputtered atoms per incident ion. For linear collision cascades, *i.e.*, for an isotropic distribution of sufficiently small number of binary collisions within a cascade, the sputtering yield Y is given by,

$$Y(E, \theta) \propto \frac{\alpha S_n(E)}{E_{sb}}$$

Eqn. 1.10

where α being a dimensionless function of the angle of incidence θ and the mass ratio M_2/M_1 , E is ion energy, E_{sb} is the surface binding energy and $S_n(E)$ is the nuclear stopping. According to *Eqn. 1.10*, the sputtering yield depends on the surface binding energy and also on the atomic species. In multi component materials like complex oxides, different sputtering yields might therefore be observed for individual atomic species, *i.e.*, one or more atomic species are sputtered preferentially. Due to this preferential sputtering, the surface concentrations are altered with increase in ion dose even in a homogeneous material. SRIM[26] software also provides an estimate of the sputtering yield for the different atomic species present in complex systems like oxides.

1.2.4. Radiation damage

The energy loss by nuclear stopping primarily produces defects and radiation damage in solids. The primitive damages in solid materials due to ion irradiation involve the microscopic defects produced in materials such as creation of primary knock on atom, displacement cascade, stable Frenkel pairs and defect clusters, etc. These microscopic defects are referred to as *radiation damage*. These microscopic defects modify the macroscopic properties, which are referred to as *radiation damage effects* or simply *radiation effects*. The characteristic time scales for ‘radiation damage’ and ‘radiation effects’ is vastly different. Radiation damage events take place in time scale less than 10^{-11} sec after the ion has interacted with the solid. Radiation effects manifests later on and evolves over months and years.

The microscopic displacement damage event is actually composed of several distinct processes such as (i) the interaction of an energetic incident particle with a lattice atom and the transfer of kinetic energy to the lattice atom resulting in the displacement of the atom from its lattice site; this atom is called as the primary

knock-on atom (PKA), (ii) the passage of the displaced atom through the lattice accompanied by the creation of additional knock-on atoms; the secondary knock on atoms, (iii) the production of a displacement cascade (collection of point defects created by the PKA) (iv) the termination of the PKA as an interstitial atom in the lattice. This entire chain of events consumes only about 10^{-11} s (see Table 1.1).

Table 1.1 Approximate time-scale for the production of defects due to irradiation[28].

Time	Event	Result
10^{-18} s	Energy transfer from the incident particle	Creation of a PKA
10^{-13} s	Displacement of lattice atoms by the PKA	Displacement cascade
10^{-11} s	Energy dissipation, spontaneous recombination and clustering	Stable Frenkel pairs and defect clusters
$>10^{-8}$ s	Defect reactions by thermal migration	SIA and vacancy recombination, clustering, trapping, defect emission
Years	Macroscopic radiation effects	Embrittlement, void swelling, etc.

The collision cascade phenomena is classified into three different regimes based on the energy of the ions and the damage mechanism, as illustrated in Figure 1.3. In the single collision regime (Figure 1.3(a)), which is typical for light ions at low energy, the atomic motion is stopped after a few collisions and so a cascade does not develop. The linear cascade regime (Figure 1.3(b)) is the regime where collisions take place only between fast moving ions and atoms at rest. This regime is the standard regime in the range of ion energies of the order of keV. In contrast, in the thermal spike regime (Figure 1.3(c)), the cascade becomes so dense that collisions between fast particles play an essential role. The life time of the spike is of the order of 10^{-13} s, which is of the order of the period of lattice vibrations.

The simplest theory of displacement cascade is given by Kinchin and Pease model[29], which gives an estimate of the maximum number of Frenkel pairs created by the incoming particle. The model assumes the following: (i) The cascade is

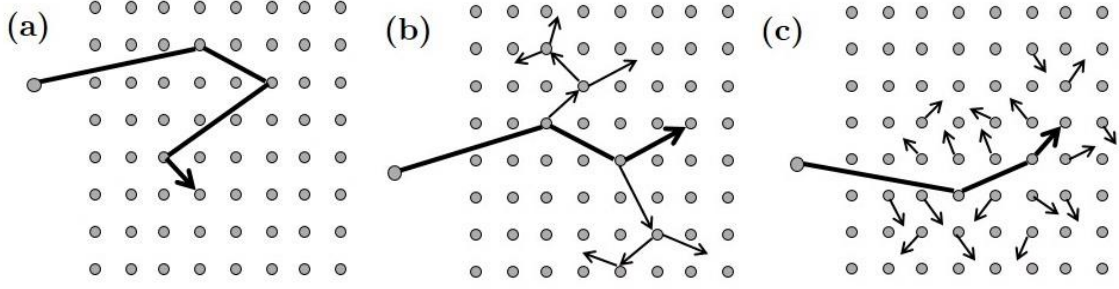


Figure 1.3 Schematics of cascade regimes (a) single collision regime, (b) linear cascade and (c) thermal spike.

created by a sequence of two-body elastic collisions between atoms and the energy-transfer cross section is given by the hard-sphere model. (ii) The PKA or any lattice atom struck by a PKA or higher order recoil must receive a minimum amount of energy in the collision (called the displacement threshold energy E_d) in order to be displaced from its lattice site. It is assumed that E_d is consumed in displacing an atom and gets subtracted from the initial energy. (iii) The arrangement of the atoms in the solid is random *i.e.*, the effects due to crystal structure is neglected. (iv) No atomic displacements occur, when the PKA energy is greater than E_c , the cutoff energy ($E_c \cong A$ keV, where A is the mass number of the incident ion.) For all energies less than E_c , electronic stopping is ignored, and only atomic collisions take place. The number of atoms displaced by a single PKA with energy E , is given by

$$\nu E = \begin{cases} 0 & 0 < E < E_d \\ 1 & E_d < E < 2E_d \\ \frac{E}{2E_d} & 2E_d < E < E_c \end{cases}$$

Eqn. 1.11

Displacements per atom (dpa) is the unit, which is used to compare radiation damage by different radiation sources. It is the number of times an atom is displaced from its normal lattice site by atomic collision processes. It may also be noted that the probability of athermal annihilation of vacancies and interstitials is also large because of the proximity of the point defects in a cascade. Hence, the number of point defects that survive a cascade can be as low as 1% of the number predicted by any simple cascade theory.

Thus, high energy particles induce the formation of point defects and defect clusters within picoseconds. With time, normal diffusion processes take place and irradiation induced defects recombine or cluster together to form more stable damage structures. So, a large population of different types of stable defect structures such as interstitials, vacancies, defect clusters, dislocation loops, dislocation network, stacking faults, voids, helium bubbles, precipitates, etc. are formed during irradiation. They may lead to order–disorder transformations, amorphization and swelling of the material, and also to phase decomposition or formation of new crystalline phases[17].

1.3. Ion irradiation effects in materials

Ion irradiation leads to changes in several properties of the material. The changes in properties are due to the formation of interstitial and or vacancy defects, defect clustering, order-disorder transformations, amorphization, swelling, phase decomposition or the formation of new crystalline phases. The structure and composition of the material provide a critical means of controlling its radiation response.

This leads to alterations in physical properties (like transport, optical, corrosion, oxidation), as well as mechanical properties (like strength, hardness, wear resistance, fatigue resistance). The compositional changes brought about by ion bombardment are classified into recoil implantation, cascade mixing, radiation-enhanced diffusion, radiation-induced segregation, Gibbsian adsorption and sputtering. Microstructurally, the phases present are often altered from what is expected from equilibrium thermodynamics, giving rise to order-disorder transformations, metastable (crystalline, amorphous or quasicrystalline) phase formation and growth, densification, grain growth, formation of a preferred texture and the formation of a high density dislocation network.

1.3.1. Effects of low energy ion irradiation – nuclear processes

In low energy ion irradiation, where the projectiles have energy ~ 1 keV per nucleon, the projectiles are implanted at shallow depths (few hundreds of nanometer) and the predominant mode of energy loss would be through nuclear processes. A classic example for the effects of low energy ion irradiation was reported by Amirthapandian *et al.*[30,31], where low energy ion irradiation has induced the mixing of (few nm thick) multilayers of Fe/Ag. Fe and Ag metals, which are thermally immiscible, readily mixed completely when irradiated with 85 keV Ar^+ ions at 110 K. The mixing at 325 K was not homogeneous even at a high ion fluence of 3×10^{16} ions/cm², as evident from the presence of a sharp sextet in the Mossbauer spectrum, with the hyperfine field of 33 T (shown in Figure 1.4(a)), along with a doublet and a broad sextet. The sharp sextet corresponds to the Fe atoms in the interior of α -Fe. But at 110 K, the Fe atoms were intermixed with Ag atoms at a low ion fluence of 1×10^{15} ions/cm², as evidenced by the presence of only a single doublet (shown in Figure 1.4(b)). This suggested that Fe atoms were completely intermixed with Ag atoms.

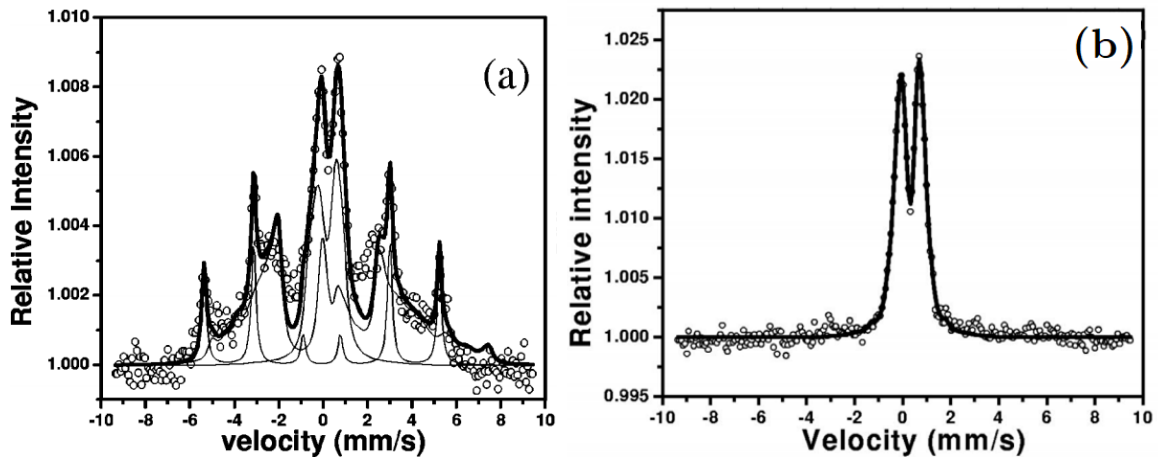


Figure 1.4 Mossbauer spectra from the multilayers of Fe/Ag 85 keV Ar^+ ions (a) at 325 K, ion fluence 3×10^{16} ions/cm² (b) at 110 K, ion fluence of 1×10^{15} ions/cm².

Another interesting phenomenon induced by low energy ions, was seen in diamond, where the ion beam induces an unusual phase transformation. Diamond

undergoes a transition from insulating material to a conducting material upon irradiation with 320 keV Xe⁺ or with 100 keV C⁺ ions[32].

1.3.2. Irradiation effects due to electronic energy loss

Irradiation of materials, by high energy, heavy ions (referred to as swift heavy ions or SHI), results in highly excited lattice atoms with negligible contributions from elastic collisions. It is expected that the lattice atoms are not displaced in the case of electronic excitation generated by SHI. But, the electronic energy deposition beyond a certain threshold[33] (~ 10 keV/nm) can cause the movements of atoms even in metals, which can lead to mixing. Ion beam mixing was observed in Ti/Si systems by 200 MeV Ag ions, where the loss is > 10 keV/nm. The displacement of lattice atoms occurs in insulating materials in a cylindrical core along the ion path, called ‘ion tracks’, which is the most prominent effect of SHI. When ion tracks form, the electronic energy loss (above the threshold), induces a crystal-to-amorphous phase transition along the ion path. Figure 1.5 shows the high resolution TEM image of an ion track reported by Park *et al.*[34] in Gd₂Ti₂O₇ pyrochlore. The shell (Region 1 in Figure 1.5) around the core (Region 2 in Figure 1.5) exhibits defect fluorite structure.

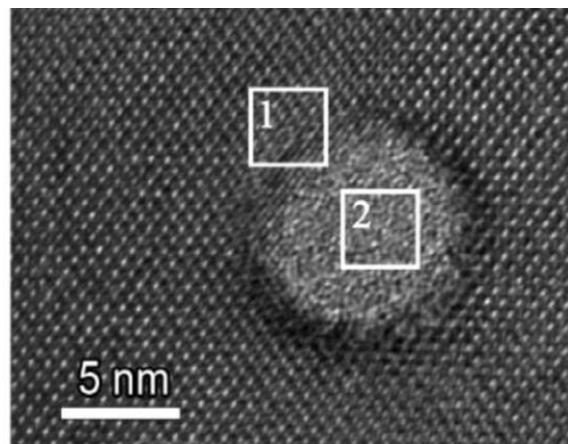


Figure 1.5 TEM images of single ion track in Gd₂Ti₂O₇. There is a defect-fluorite shell (Region 1; 1.5 nm thick) that surrounds the amorphous core track (Region 2). (Ref.[34])

Several interpretations have been proposed to explain the formation of ion tracks by SHI. The prominent models are the ‘Coulomb explosion’ model and the ‘thermal spike’ mechanism.

According to the ‘coulomb explosion’ model (originally proposed by Fleischer *et al.*[35]) when a swift heavy ion traverses a solid target, its kinetic energy is transferred to the target electrons within a short timescale of 10^{-17} sec and these electrons move away from the ion path leaving a positively charged inner cylinder. The created ions will repel each other by electrostatic forces and this repulsion leads to effective atomic motion and thence track formation. This happens only if the electrostatic energy surpasses the chemical bond energy.

Two models are currently proposed to explain track formation in solids due to ion irradiation. The first one[36,37] considers the irradiated solid as a two component medium: the electron gas and the atomic lattice. After the passage of the irradiating ion (within 10^{-17} sec), the energy received by the ejected electrons is first shared with the other electrons in the vicinity of the ion trajectory due to electron–electron interaction. This process gives rise to a local thermalization of the electron gas within a period 10^{-15} sec. The subsequent electron–lattice interactions transfer heat to the lattice atoms giving rise to a large increase of temperature in short time scales (10^{-11} s) , the so-called ‘thermal spike’. The other version of the thermal spike is based on an analytical approach[38]. The main assumption of this model is that soon after the passage of the irradiating ion, a fraction of the electronic energy loss S_e is converted to heat for the atomic lattice and that the lattice temperature has a Gaussian distribution with an initial radial extension a_0 which evolves with time.

When these ion tracks start to overlap, its effects (such as modification of defect concentration, atomic transport, phase transformation and track formation) spread over the sample and eventually saturates after spanning the whole surface

of the sample. This phenomenon is rightly explained as the single ion impact mechanism.

The high electronic energy loss released by swift heavy ions in solid materials would also be manifested as modifications in defect concentrations, atomic transport, and phase transformation. In the case of amorphous materials, SHI irradiation leads to macroscopically visible anisotropic mass transport, called Klaumunzer's effect[39,40], which results in a giant anisotropic deformation. None of the available growth mechanisms proposed for crystalline metals is able to explain this kind of radiation growth.

1.3.3. Void swelling

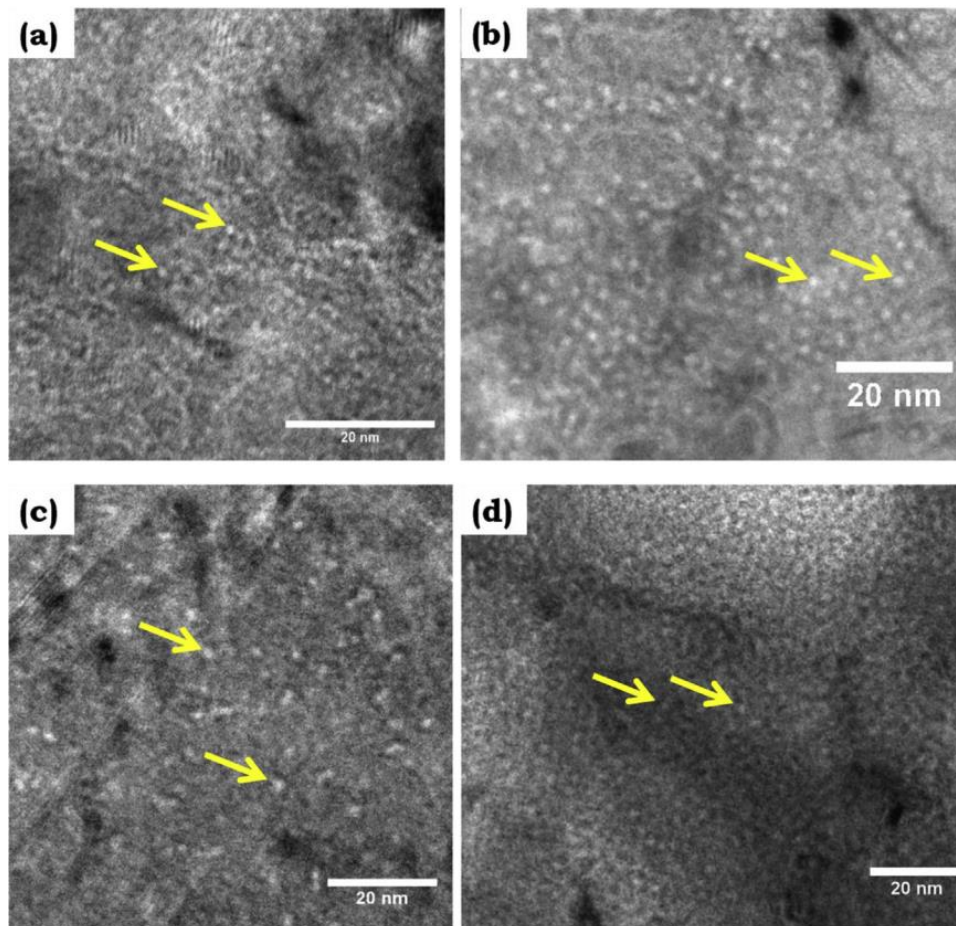


Figure 1.6 Cavities in D9 steel alloys pre-implanted with 100 appm of helium and subsequently implanted with 2.5 MeV Ni^{2+} ions, at (a) 500 °C (b) 550 °C (c) 600 °C (d) 650 °C. The arrows point towards typical cavities. (Ref.[41])

One major radiation effect of displacement damage produced by fast neutrons in the core structural materials in a fast reactor is void swelling. Ion irradiation is extensively used for the simulation of neutron damage in structural materials. Balaji *et al.*[41] have studied the void swelling phenomenon in D9 steel using ion irradiation experiments. The authors have implanted helium in the D9 steel sample, followed by the implantation of nickel (2.5 MeV Ni²⁺) ion, so as to produce a peak damage of 100 *dpa*, at various temperatures and studied the temperature dependence of void swelling. The TEM micrographs (Figure 1.6) show the presence of nano cavities (voids) upon ion irradiation. The void swelling was calculated from the average size of these cavities. The authors have noticed peak swelling at 550 °C.

1.3.4. Ion irradiation induced phase transformations

The thermodynamic and kinetic aspects of ion irradiation-induced phase transformations in intermetallic compounds are detailed by Nastasi *et al.*[42]. This review has shown that irradiation-induced transformations can be quantitatively understood from free energy considerations. The energy of a system under irradiation was elevated by the gradual accumulation of lattice damage, and directly by the formation of a thermal spike in the collision cascade. The irradiated sample, therefore, assumes a state of higher free energy and is the driving force for a transformation to a lower free energy state, different from the initial phase. For example, ion-beam-induced amorphization in Si is of significant interest, for the fabrication of Si devices[43].

Although amorphization is the predominant effect of ion irradiation, ion beams are known to produce even the reverse phenomenon, namely amorphous-to-crystalline transition. In some cases, even crystalline-to-crystalline transitions are also observed.

Ion beam induced amorphization of complex ceramic materials have been reviewed by many authors[11,18,44]. Electronic excitation and ionization arising from the electronic energy loss (S_e) of energetic ions induces structural changes in

material systems with a low electrical conductivity and also in metallic alloys[36]. Ion beam induced amorphization may be categorized into heterogeneous amorphization and homogeneous amorphization. Heterogeneous amorphization occurs when the isolated damage regions, created by individual ions, start to overlap. Homogeneous amorphization takes place via the buildup of simple defects.

Amorphous-to-crystalline transitions are observed mostly in metallic glasses. Many mechanisms have been proposed[45–47] to rationalize this phenomenon, including the one that associates the local adiabatic heating inside the shear bands as causing the crystallization. There are two basic modes of deformation in metallic glasses homogeneous flow and inhomogeneous flow. It was experimentally found that metallic glasses deform homogeneously at high temperature and/or low strain rate whereas they deform inhomogeneously at low temperature and/or high strain rate. In this latter case, the deformation is localized in thin bands, called shear or deformation bands. In homogeneous flow, each volume element of the specimen contributes to the strain, and in inhomogeneous flow, the strain is localized in a few very thin ‘shear bands’. Shear bands contain homogeneously distributed excess free volume. The material inside the shear bands undergoes some structural change which leads to a local lowering of the viscosity[48], associated with an increase in the free volume. This enhances diffusion locally. When diffusion is enhanced, the metastable glass takes the stable crystalline structure. An exhaustive review of shear bands in metallic glasses may be seen in[49,50].

He *et al.*[48] investigated the local microstructure evolution at shear bands in phase-separated bulk metallic glasses, by experiments. They demonstrated that there exists an affected zone around the shear band and that that changes originate not only from the shear bands themselves, but also from the affected zones in the adjacent matrix. This work shed light on direct visualization of deformation-related effects, in particular increased atomic mobility, in the region around shear bands. Chen *et al.*[51] has observed crystallization within the shear bands of aluminium-

based amorphous alloys induced by bending, and the crystallization was a consequence of local atomic rearrangements in regions of high plastic strain.

Rizza *et al.*[52] expected that shear bands should form close to the ion track in swift heavy ion (SHI) irradiation. SHI irradiation induces a localized shear stress, along with a large strain rate, and it generates an outgoing pressure wave[53,54]. Therefore, in the same way as shear bands were formed during high strain rate experiments, deformation bands are expected to be formed close to the ion track in SHI. Rizza *et al.*[52] have experimentally observed the formation of shear bands, induced by swift heavy ions, in $\text{Fe}_{73.5}\text{Nb}_{4.5}\text{Cr}_5\text{Cu}_1\text{B}_{16}$ sample, when irradiated to a fluence of 1×10^{10} ions/cm² with 30 MeV C₆₀. (See Figure 1.7.)

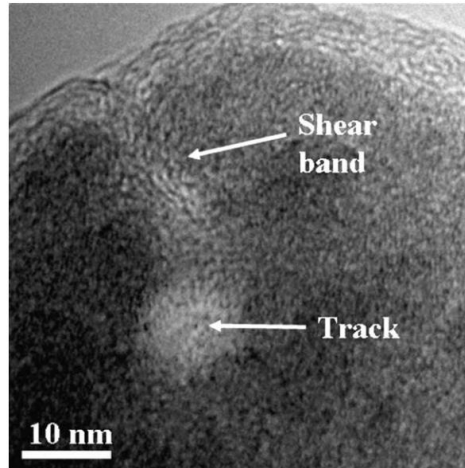


Figure 1.7 TEM image of an isolated track in an $\text{Fe}_{73.5}\text{Nb}_{4.5}\text{Cr}_5\text{Cu}_1\text{B}_{16}$ sample irradiated to a fluence of 1×10^{10} cm⁻² with 30 MeV C₆₀. A deformation band which exits toward the sample edge is visible.

The most interesting type of transition, induced by ion irradiation, is the transformation from one crystalline phase to another crystalline phase. The first such report was by Dammak *et al.*[55], where *hcp* α -phase of titanium got transformed into hexagonal ω -phase, following a 2.2 GeV uranium ion bombardment at 20 K. Later on there were many reports explaining such a transformation. For instance, yttria was found to transform from the cubic to the monoclinic phase after irradiation with 1-GeV Ta or 0.86-GeV Pb ions[56]. Another example is the

transformation of the $\text{Bi}_2\text{Sr}_2\text{Ca}_1\text{Cu}_2\text{O}_y$ phase to the $\text{Bi}_2\text{Sr}_2\text{Ca}_2\text{Cu}_3\text{O}_y$ phase after irradiation with 100 MeV ^{57}Fe ions at 100 K[57].

The classic examples for crystalline-to-crystalline phase transitions are that of zirconia and hafnia. It was found that both zirconia and hafnia transform from the monoclinic to the tetragonal phase upon ion irradiation. There are many reports in this regard[58–63]. Many different energetic atomic species induce the phase transitions in both zirconia and hafnia, for example, zirconia showed the transition when irradiated with 595 MeV Xe and hafnia was found to change its phase while irradiated with 250 MeV I – both at room temperature. An interesting feature of this phase transition is that the obtained tetragonal phase is stable at room temperature for more than several months. This is in contrast with the fact that the tetragonal phase is thermodynamically stable only at temperatures of ~1400–2600 K for pure zirconia and at temperatures of ~2000–2900 K for pure hafnia. In both materials the kinetics of the phase transition is related to a mechanism involving a double ion impact[58].

1.3.5. Inert gas bubble formation in materials

Inert gases, when introduced into any material, present a unique situation since they do not form compounds with the material. Their presence in aggregation can result in a significant degradation of material properties depending on the concentration of the gas atoms. The location of the inert atoms – in grain boundaries, in dislocations or in the particle-matrix interface – influences the property of the material.

Due to their inert nature and low solubility, they preferably aggregate into the form of bubbles. Inert gas bubbles have been noticed in metals, alloys[64–68], oxides[69–73], carbides[74], etc. Chen *et al.*[68] have studied the bubble-loop complexes in ferritic ODS alloy (PM2000) irradiated with 24 MeV α -particles. The bright-field TEM images in Figure 1.8 showed the bubble and ODS particle complexes in the sample, at 773 K, as observed by Chen *et al.*[68].

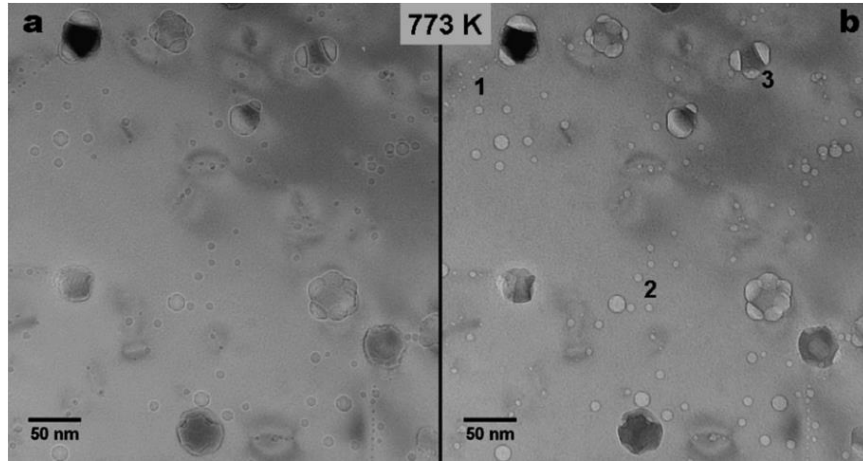


Figure 1.8 Bright-field TEM images showing the bubble and the oxide particle complexes in ferritic ODS alloy (PM2000) irradiated with 24 MeV α -particles, at 773 K, (a) at over-focus and (b) at under-focus. (Ref. [68])

The formation of void and gas bubble superlattices is yet another intriguing nanoscale phenomenon. This phenomenon has been a subject of interest ever since the discovery that helium bubbles in molybdenum could form a *bcc* lattice[75]. There are many reports on bubble lattices in metals starting from the ‘krypton bubble lattice alignment’ inside titanium[76] upto a recent report on helium bubble lattices in tungston[77] (shown in Figure 1.9).

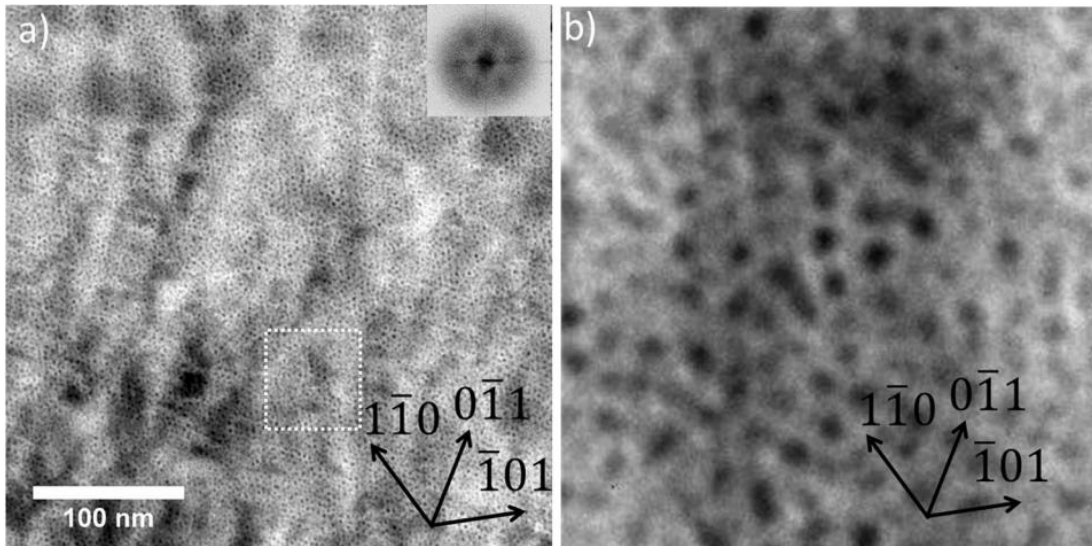


Figure 1.9 W sample irradiated with 15 keV He ions at 773 K up to 1.1×10^{17} ions/cm² to 3 dpa. TEM image of a He bubble lattice close to the [111] zone axis with inset showing the corresponding FFT; (b) shows the enlarged region of white dashed box in (a). (Ref.[77])

In addition to the ion irradiation effects listed above, there are reports on ion beam induced plastic deformations also. It has been observed in metallic glasses[78], glasses[79], silicon[80] and other amorphous materials[81].

1.4. Radiation effects in oxide materials

The radiation response of oxide based ceramics are very different from that of metals and alloys[3,10]. The difference emanates from the factors such as the complex nature of bonds, the complex crystal structures, the presence of different types of atomic species, etc. In many cases, complex chemistry, degree of inherent disordering[82] and crystal size of the oxides[83] are important factors that affect the radiation behaviour of complex ceramics.

Unlike metals, ceramic oxides consists of two or more number of atoms in its unit cell and so the nature of bond between any two atomic species will be different. The complex crystal structures of oxides consist of many sublattices populated by atoms with different masses and valency. Different atomic species in the lattice will have different displacement threshold energies (E_d). The nuclear and electronic stopping ratio also differs significantly between the sublattices[11]. Therefore, ceramics show difference in their response to radiation induced defect production, defect aggregation and defect recovery processes.

1.4.1. Radiation effects in oxide based fuel materials

A variety of materials have been used, or contemplated, as fuel materials. Fissile actinide isotopes have either been incorporated into stable metal alloys, or into refractory ceramics (oxides, nitrides, carbides, or silicides), to be used as fuel. Other, more complex materials, like *cercer* (ceramic–ceramic combinations) or *cermet* (ceramic–metal) composites, have also been investigated for nuclear fuel. Metal alloy fuels carry the drawback of a low melting temperature, moreover they form eutectics that further bring the melting point down, and so their use would be restricted to below 1000 °C. Oxides, on the other hand, are highly stable, and prove

highly refractory, exhibiting melting temperatures higher than 2,500 °C. Presently oxides of actinides (urania, plutonia and thoria) are used on an industrial scale, as fuel for nuclear reactors.

Among them, thoria has drawn attention as a potential source of nuclear energy since the 1950s due to several attractive features of the Th–U²³³ fuel cycle and because of its abundance on earth. The use of thorium assumes greater significance in India's context, as India's uranium resources are limited and thorium resources are vast[84]. Thoria is a highly stable oxide, and exhibits higher thermal conductivity, higher melting temperature, higher corrosion resistance and lower thermal expansion compared to urania[85].

Inert gas induced swelling is one of the major concern in the case of nuclear fuel materials. The swelling due to the accumulation of inert gases (Kr, Xe and He) leads to degradation of thermal conductivity of the fuel[5–7]. The behaviour of inert gases (Kr, Xe and He) inside the nuclear fuel materials (urania, thoria and ceria) have been characterized by many authors based on experiments and computer simulations.

Garrido *et al.*[86], experimentally found that the implanted helium (100 keV ³He⁺ ions) takes octahedral interstitial position in UO₂ single crystal (*fcc*), using ion channeling, nuclear reaction analysis experiments and Rutherford backscattering spectrometry. The calculations by Dąbrowski *et al.*[87] also showed that helium occupies octahedral interstitial position in the perfect *fcc* lattice of urania and thoria. DFT simulations by Yun *et al.*[88] and Shao *et al.*[89] show that helium atoms may tend to form small (3-4-atom) clusters around the octahedral interstitial site in urania[88] and thoria[89]. Dąbrowski *et al.*[87] further showed that helium atom located in the octahedral interstitial site would cause a local increase (~0.3%) in the lattice parameter in both urania and thoria.

Roudil *et al.*[90] measured the activation energy (E_a) and the diffusion coefficient (D) for the diffusion of helium in urania by nuclear reaction analysis

((*d,p*) reaction) and found that E_a was ~ 2 eV and D was just $2.9 \times 10^{-17} \text{ m}^2 \text{ s}^{-1}$ at 1000°C . Similarly, Lu *et al.*[91] have reported that helium has a very large diffusion barrier (3.34 eV) in perfect thoria lattice. Dąbrowski *et al.*[87] have noticed that helium has a small diffusion coefficient ($10^{-48} \text{ cm}^2 \text{ s}^{-1}$ at 300 K) in perfect thoria.

The calculations done by Grimes *et al.*[92] shows that the diffusion barrier for the helium atom trapped in the interstitial sites in perfect UO_2 is large (3.8 eV) whereas the diffusion barriers are significantly reduced when the diffusion is assisted by oxygen vacancy (0.38 eV) or uranium vacancy (0.24 eV). This indicates that it is difficult for the helium atom to diffuse in perfect urania or thoria.

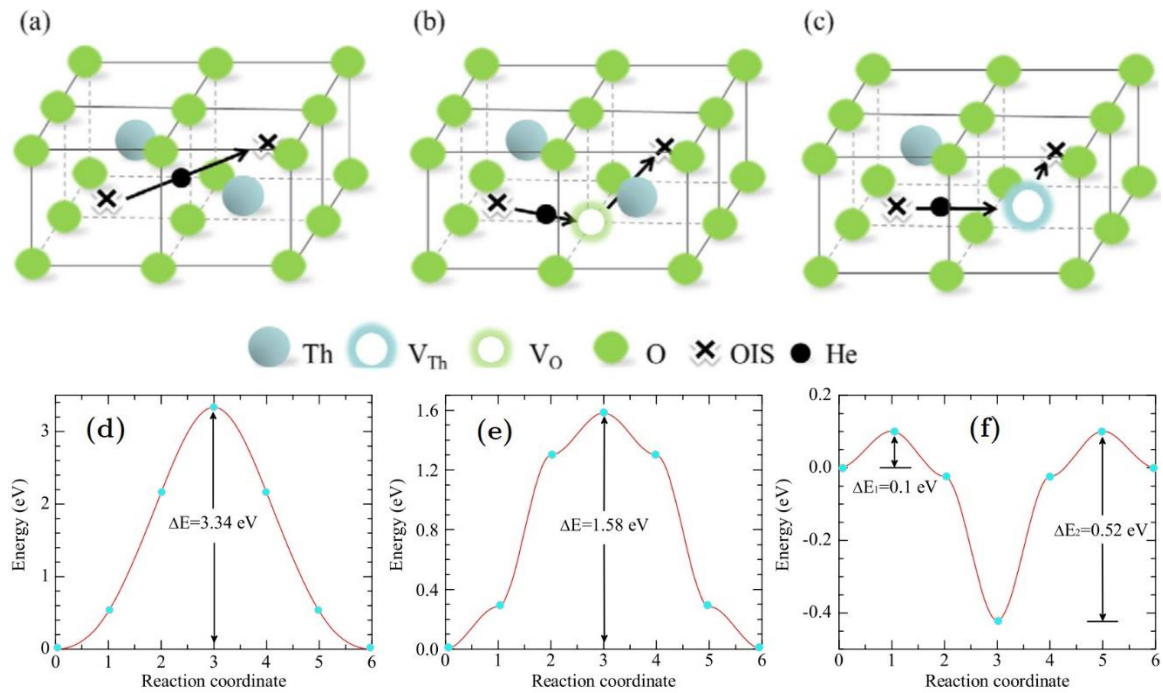


Figure 1.10 Diffusion pathways for a helium atom from one octahedral interstitial site to another octahedral interstitial site (a) directly in intrinsic thoria, (b), through an oxygen vacancy (c) and through a thorium vacancy in defective thoria. (d), (e) and (f) are the energy profiles corresponding to the diffusion mechanism (a), (b) and (c) respectively. (adapted from Ref.[91])

Using density functional theory (DFT) calculations, Lu *et al.*[91] have shown that helium diffusion is possible in thoria lattice only in the presence of Th-vacancy, where the energy barrier is just 0.52 eV (Figure 1.10), and that diffusion might lead to helium aggregation causing failure of fuel. According to the review by Trocellier

et al.[93], helium aggregation in urania or plutonia can lead to microscopic and macroscopic swelling, due to the low solubility of helium, which may result in cracking of the material.

Mohun *et al.*[94] studied the mechanism of defect formation in urania and thoria due to α particles, by irradiating with 21 MeV He^{2+} ions. Raman scattering and luminescence results showed that although UO_2 , ThO_2 and PuO_2 share similar characteristics, the mechanism of defect creation in ThO_2 is totally different.

The minimum helium concentration required to form bubbles in oxide materials (like MgO [95], borosilicate glass[96]) is around 5 to 12 *at%*. In yttria stabilized zirconia, Yang *et al.*[97] have noticed that, helium bubbles nucleate only when the concentration of He exceeds ~ 17 *at%*. All the above DFT calculations assume small concentrations of helium (few *at%*) in thoria, but there is no experimental study on the behaviour of small concentrations of helium in thoria.

In the present thesis, the behaviour of small concentration (~ 4 *at%*) of helium inside thoria was studied using experiments (Grazing Incidence X-Ray Diffraction (GIXRD) and Transmission Electron Microscopy (TEM)). Further, DFT calculations were used to understand and interpret the experimental observations.

1.4.2. Radiation response of rare earth titanates

The core structural materials in the reactor require properties such as low activation, adequate strength, toughness, and resistance to swelling and creep due to radiation[98,99]. The viability of nuclear energy critically depends on the development of new, high-performance structural materials that can support extended component lifetimes under extremely hostile conditions[100].

Oxide dispersion strengthened (ODS) steels is considered as the most promising structural material for advanced nuclear systems. The enhanced creep resistance of the ODS steels at high temperature and their radiation resistance, originate from the stabilized oxide nanoclusters[101], which are the nanoparticles of yttrium titanates (*i.e.*, complexes of Y-Ti-O). The composition of the oxide particles

in ODS steels is predominantly $Y_2Ti_2O_7$ or Y_2TiO_5 [102–106], both in the case of commercial ODS alloys, like 9Cr-ODS, MA957[13], MA956 and PM2000, and in the case of laboratory alloys, like 12YWT16 and 14YWT. Small sized nanoclusters exist as coherent solute-enriched-clusters whereas larger particles have their stoichiometry close to the phases of $Y_2Ti_2O_7$ and Y_2TiO_5 [107,108]. Detailed experimental analysis, by London *et al.*[109,110], on the composition of the oxide particles in the model ODS alloys, using atom probe tomography (APT), also revealed the predominance of only these two stoichiometries. Moreover, it was understood from DFT calculations[111] that these two systems have relatively more negative heat of formation when compared with the other possible stoichiometries of Y, Ti and O.

As far as the radiation resistance is concerned, these two systems have good radiation resistance, since both of them – the pyrochlore systems of type $A_2B_2O_7$ [112,113] and the orthorhombic rare-earth titanate systems Ln_2TiO_5 [114] – have complex crystal structure. In order to further describe and control the stability and the strengthening mechanism of these systems, an improved understanding of their phase stability and radiation response is necessary.

The stability of the oxide particles (of Y, Ti and O) eventually depends on the strength and the nature of the metal–oxygen (M–O) bonds in these oxide particles. The M–O bond strength changes with their structure and stoichiometry. The degree of covalency in the M–O bonds in $Y_2Ti_2O_7$ and Y_2TiO_5 were earlier compared by Jiang *et al.*[104], using DFT calculations and it was reported that the Ti–O bonds exhibit higher covalency than the Y–O bonds, even though ionic bonding dominates in both the oxides. Temperature dependence of the critical amorphization dose in different rare-earth titanate pyrochlores have been experimentally studied by Lian *et al.*[113] and Zhang *et al.*[114]. The critical amorphization temperature (T_c) for $Y_2Ti_2O_7$ and Y_2TiO_5 are found to be 780 K[113] and 623 K[114] respectively.

The T_c of Y_2TiO_5 is lower than that of $Y_2Ti_2O_7$, which implies that accommodation of ion-induced defects is much enhanced in Y_2TiO_5 as compared to $Y_2Ti_2O_7$.

There is no experimental study especially to compare the nature of the M-O bonds in $Y_2Ti_2O_7$ and Y_2TiO_5 . The comparison of the strength and the nature of the M-O bonds in these two oxide particles ($Y_2Ti_2O_7$, and Y_2TiO_5) can help in deciding the composition of the minor alloying elements Y and Ti, which may have a significant impact on the designing of the ODS steels.

1.4.3. Radiation damage in oxide glasses used as wasteform

Borosilicate glass is the primary choice of material for the immobilization of nuclear waste[14]. Ceramic oxide materials like synroc, titania (in the form of glass-ceramic composites) are also proposed as an alternative wasteform[17,115]. The aqueous high level waste (HLW) originating from fast reactors is largely different from that of thermal reactors, since it consists of minor actinides, noble metals volatile fission products, rare earths and heavy metals (like Mo and Cr) in higher concentrations. The low solubility of heavy metals in borosilicate glasses make them not suitable for disposing the HLW from fast reactors.

One alternative wasteform proposed for the disposal of the fast reactor wastes, is iron phosphate glasses IPG[15,16,116]. They have good glass forming ability, very high waste loading and favourable chemical stability[117–120]. The density of iron phosphate vitreous wasteform (3.2 g/cc) is 25% higher than that of borosilicate wasteform for the same amount of waste immobilization; consequently its volume is 25% lower than that of borosilicate waste form. The melts of IPG wasteform are produced at lower temperatures (<1273 K) than BSG (1423 K)[121], and they homogenize in shorter durations, because of their high fluidity. The IPG with the particular composition of 40 mol% Fe_2O_3 and 60 mol% P_2O_5 , has been identified as the promising composition, which is chemically more durable[122].

The major issue, while disposing nuclear waste in glass matrices, is the damage in the glass matrix due to the ballistic processes caused by atomic

displacements due to α -particles (4.5 to 5.5 MeV) and the recoiling of heavy nuclei (70 to 100 keV) resulting from actinide decay. Figure 1.11 shows the cumulative irradiation damage (in terms of *dpa*) generated by β -decay and α -decay as a function of storage time in multiphase ceramics or glass-ceramics. β -decay is the primary source of radiation during the first 500 years of storage, as it originates from the shorter-lived fission products. α -decay is generally dominant at longer times owing to the long half-lives of the actinides and their daughter products.

The concern is whether the damage due to the α -decay events (or the ion irradiation) affects the relaxation processes in the glass[123], e.g., crystallization of the glass. Nucleation of crystals modifies the leaching rate. Therefore, studies on the radiation induced relaxation processes in the wastefoms help to improve the material.

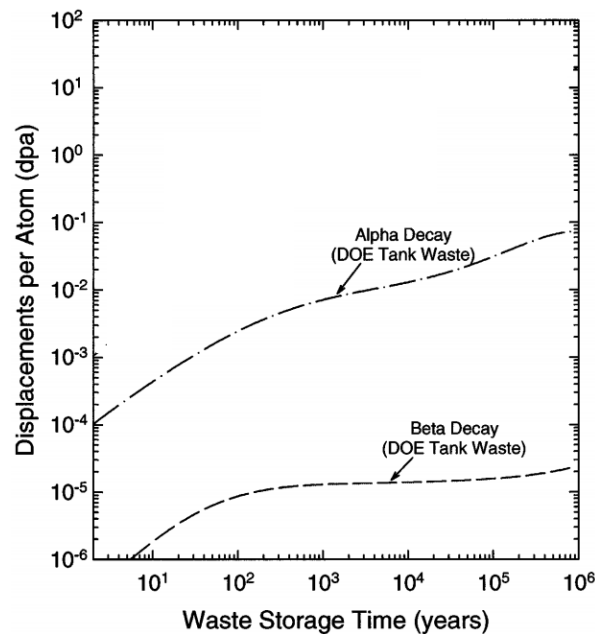


Figure 1.11 Irradiation damage (relative number of displacements – *dpa*) generated by β -decay and α -decay events in typical ceramics containing tank waste of DoE (USA). Courtesy Ref[17].

Many reports are available on radiation damage studies on silicon based glasses[124]. But that cannot be extrapolated to phosphate glasses. It is mainly because of the fundamental difference in the chemical nature of the two glasses;

silicate glasses are based on 4-corner sharing tetrahedral network, whereas phosphate glasses are generally 3-corner sharing tetrahedral network.

Another type of irradiation induced damage in IPG is the variation in the concentration of $\text{Fe}^{2+}/\text{Fe}^{3+}$ ions. It is evident from the literature[125] that as the concentration of Fe^{2+} increases in IPG, the density also increases for the same atomic composition of IPG. It has been experimentally noticed in IPG (using Mössbauer spectroscopy[126]), that when the melting temperature of IPG is increased from 1423 to 1673 K, the density of the glass increases along with the increase in concentration of Fe^{2+} . More importantly, the IPG used in their work, with 40 mol% Fe_2O_3 60 mol% P_2O_5 , (the promising composition for the purpose[127]), is found to change its density depending on the concentration of Fe^{2+} in the glass[125,126].

Very few reports are available regarding the irradiation effects in IPG. Sun *et al.*[128] have reported the effects of electron beam and ion beam irradiation on IPG. Electron beam irradiation leads to the formation of Fe-rich and pure P phases whereas the ultra-low energy (3.5 keV Ar^+) ion irradiation on IPG leads to the formation of Fe/FeO nanoparticles as a result of preferential sputtering during ion irradiation, *i.e.*, P and O were sputtered out at a higher rate than Fe. Awazu *et al.*[129] have reported that swift heavy ion irradiation on zinc phosphate glass shows the formation of ion tracks and leads to reduction in the number of bridging O atoms.

In this context, in the present thesis, the stability of the glass phase of IPG against irradiation induced damages were studied by doing self-ion (4 MeV O^+ ion) irradiation experiments on IPG samples and analyzing the microstructural changes using high resolution transmission electron microscopy (HRTEM). Further, the qualitative change in the charge state of Fe, due to irradiation, was studied using the change in the pre-edge features in the Fe L₂₃-edge in X-ray absorption spectroscopy (XAS).

1.5. Objective and overview of the thesis

The present thesis deals with the studies on the radiation stability of oxide ceramics: (i) thorium dioxide or thoria (ThO_2), a nuclear fuel material, (ii) yttrium titanates ($\text{Y}_2\text{Ti}_2\text{O}_7$ and Y_2TiO_5), the oxide-dispersoids used for strengthening the structural material, (iii) Iron Phosphate Glass (IPG), the material proposed for the disposal of high level nuclear waste from fast reactors.

This thesis is organized into six chapters. The contents of the forthcoming chapters are summarized below.

Chapter 2 explains the sample preparation methods by which the oxide ceramic materials were synthesized. It also explains the experimental and the computational methods used in the thesis to characterize the materials and to understand the effect of ion irradiation. It explains the working principles of ion irradiation facilities and the characterization techniques such as grazing incidence X-ray diffraction (GIXRD), transmission electron microscopy (TEM), scanning electron microscopy (SEM) Raman spectroscopy and the core level spectroscopic techniques (X-ray absorption spectroscopy (XAS) and electron energy loss spectroscopy (EELS)). The fundamentals of density functional theory based codes (VASP & CASTEP) is also explained.

Chapter 3 deals with the behaviour of the inert gas helium in thoria. Helium was implanted in thoria using low energy helium (100 keV He^+) ion beam and the changes in the microstructure were analysed using grazing incidence X-ray diffraction (GIXRD) and transmission electron microscopy (TEM). Both the experiments showed that there is lattice expansion (1.07 %) in isolated nanometric regions in the surface of the sample upon irradiation. First principle calculations showed that energetics prefer aggregation and ordering of helium in the octahedral interstitial sites in thoria lattice, and the ordered aggregation eventually results in lattice expansion of 1.25% which is in agreement with the expansion observed

experimentally. The experiments and calculations confirm that the lattice expansion is due to the ordering of helium atoms in the octahedral interstitial sites of thoria.

Chapter 4: This chapter deals with the characterization of radiation stability and bond strengths of the oxide nanodispersoids used for strengthening the ODS steels. The irradiation stability of both the yttrium titanates were compared by irradiating both the oxide samples with 70 keV Kr^+ ions at room temperature. High resolution TEM images showed the presence of stacking faults in $\text{Y}_2\text{Ti}_2\text{O}_7$ and faceted bubbles of krypton in Y_2TiO_5 , upon irradiation at room temperature. The experiments support the argument that $\text{Y}_2\text{Ti}_2\text{O}_7$ has better radiation resistance compared to Y_2TiO_5 .

Further, this chapter quantitatively compares the strengths of M-O bonds in Y_2TiO_5 and $\text{Y}_2\text{Ti}_2\text{O}_7$ by comparing the pre-edge features in O K-edge in EELS and using the electron charge densities calculated using DFT. The pre-edge features in the O-K edge of transition metal (TM) oxides manifest the effect of crystal field splitting in the Ti $3d$ orbital. EELS analysis showed that the overlap of Ti $3d$ orbital and O $2p$ orbital is less dominant in Y_2TiO_5 compared to $\text{Y}_2\text{Ti}_2\text{O}_7$. The EELS and DFT results showed that Ti-O bonds in $\text{Y}_2\text{Ti}_2\text{O}_7$ is more covalent compared to Y_2TiO_5 and Ti-O bonds are more covalent than Y-O bonds in both the yttrium titanates. Hence it is suggested that $\text{Y}_2\text{Ti}_2\text{O}_7$ is better radiation resistant than Y_2TiO_5 .

Chapter 5 analyses irradiation induced relaxation processes in IPG and irradiation induced changes in the charge state of Fe atom. IPG samples were irradiated with 4 MeV O^+ (self) ion, which introduces strain required for inducing relaxation processes. TEM showed the formation of nanocrystals of $\text{Fe}_4(\text{P}_2\text{O}_7)_3$, $\text{Fe}(\text{PO}_3)_3$ and P_2O_5 upon irradiation, consistent with the earlier reports. The mechanism of crystallization was explained based on stress driven crystallization mechanism.

Changes in the charge state of Fe atom upon ion irradiation is analysed using X-ray absorption spectra. XAS (O K-edge and Fe L₂₃-edge) analysis of the pre-edge features clearly show that the concentration of Fe²⁺ has increased and the concentration of Fe³⁺ has decreased upon 4 MeV O⁺ irradiation. The rise in the population of Fe²⁺ increases the viscosity of IPG, which in turn increases the glass forming ability.

Chapter 6 gives the summary and the salient features of the thesis and explains the scope for the future work.

Chapter 2

Experimental Techniques

This chapter explains the different techniques used for preparing different oxide samples, whose radiation responses were studied in this thesis. The technical details about the particle accelerator facilities which were used for ion implantation/irradiation are also given in this chapter.

The present thesis uses various material characterization techniques, which can be classified into diffraction techniques, microscopic techniques and spectroscopic techniques. X-ray diffraction (XRD), grazing incidence X-ray diffraction (GIXRD) and electron diffraction techniques were used to characterize the changes in the crystal structures of the specimen. High resolution transmission electron microscopy (HRTEM), is the microscopic technique used in this thesis to understand the changes in the microstructure of the specimen. Under the category of spectroscopic techniques, energy-dispersive X-ray spectroscopy (EDS), electron energy loss spectroscopy (EELS), Raman spectroscopy, and X-ray absorption spectroscopy (XAS) were employed to analyse various chemical and bonding nature of the specimen. The present thesis also uses computational methods based on density functional theory and molecular dynamics. This chapter briefly explains the working principle and the capabilities of these characterization techniques and computational methods.

2.1. Sample preparation methods

2.1.1. Solid state reaction method

A variety of methods exist for the synthesis of ceramic powder samples, like solid state reaction technique, sol-gel technique, co-precipitation technique, hydrothermal method, chemical/physical vapor deposition technique, etc. These methods are broadly categorized into mechanical methods and chemical methods.

Solid-state reactions method is a mechanical method for the synthesis of ceramic oxides.

Solid state reaction (SSR) is the conventional method used for the synthesis of many ceramic materials. It provides large range of selection of starting materials like, oxides, nitrates, carbonates, etc. Since, solids do not react with each other at room temperature (RT), it is necessary to heat them at elevated temperatures as high as up to 1500 °C for the proper reaction to take place at appreciable rate. Thus, both, thermodynamic and kinetic factors are important in SSR. The major advantage of SSR method is, the final product in solid form is structurally pure with the desired properties depending on the final sintering temperatures.

While synthesizing sample in SSR method, high purity starting materials (precursors) should be used (purity > 99.95%). The precursor materials need to be grained finely, since the reaction rate increases with increase in surface area. Then they should be taken in appropriate stoichiometry and mixed thoroughly using agate mortar and pestle or ball milling.

The solid powder mixture should be heated at elevated temperatures in air using furnace (calcination). The calcination process should be repeated three or more times with intermittent grinding. The temperature should be systematically increased at subsequent calcination. Tamman's Rule[130] says that extensive reaction will not occur until the temperature reaches at least $\frac{2}{3}$ of the melting point of one or more of the reactants.

The calcinated powder should be pelletized to form uniform and compact pellets and should again be sintered at more elevated temperatures (>1300 °C) for prolonged duration.

The advantages of SSR:

- It has higher productivity and lower cost
- A whole range of materials can be synthesized, including mixed metal oxides, sulfides, nitrides, aluminosilicates, etc.;

- There will not be impurity phase in the final product except the precursors.

The disadvantages of SSR:

- It requires very high temperatures (500-2000 °C); since it is diffusion limited,
- The reaction would proceed very slowly;
- Increasing the temperature speeds up the reaction since it increases the diffusion rate, but the desired compound may decompose at high temperatures;

In the present thesis, the yttrium titanate samples $Y_2Ti_2O_7$ and Y_2TiO_5 were prepared by solid state reaction method. The precursor materials used were Y_2O_3 (with purity: 99.995% from *Alfa Aesar*) and TiO_2 (with purity: 99.5% from *Merck*). The melting point of Y_2O_3 is 2425 °C and that of TiO_2 is 1843 °C. The precursor materials were ground thoroughly to ensure homogenous mixture and the powders were pelletized using a hydraulic press to increase the number of crystallites in contact and then the samples were heat treated.

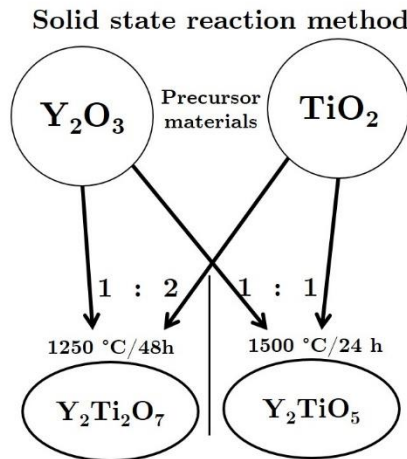


Figure 2.1 Schematic illustration of the solid state reaction method used to synthesize $Y_2Ti_2O_7$ and Y_2TiO_5

In order to synthesize $Y_2Ti_2O_7$, Y_2O_3 and TiO_2 were taken in the molecular ratio of 1:2; the mixture was calcined at 1250 °C in air for 48 hours following the recipe proposed in Ref.[131]. The synthesis procedure is illustrated schematically in Figure 2.1. Y_2TiO_5 was synthesized with the same precursors Y_2O_3 and TiO_2 taken in the molecular ratio 1:1. The mixture was calcined at 1500 °C in air for 24 hours

as per the procedure reported in[132]. The sample was ground well and the calcination process was repeated 3 times to enable complete reaction. The pellets were finally sintered at 900 °C for 8 hours. The sintered pellets were used for the ion irradiation experiments.

2.1.2. Gel combustion method

Combustion synthesis is an easy and convenient method for the preparation of a variety of advanced ceramics, catalysts and nano materials. In this technique, based on the principles of the fuel chemistry, a thermally induced redox reaction takes place between an oxidant and a fuel. Many types of combustion synthesis exist which differ mainly in the physical state of the reactants or in the combustion modality. By combustion-based methods, it is possible to produce monophasic nanopowders with homogeneous microstructure, at lower temperatures or shorter reaction times, if compared with other conventional methods like solid state synthesis or nitrate method[133]. Today it has become a very popular approach for preparation of nanomaterials and a number of important breakthroughs in this field have been made[134,135].

Advantages of sol-gel auto combustion process:

10. Low cost and low temperature process.
11. Better control of stoichiometry.
12. Crystallite size of the final oxide products is invariably in the nanometer range.
13. Exothermic reaction makes product almost instantaneously.
14. Products have high purity, better homogeneity and high surface area

Disadvantages of sol-gel auto combustion process:

1. Possibility of contamination due to carbonaceous residue, particle agglomeration
2. There is no control on particle morphology
3. Understanding of combustion behaviour is needed to perform the controlled combustion in order to get final products with desired properties
4. There is possibility of violent combustion reaction

Citrate–nitrate auto-combustion synthesis is a very popular solution combustion method[136], where citric acid the fuel is and metal nitrates are used as metal and oxidant source.

The gel-combustion synthesis involves exothermic burning reaction between an oxidizing agent (metal nitrates or acetates) and an organic fuel (glycerine, citric acid, sucrose, etc.) The materials are initially mixed in a definite proportion to form a homogenous aqueous solution, followed by gelation and combustion.



Figure 2.2 The photographs depicting the stages in the synthesis of thoria from the precursors thorium nitrate and citric acid, by citrate gel combustion method. (a) the gel before combustion, (b) combustion and (c) after combustion.

In the present work, thoria (ThO_2) was synthesized by the citrate gel-combustion method, as reported in Ref.[137]. The precursor materials used were thorium nitrate and citric acid. Citrate gel-combustion method involves combustion of the mixture of precursors. The combustion gives a porous, fluffy, crystalline and highly free flowing powder. The powder was then calcined at 973 K for 5 hours in air to remove the residual carbon. The pellets were prepared with a pressure of 300 MPa and sintered at 1773 K.

2.1.3. Glass preparation – Melt-Quench method

Melt quenching technique was the first glass preparation technique used in glass industry as well as in research field, while there are presently few more techniques like chemical vapor deposition and sol gel method[138]. One of the important features of the melt quenching technique is the flexibility of preparing a large number of compositions of glass of silicate, borate, phosphate, oxide or non-

oxide systems. The disadvantage is the lack of purity of the prepared glass sample. In order to avoid contamination, crucibles made of noble metals like gold, platinum are generally used.

Glass formation is a matter of bypassing the process of crystallization and almost all materials can be prepared as amorphous solids by quick cooling. The rate of cooling varies enormously from material to material. To become an amorphous solid, the material is cooled below a critical temperature called the glass-transition temperature (T_g). The glass transition occurs when the supercooled liquid freezes into an amorphous solid with no abrupt discontinuity in volume, near the glass transition temperature.

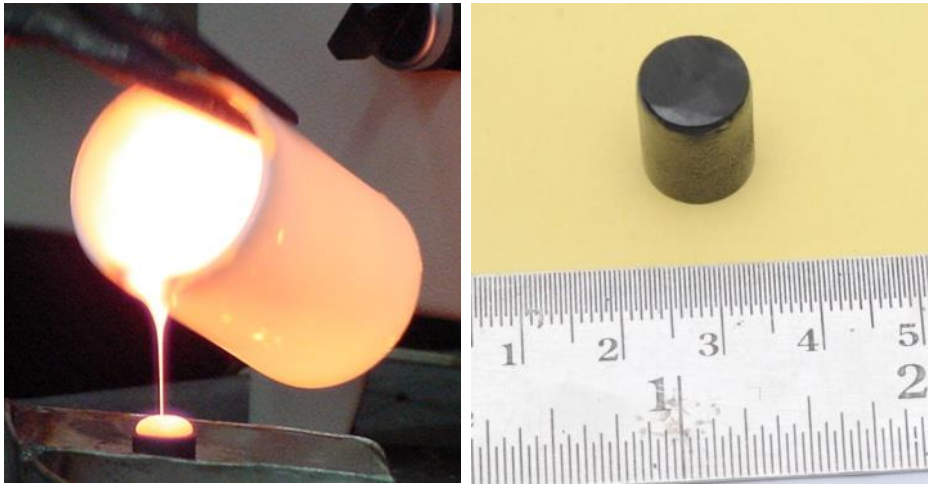


Figure 2.3 (a) Photograph of IPG glass melt, while pouring (b) Photograph of the IPG glass sample

In the present thesis, iron phosphate glass (IPG) was synthesized using melt-quench method.

2.2. Accelerator facilities

In the present thesis, radiation damage was simulated in the ceramic oxide samples using energetic ion beams. The ion irradiations were carried out in different accelerators. The details of the accelerators are given below.

2.2.1. 1.7 MV Tandetron accelerator

The 1.7 MV Tandetron accelerator has the “tandem” configuration. In the tandem setup, negative ions from the source are first accelerated to the high voltage terminal. Then the negative ions are converted to positive ions while passing through a stripper canal in the centre of the accelerator. The positive ions get acceleration, when it travels beyond the stripper canal towards the ground potential on the other side. The accelerator is filled with SF₆ gas for high voltage isolation. Tandetron accelerator has two advantages namely the advantage of using the same high voltage for accelerating the ions twice and the advantage of having both the ion injection system and the target at the ground potential.



Figure 2.4 Photograph of 1.7 MV Tandetron accelerator and the beamlines.

The beam injection system of the accelerator has two ion sources: (i) a high brightness duoplasmatron ion source for the production of H⁺ and He⁺ ions and (ii) a sputter source SNICS (Source of Negative Ions by Cesium Sputtering) capable of producing negative ions of almost all elements. A 90° mass analyzing magnet

facilitates the injection of the ion beam from either of the ion sources into the accelerator. The mass analyzing magnet has a resolution ($m/\Delta m$) 190.

The entire accelerating structure consisting of the accelerating tube, the high voltage terminal and the power supply is enclosed in a pressure vessel filled with SF₆ gas at a pressure of 6 kg/cm² for achieving high voltage insulation. The Cockroft-Walton type solid state power supply used for the generation of high voltage, allows the variation of the terminal voltage from 100 kV to 1.7 MV with a stability of ± 100 V. The accelerating tubes are maintained at a pressure of $\sim 2 \times 10^{-7}$ mbar and a turbomolecular pump has been installed at the high voltage terminal for the recirculation of the stripper gas. The accelerated ions emerging on the high energy side of the machine are focused by electrostatic quadrupole lens. The photograph of the Tandetron accelerator along with its beamlines is shown in Figure 2.4.

A high energy switching magnet selects the beam according to the energy of the ions and switches the beam to the experimental ports located at $\pm 10^\circ$ and $\pm 30^\circ$ angular positions. An implantation beam line with the beam sweep system, neutral trap, beam profile monitor and retractable slits for beam collimation has been installed at the 10° port of the switching magnet. The maximum energy achievable, is decided by the charge state (q) of the ions at the terminal after stripping and the terminal voltage (V), for $E = V(1+q)$. A UHV compatible, high-temperature irradiation cum ion beam analysis chamber has been installed at another 10° beam line.

2.2.2. 150 kV ion accelerator

A schematic diagram of the 150 kV accelerator is shown in Figure 2.5. The facility is indigenously developed at IGCAR. The 150 kV ion accelerator consists of a gaseous radio frequency (RF) plasma source at a pressure of 10^{-4} mbar in which the desired gaseous ions are generated. The ions are extracted from the ion source and accelerated to desired voltage, in the range of 30-150 kV. The ions are mass

analyzed by a 45° electromagnetic mass analyzer. The analyzed ion beam is collimated and allowed to impinge on the sample kept in the irradiation chamber. The target chamber is maintained at an ultra-high vacuum of 10^{-7} to 10^{-8} mbar using a turbomolecular pump.

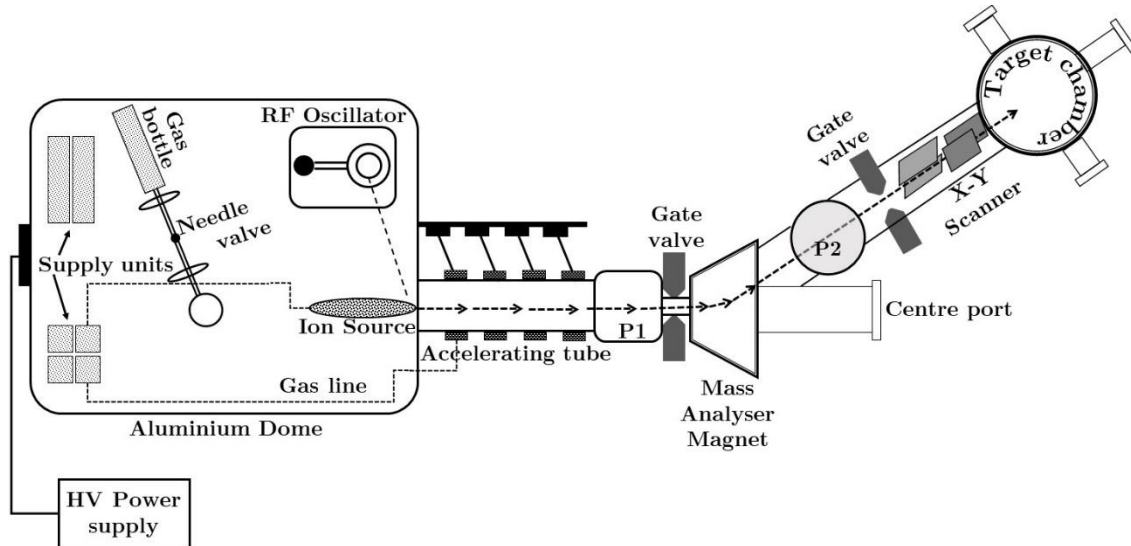


Figure 2.5 (Top) The schematic diagram and (Bottom) the photograph of the 150 kV accelerator facility.

The sample is mounted on a copper block in the sample manipulator and is insulated from the rest of the chamber, to facilitate beam current measurement. The beam current and the dose (in ions/cm²) are measured using a current integrator. A secondary electron trap is used to eliminate the error in the beam

current measurement caused by the emission of secondary electrons from the target. The secondary electron trap consists of a thin metallic cylinder surrounding the sample holder with appropriate holes cut in it for the beam entry and sample viewing. A potential of approximately (-40 V) is applied on the trap for secondary electron suppression. A liquid nitrogen trap was fixed to trap the organic contaminants and hence to maintain a clean vacuum.

Though the accelerator has the capability to deliver the ion beam current of the order of tens of μA , a low current ($< 1 \mu\text{A}$) was maintained during irradiation to avoid the beam heating of the target material. According to the need of the beam size the collimator diameter was varied from 8.5 mm to 14 mm. Most of the irradiation were carried out at room temperature and a few of the irradiations were carried out at 110 K.

2.3. Diffraction techniques

2.3.1. X-ray diffraction

X-ray diffraction (XRD) is one of the most important non-destructive technique used for materials characterization. It is mainly used for identification of crystal structure of the material and for quantitative phase analysis. X-ray diffraction techniques have, therefore, been widely used as an indispensable means in materials research.

The Bragg equation is the key in understanding X-ray diffraction.

$$n\lambda = 2d \sin\theta$$

Eqn. 2.1

where, n is an integer, λ is the characteristic wavelength of the X-ray, d is the interplanar spacing between rows of atoms, and θ is the angle of the X-ray beam with respect to these planes (Figure 2.6). When Bragg condition is satisfied, X-rays scattered by the corresponding planes are in phase and they interfere constructively resulting in a peak in the XRD pattern. The X-ray diffraction pattern basically shows the diffracted intensities as a function of collection angles.

In the present thesis, STOE X-Ray Diffractometer was used for characterization of the samples. It was operated in Bragg Brentano geometry (Figure 2.6(a)). The detector collection angle is from 10° to 90° with a step size of 0.1°.

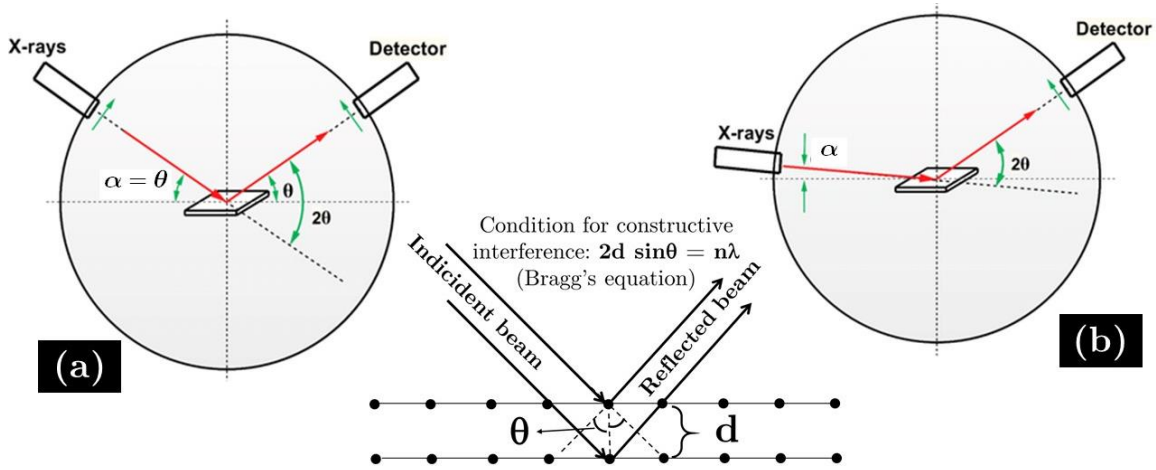


Figure 2.6 Schematic of (a) Bragg-Brentano (θ - 2θ) geometry and (b) GIXRD geometry.

2.3.2. Grazing incidence X-Ray Diffraction

Grazing Incidence X-Ray Diffraction (GIXRD) is a scattering geometry combining the Bragg condition with the conditions for X-ray total external reflection from crystal surfaces. In GIXRD experiments, the incident beam impinges onto the surface of a thin film, at an incident angle of 1° or less. This provides advantage over other diffraction schemes in the studies of thin surface layers, since the penetration depth of X-rays inside the slab is reduced by three orders of magnitude typically from 1-10 μm to 1-10 nm, as explained below.

When X-rays penetrate solid material, its intensity is absorbed by the solid and reduces according to Beer Lambert’s law:

$$I = I_0 \exp(-\mu t) \tag{Eqn. 2.2}$$

where, I_0 is the initial X-ray beam intensity, I is the intensity of the emerging X-ray, μ is the linear mass absorption coefficient of the material and t is the distance travelled by X-ray inside the material.

For an incident angle of α and a particular collection angle of 2θ (as illustrated in Figure 2.7) the total distance travelled by the X-ray inside the material can be written as

$$t = x \operatorname{cosec} 2\theta - \alpha + x \operatorname{cosec}(\alpha) \quad \text{Eqn. 2.3}$$

where x is X-ray probe depth. When 99% of the incident intensity is absorbed, Eqn. 2.2 becomes $\ln 100 = \mu t$ and Eqn. 2.3 becomes

$$x = \frac{\ln 100}{\mu[\operatorname{cosec} 2\theta - \alpha + \operatorname{cosec} \alpha]} \quad \text{Eqn. 2.4}$$

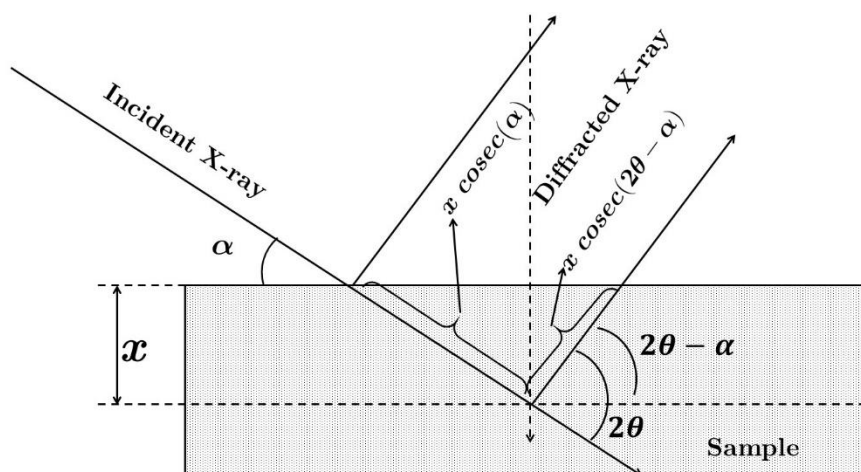


Figure 2.7 Schematic diagram showing the scattering geometry in GIXRD

In the present thesis, ion irradiation is used to simulate the radiation effects in the samples, and the effects are observed near the surface of the sample, within few hundreds of nanometers depth. Hence GIXRD was used to characterize the effects in the surface. The incident angle α is kept very small, as given by Eqn. 2.4, so as to probe the effects of irradiation.

In the present study, Bruker X-ray diffractometer, Model: D8-Discover was used, and Cu $K\alpha$ radiation (1.541 \AA) was used as the probe.

2.3.3. Electron diffraction

When electrons pass through the periodic lattice of a crystal, behaves as a wave and produces diffraction pattern, very much similar to optical diffraction in

gratings and X-rays in crystals. The wavelength of an electron accelerated in a TEM is much smaller than that of the X-rays. The wavelength of electrons is calculated reckoning the relativistic effects as:

$$\lambda = \frac{h}{\sqrt{2m_0eV \left(1 + \frac{eV}{2m_0C^2}\right)}}$$

Eqn. 2.5

where, m_0 is the rest mass of electron, and V is the voltage upto which the electrons are accelerated. So, the wavelength of electrons is much smaller than that of photons (2.5 pm for 200 keV electrons). A consequence of this is that the radius of the Ewald sphere is much larger in electron diffraction experiments than in X-ray diffraction. This allows the diffraction experiment to reveal more of the two-dimensional distribution of reciprocal lattice points. Moreover, electron diffraction has very high spatial resolution (to study small crystals or particles).

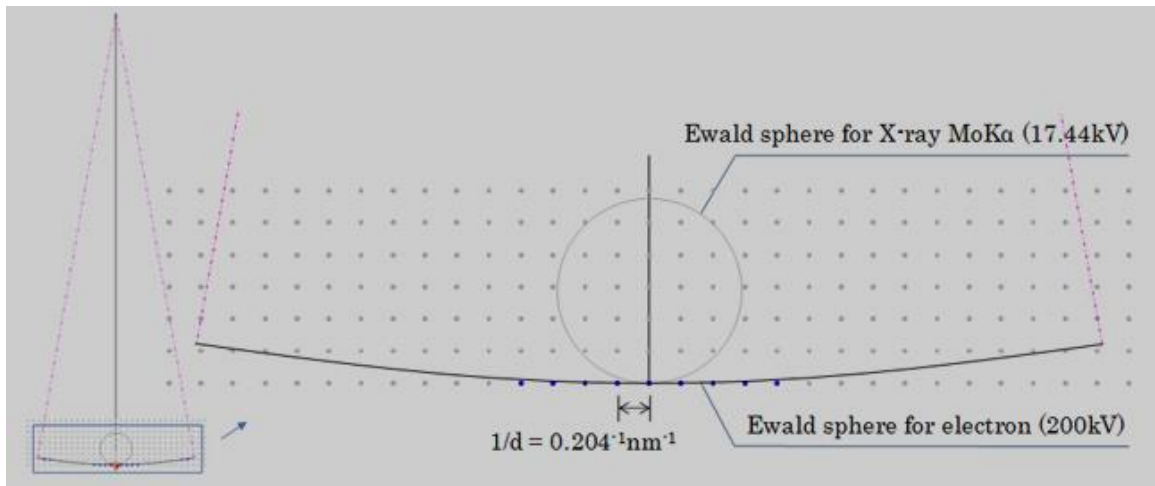


Figure 2.8 Schematic illustration of the change in the size of Ewald sphere (in the reciprocal lattice), due to the variation in the wavelength of X-rays and electrons. (Ref.[139])

The electron diffraction patterns can be used for the identification of: phases and crystal structure types, crystal symmetry and crystal space group determinations, orientation relationships between phases. *i.e.* determining growth directions, interface coherency, identifying defects, determining the ordering behaviour of crystal structures and the site occupancy preferences, etc.

The single crystalline materials show (a) spot pattern or (b) Kikuchi line pattern or (c) a combination of spot and Kikuchi line patterns. The polycrystalline materials exhibit ring pattern. When the grain size of the specimen is extremely fine or completely amorphous, the feature of concentric rings in the pattern disappears and a halo is left around the bright centre spot, which shows that the electrons are scattered randomly by the amorphous structure of specimen. The amorphous and glassy materials are identified by this method.

2.4. Transmission electron microscopy

Historically Transmission Electron Microscopes (TEM) were developed to overcome the limitations in image resolution in optical microscopes, which is imposed by the wavelength of visible light. The probe used in TEMs is high energy electrons whose wavelength is of the order of pm, *e.g.* 200 keV electrons have wavelength of ~ 2.5 pm (as given by *Eqn. 2.5*). Practically, the resolution is limited to ~ 0.1 nm, due to the aberrations in the objective lens system in electron microscopes. It is still orders of magnitude smaller than the wavelength of visible light. This small wavelength helps to probe a spatial resolution down to atomic dimensions in materials.

TEM image contrast arises because of the scattering of the incident electron beam by the specimen. The electron wave can change both its amplitude and its phase as it traverses the specimen and both types of change can give rise to image contrast. The distinction between the amplitude contrast and the phase contrast is a fundamental distinction. In most situations, both types of contrast actually contribute to an image, and one will tend to dominate the other. Amplitude contrast results from variations in mass or thickness or a combination of the two. *Z*-contrast is the name given to mass-thickness at high-resolution, at atomic levels. Phase contrast arises whenever there are more than one beam contributing to the imaging. Phase-contrast imaging is often thought to be synonymous with high-resolution

TEM. In fact, phase contrast appears in most TEM images even at relatively low magnifications.

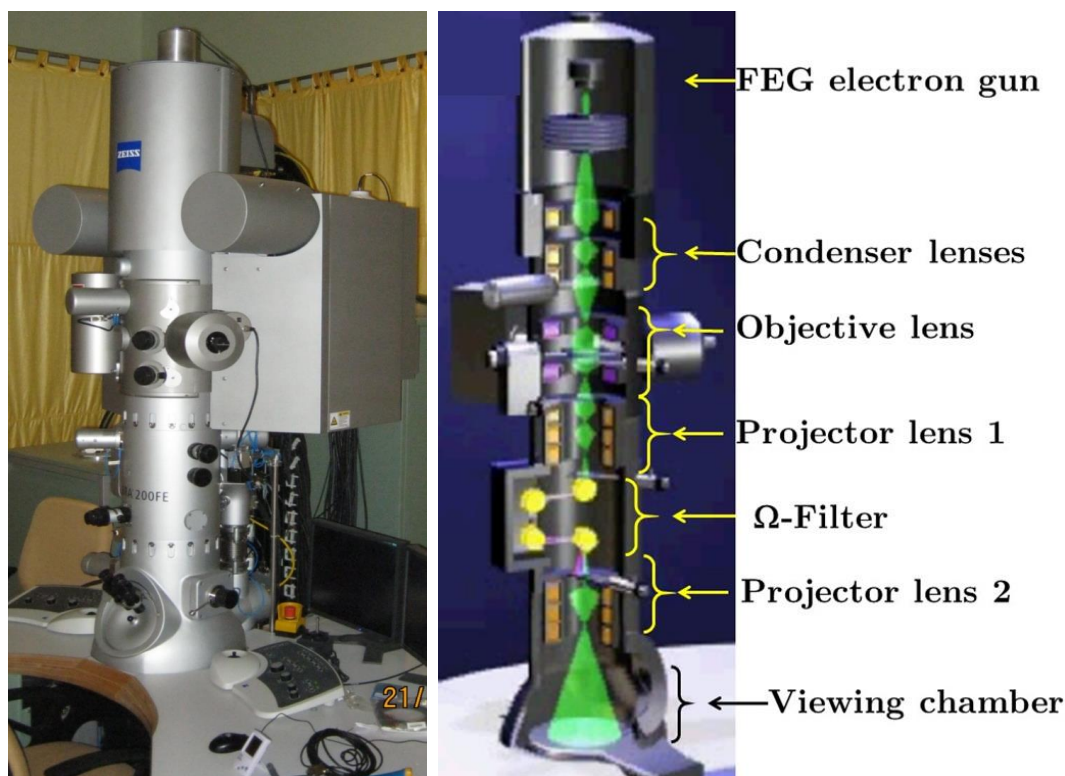


Figure 2.9 The LIBRA 200FE, high resolution transmission electron microscope: the photograph (Left) and the illustration of the electron path in the TEM (right).

The TEM used for characterizing all the materials in this thesis is LIBRA-200 FE. It is a high resolution TEM (HRTEM), equipped with field emission gun (FEG) electron source and an in column omega filter. The HRTEM may also be operated in scanning mode, rendering it a Scanning TEM (STEM). In addition to imaging, STEM mode can also be used for Spot EELS and Spot EDS. Moreover, the microscope comprises of the components required for the analytical techniques: Energy Dispersive X-ray Spectrometry (EDS) and Electron Energy Loss Spectroscopy (EELS). The TEM is operated at an accelerating voltage of 200 kV. The information limit of the TEM is 1.3 Å and STEM resolution 3 Å. The energy resolution of the EELS spectrometer is 0.7 eV.

2.4.1. Energy Dispersive X-ray Spectrometry

Energy Dispersive X-Ray Spectroscopy (EDS or EDX) is a chemical microanalysis technique used in conjunction with TEM. It is an analytical technique used for elemental analysis or chemical characterization of a sample, using the characteristic X-rays emitted by the atomic species. High energy electron beam is used to stimulate the characteristic X-rays from the elements present in the sample. X-ray detector present in the EDS set up detects the X-ray and generates the spectrum.

2.4.2. TEM Sample preparation

While using TEM for materials characterization, the real challenge lies in the preparation of thin samples for the TEM, because the sample should be ultimately 'electron transparent'. Typically, the region of interest in the sample is expected to be thin around 100 nm. Different methods exist for sample preparation, for different types of materials (metals/glass/ceramics) and different sample geometries (bulk/thin films/powders). But generally the thinning processes do affect the sample microstructures and morphology, changing both their structure and chemistry. So, in the present thesis, sample preparation method was selected based on the situation and requirements.

2.5. Spectroscopy techniques

2.5.1. Core level spectroscopy techniques

The properties of solids are determined by the characteristic features of valence electron states. The valence electron states contain the partially filled conduction band states in metals and the filled valence and empty conduction band states in insulators.

The underlying physical phenomenon in these spectroscopic techniques is excitation of a core electron to the excitation threshold (valence or conduction band), by X-rays or electron beam (which is called the probe) and the excited state

of the system decays by emitting X-rays or Auger electron. Accordingly, there are various kinds of core level spectroscopy. Among them, X-ray absorption spectroscopy (XAS) uses X-ray for exciting the core electron, whereas, the electron energy loss spectroscopy (EELS) uses electron for the purpose. When a core electron is ejected from an atom the probe loses equivalent energy. Each core shell has a distinct binding energy, and thus if one plots the energy loss of the probe as a function of energy, there is an abrupt increase in absorption cross-section corresponding to the ionization energy. This gives rise to a so-called absorption edge, with each edge representing a different core-electron binding energy. The edges are named according to the principle quantum number of the electron that is excited, as K, L, M, etc.

The X-ray absorption spectrum is closely related to the density of states of a system. As such XAS is able to provide a detailed picture of the local electronic structure of the element studied. Core level spectroscopy is majorly used for elemental identification. Most of the times, the ionization edges in the core level spectra are used as fingerprints (and compared with earlier reports) to identify the phase, the nature of bonds, coordination numbers, etc. But, inherently, the core level spectroscopy is a powerful tool which can be used to study many material properties like chemical shift (change in charge state), coordination numbers, radial distribution function, structural information, band gap, bulk/surface plasmons, 2D elemental distribution maps (e.g. EFTEM imaging in TEM), sample thickness, etc.

2.5.1.1. X-Ray Absorption Spectroscopy

Until synchrotrons were utilized as the main photon sources, the study of core level spectroscopy was a long way behind. The high-brilliance synchrotron radiation sources have opened up this possibilities for X-Ray Absorption Spectroscopy (XAS), where high energy X-ray photons are used for exciting the core electrons. In the present thesis, XAS studies were done in the INDUS-2 synchrotron facility in RRCAT, Indore.

The beamline BL-01[140] was used to analyse X-ray absorption near edge structure (XANES) and the measurements were taken in total electron yield (TEY) mode. The specimen were probed upto a depth of ~ 70 nm, where the effects of irradiation will be prominent.

The effects of ion irradiation in the iron phosphate glass samples were studied by analyzing the changes in the XANES around the ionization edge of Fe (Fe L_{23} -edge, 708 eV). Similarly the irradiation induced changes in the nature of bonds in thoria was studied by analyzing the changes in the Oxygen K edge features (at 532 eV). Soft X-ray absorption spectroscopy (SXAS) beamline (BL-01) was used for characterizing the samples mentioned above, since the energy range accessible in BL-01 (100 eV to 1000 eV) matches with the requirements.

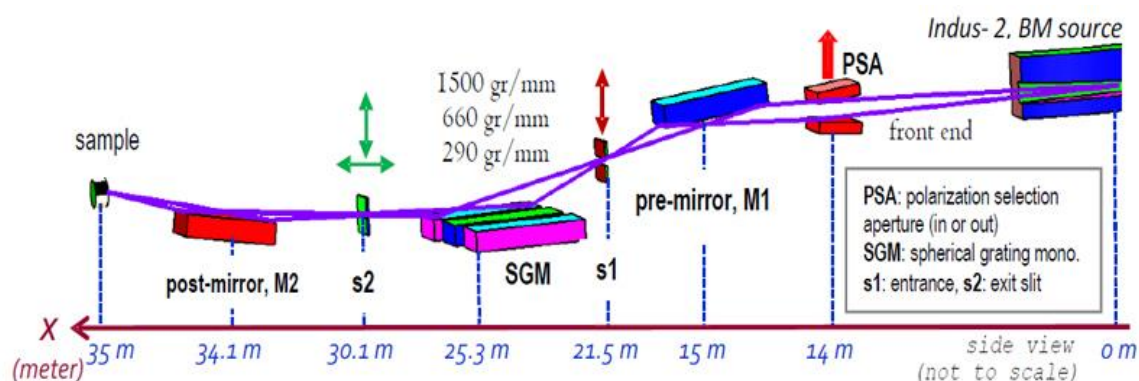


Figure 2.10 Schematic diagram of polarized light soft X-ray absorption spectroscopy beamline BL01 at INDUS-2

2.5.1.2. Electron energy loss spectroscopy

Electron energy loss spectroscopy (EELS) is also a core level spectroscopic technique that uses high energy electrons as the after they interact with a specimen. It is a powerful analytical technique which is capable of providing information about electronic structure, bond length, oxidation state, and chemical composition, with a spatial resolution down to atomic level in favourable cases[141].

The LIBRA 200FE TEM has the omega energy filter which helps analyse the inelastically scattered electrons. The schematic of the TEM with Ω energy filter is

shown in Figure 2.11. The CCD camera, which is primarily used for imaging, is also calibrated for recording the EELS spectra.

A typical EELS spectrum is shown in Figure 2.11(b). In EELS the intensity of the inelastically scattered electrons, is plotted as a function of the energy loss. The spectra consists of zero loss peak (ZLP) at 0 eV and a plasmon peak at ~ 50 eV, followed by ionization edges beyond 50 eV upto 2000 eV. The ZLP corresponds to the electrons which do not lose energy inside the specimen. Since majority of the electrons are scattered elastically, the intensity of ZLP will be orders of magnitude larger than the other peaks. The ZLP and the plasmon peaks have very few applications while the ionization edges are used rigorously for elemental identification, for analyzing the charge state, to recognize the type of bonds, etc.

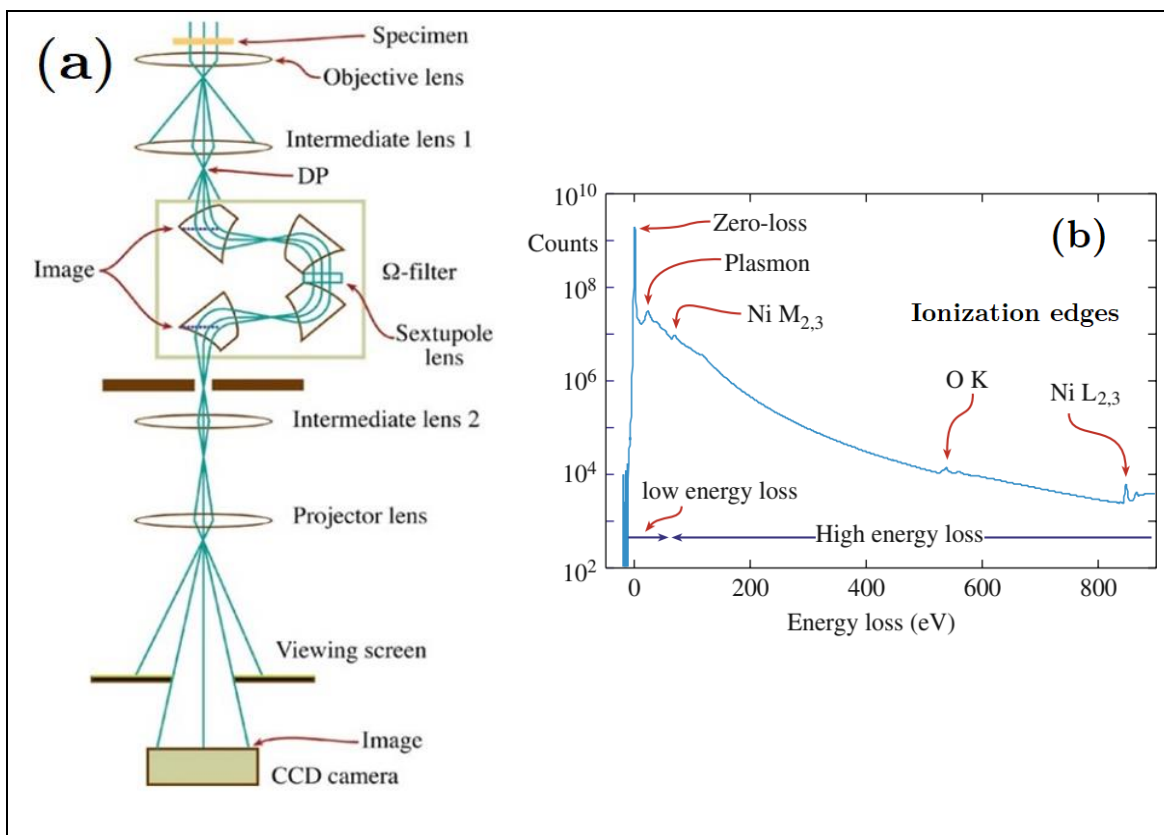


Figure 2.11 (a) Schematic diagram of Omega energy filter in TEM for EELS analysis. (b) Typical EELS spectrum containing the zero loss peak, the plasmon peaks and the ionization edges (Ref.[142])

2.5.2. Raman spectroscopy

Raman spectroscopy is one of the vibrational spectroscopic techniques used to provide information on molecular vibrations and crystal structures. It is used for phase identification, chemical identification, characterization of molecular structure, changes in bonding effects, changes in atomic environment and stress in the material.

Raman spectroscopic technique uses a laser light source to irradiate the material sample. When light is scattered by matter, almost all of the light gets scattered elastically without any change in energy and this process is called Rayleigh scattering. At the same time, a very small fraction of light undergoes inelastic scattering, where it loses energy in modifying the vibrational level of the molecule.

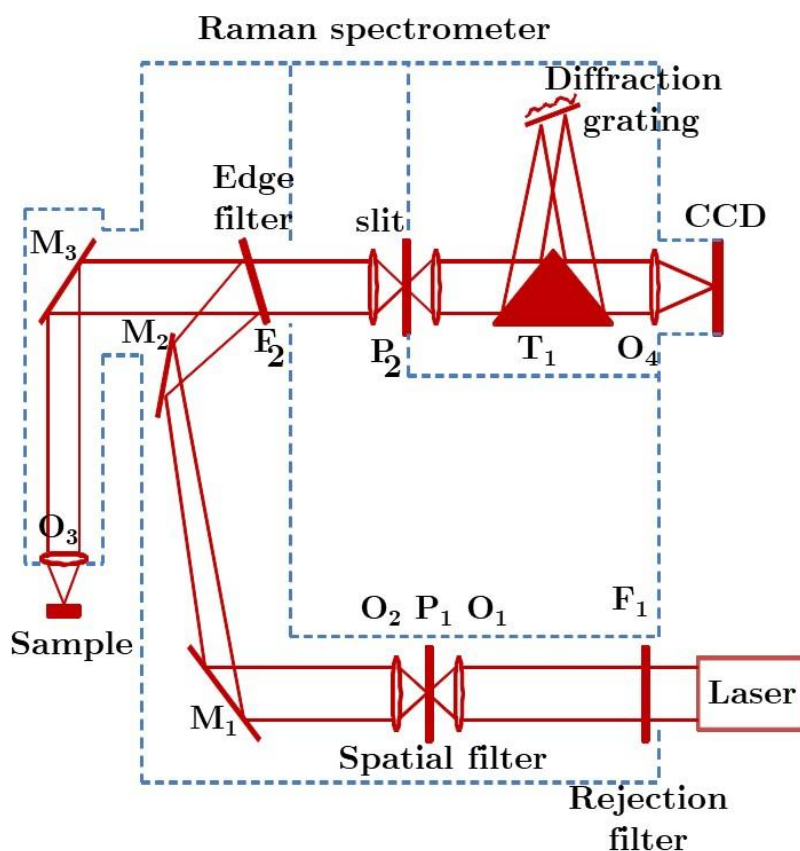


Figure 2.12 Block diagram representing the working of Raman spectrometer

In the present thesis, the equipment used for Raman analysis is the “Micro Raman” spectrometer system; make: Renishaw and model: InVia. The excitation laser had a frequency of 514 nm. It comprises of one or more lasers as excitation

source, a microscope unit coupled to a monochromator and a CCD camera detector. The working of this spectrometer is briefly shown in Figure 2.12 with the help of block diagram.

Raman scattering setup consists of a laser excitation source, focusing lens, sample chamber, collection optics, dispersing system to analyze the scattered beam and a detector. This spectrometer, the 514.5 nm line from an Ar^+ laser has been used as excitation source.

The laser light entering the system unit passes through a rejection filter F_1 , whose purpose is to reject all but the desired lasing line from the laser for excitation of the sample. Then a plasma filter for eliminating the plasma lines corresponding to the desired wavelength is used. The laser beam passes through a spatial filter which comprises of a set of objective O_1 and pinhole P_1 to converge the beam to a 10 μm (Gaussian shaped) spot. A second objective lens O_2 is used to make a well-collimated parallel beam. Two mirrors M_1 and M_2 are used to reflect the laser beam on to the edge filter F_2 . The angle of the edge filter is adjusted in such a way that the laser beam falls on mirror M_3 and is directed into the optical path of the microscope. The light falls on the microscope objective lens O_3 which focuses it on the sample to illuminate it. The sample is placed on a piezoelectric transducer-controlled mechanical stage which helps in positioning and focusing the beam on the sample. The light scattered from the sample is collected back in the back-scattering geometry by the same microscope unit which incidents it on the edge filter F_2 . This filter blocks the Rayleigh component of the scattered light and passes the Raman signal into the monochromator unit through slit P_2 . Inside the monochromator unit, the scattered light strikes the prism mirror T_1 which directs it to the grating. The grating disperses the light and sends it back to T_1 which directs it to the detector through lens O_4 . The lower wavenumber limit of detecting Raman signal using this spectrometer is 65 cm^{-1} . Below this range, the edge filter eliminates Raman intensities also along with Rayleigh background. The detector is

a Peltier-cooled (upto 197 K) CCD camera where the dispersed light is focused. The CCD converts light into charges which is read by the readout electronics.

2.6. Computational methods

2.6.1. Density Functional Theory

The material world of everyday experience, as studied by chemistry and condensed matter physics is built up from electrons and a few (or at most a few hundred) kinds of nuclei. The basic interaction is electrostatic or Coulombic[143]. The electrons must be described by quantum mechanics, while the more massive nuclei can sometimes be regarded as classical particles.

The ground state properties of any solid can thus be obtained *ab-initio* by solving time independent Schrödinger equations.

$$H\psi \{R_A\}, \{r_i, \sigma_i\} = E\psi \{R_A\}, \{r_i, \sigma_i\}$$

Eqn. 2.6

The many-body wavefunction ψ is a complicated function of all the spatial coordinates of nuclei $\{R_A\}$ and spatial and spin coordinates of electrons $\{r_i, \sigma_i\}$. H includes all possible interactions between electrons and nuclei and can be written as

$$H = \underbrace{\sum \frac{-\hbar^2}{2M_I} \nabla_I^2}_{\text{K.E term}} + \underbrace{\sum \frac{-\hbar^2}{2m_i} \nabla_i^2}_{\text{e-e repulsion}} + \underbrace{\frac{e^2}{2} \sum \sum \frac{1}{r_i - r_j}}_{\text{nuclei-nuclei repulsion}} + \underbrace{\frac{e^2}{2} \sum \sum \frac{Z_I Z_J}{|R_I - R_J|}}_{\text{e-nuclei interaction}} - \underbrace{e^2 \sum \sum \frac{Z_I}{R_I - r_j}}_{\text{e-nuclei interaction}}$$

Eqn. 2.7

M_A is the ratio of the mass of nucleus A to the mass of an electron and Z_A is atomic number of nucleus A.

Eqn. 2.7 is a complex one to solve for systems containing more than a few electrons. So few approximations are made to reduce the complexity.

Born-Oppenheimer approximation: Since nuclei are much heavier than electrons, the timescale its response is also orders of magnitude slower than electrons. As a result the second term in *Eqn. 2.7* can be neglected and the fourth term can be assumed as constant for a given configuration of the nuclei (considered as external potential, V_{ext}). Even with this simplification, it becomes very tough

task to solve N -electron system (with $3N$ coordinates). Hartree assumed the wave function of electron to be product of single particle states, *i.e.*, the electrons are considered to be independent. (Hartree method includes only Coulomb repulsion between electrons.)

$$\psi_e x_1, x_2, \dots, x_N = \phi_1 x_1 \phi_2 x_2 \dots \phi_N x_N$$

Eqn. 2.8

Electrons being Fermionic in nature, their wavefunction should be antisymmetric with respect to the exchange of any two electrons. But the product of one-electron wavefunctions as given in equation 2.8 is not antisymmetric. Hartree-Fock approximation simplifies the interacting many electron wave function into a product of wave functions of single electrons. Anti-symmetry was included in Hartree-Fock method, by writing many-electron wave function as a Slater determinant of one-electron orbitals as

$$\psi_{\text{HF}} \mathbf{r} = \frac{1}{\sqrt{n!}} \begin{vmatrix} \psi_1 \mathbf{r}_1 & \dots & \psi_n \mathbf{r}_1 \\ \vdots & \ddots & \vdots \\ \psi_1 \mathbf{r}_n & \dots & \psi_n \mathbf{r}_n \end{vmatrix}$$

Eqn. 2.9

Wave function based approaches become very difficult to solve when the particle number becomes very large. Wave function for a system depends on the position coordinates of all the electrons. Alternative approach using electron density simplifies the problem as it depends on only three position coordinates from which one would find the electron density – the total electron density due to all the electrons in the system – at that position. DFT is based on the two theorems as follows. For any system of interacting particles in an external potential $V_{\text{ext}}(\mathbf{r})$, the potential $V_{\text{ext}}(\mathbf{r})$ is determined uniquely, except for a constant, by the ground-state particle density $n_0(\mathbf{r})$. Second theorem states that a universal functional of the energy $E[n]$ in terms of the density $n(\mathbf{r})$ can be defined, valid for any external potential $V_{\text{ext}}(\mathbf{r})$. For any particular $V_{\text{ext}}(\mathbf{r})$, the exact ground-state energy of the system is the global minimum value of this functional, and the density $n(\mathbf{r})$ that minimizes the functional is the exact ground-state density $n_0(\mathbf{r})$.

The practical tools to determine ground state density is given by the Kohn-Sham ansatz. They replace the interacting many body problem by auxiliary problem of non-interacting electrons having same density as that of original interacting system. This leads to Kohn-Sham equations:

$$\left(-\frac{1}{2}\nabla^2 + V_{eff}(\mathbf{r}) \right) \psi_i(\mathbf{r}) = \varepsilon_i \psi_i(\mathbf{r})$$

Eqn. 2.10

where $n(\mathbf{r}) = \sum |\psi_i(\mathbf{r})|^2$ and

$$V_{eff}(\mathbf{r}) = V_{ext}(\mathbf{r}) + \int \frac{n(\mathbf{r}')}{|\mathbf{r} - \mathbf{r}'|} d\mathbf{r}' + V_{xc}(\mathbf{r})$$

Eqn. 2.11

These equations are solved self consistently to solve the Kohn-Sham equations, beginning with a guess electron density $n(\mathbf{r})$. Here the effective potential $V_{eff}(\mathbf{r})$, experienced by every electron includes the external potential ($V_{ext}(\mathbf{r})$) and the exchange-correlation potential $V_{xc}(\mathbf{r})$ and the wave function of an electron under this potential is calculated as a linear combination of plane wave basis sets.

This exchange-correlation function contains all the many body (many electrons) effects and is crucial approximation involved in DFT calculations. Two most widely used approximations being Local Density Approximation (LDA) and Generalized Gradient Approximation (GGA). In LDA the exchange-correlation energy at each point of the real space is assumed to be equal to that of a uniform electron gas with same density. In the context of gradient corrected exchange correlation functionals, two widely used functionals are those parametrized by Perdew and Wang (PW91)[144], and Perdew, Burke and Ernzerhof (PBE)[145].

2.6.1.1. Materials Studio - CASTEP

CASTEP[146] is a quantum mechanics-based program designed specifically for solid-state materials science. CASTEP employs the density functional theory plane-wave pseudopotential method, which allows to perform first-principles

quantum mechanics calculations to explore the properties of crystals and surfaces in materials. CASTEP is included in Materials Studio package.

Being a DFT code, CASTEP helps to calculate the core level spectroscopies, density of states, electron density difference, and a wide range of properties related to vibrational models which depends on electronic structures. The graphical user interface in Materials Studio helps to prepare the input (like definition of the crystal structures) and to process the outputs (like extracting charge density plots, EELS spectra plots, etc.) from CASTEP. The complete guide is available in Ref.[147].

Core level spectroscopic properties of solids are related to the electronic transitions from a core level of an ion to the conduction band. The core level is localized, so the core level spectroscopy provides a detailed element-specific picture of the local electronic structure around a given atomic site. Electron energy-loss near-edge structure (ELNES or EELS) and X-ray absorption near-edge structure (XANES) spectroscopy provide information on the unoccupied electronic states (in the conduction bands) by exciting one electron from a core level into the unoccupied state. In this case, the probing electron or X-ray interacts with a system that has been perturbed by the probe itself, created a hole in the inner-shell, a ‘core hole’. Calculations with core holes are designed in CASTEP to describe the electronic structure of such perturbed systems.

In the present thesis CASTEP is used to calculate EELS, and electron charge density difference.

2.6.1.2. Vienna *Ab-initio* Simulation Package

The Vienna *Ab-initio* Simulation Package (VASP) is a computer program for atomic scale materials modelling; for electronic structure calculations and quantum-mechanical molecular dynamics, etc. from first principles. VASP computes an approximate solution to the many-body Schrödinger equation within density functional theory (DFT). In VASP, the central quantities like the one-electron orbitals, the electronic charge density, and the local potential are expressed in plane

wave basis sets. The interactions between the electrons and the systems of ‘ions + core electrons’, are described using norm-conserving or ultrasoft pseudopotentials, or the projector augmented wave (PAW) method.

In the present thesis VASP has been used to find out the total energies of crystal systems as a function of different volumes. These values help calculate the lattice parameter of the particular crystal system, using the Birch–Murnaghan isothermal equation of state[148]. VASP calculations are used in the thesis, to find the binding energy of two or more interstitial atoms in different neighbourhoods, and also to find the formation energy pertaining to the formation of defects and/or interstitials in a perfect crystal system. The details are given in the appropriate sections in the thesis.

2.6.2. Molecular Dynamics simulations

LAMMPS (Large-scale Atomic/Molecular Massively Parallel Simulator) is a classical molecular dynamics simulation code with a focus on materials modeling. LAMMPS can model systems with only a few particles up to millions or billions. In the most general sense, LAMMPS integrates Newton’s equations of motion for a collection of interacting particles. A single particle can be an atom or molecule or electron, a coarse-grained cluster of atoms, or a mesoscopic or macroscopic clump of material. The interaction models that LAMMPS includes are mostly short-range in nature; some long-range models are included as well. LAMMPS uses neighbor lists to keep track of nearby particles. The lists are optimized for systems with particles that are repulsive at short distances, so that the local density of particles never becomes too large.

In the present thesis, LAMMPS is used to calculate the stacking fault formation energy in the *fcc* yttrium titanate $Y_2Ti_2O_7$.

2.6.3. CTM4XAS

A range of DFT based computer codes exist to calculate the X-ray absorption cross-section and thereby to calculate the XAS which is a core level spectrum. The theory of DFT transforms the problem of many electron system (*i.e.*, the system of valence electrons) into a scenario where every single electron is considered to be moving in the effective field of all the other valence electrons; the field being represented by the density functional $n_0 \mathbf{r}$. This single particle description works well for all K edges, whereas for the other edges, in particular the metal L₂₃ edges, the agreement is poor. The reason for this discrepancy is not that the density-of-states is calculated wrongly, but that one does not observe the density of states in such X-ray absorption processes. The reason for the deviation from the density-of-states is the strong overlap of the core wave function with the valence wave functions. The overlap of core and valence wave functions is present also in the ground state, but because all core states are filled, it is not effective and one can approximate the core electrons with their charge.

Multiplet effects are important in the cases when there are core holes. Multiplet effects determine the spectral shapes and influence the L₃ to L₂ branching ratio. They play an important role in a large fraction of X-ray spectroscopies. An exhaustive review of the multiplet effects may be seen in Ref[149].

CTM4XAS stands for Charge Transfer Multiplet program for X-ray Absorption Spectroscopy. In contrast to these *ab-initio* routes, the CTM4XAS program is based on a semi-empirical approach that includes explicitly the important interactions for the calculation of L edge spectra. This includes the core and valence spin-orbit couplings, the core-valence two-electron integrals (multiplet effects) and the core hole induced charge transfer effects. CTM4XAS calculations use the charge transfer multiplet model developed by Theo Thole[150] as the basis.

2.7. Summary

This chapter gives brief introduction to diffraction techniques (XRD, GIXRD and electron diffraction), spectroscopic techniques (EDS, EELS, Raman spectroscopy, XAS) and High resolution TEM. This chapter briefly explains the various computational methods used in the thesis.

Chapter 3

Aggregation and ordering of helium in thoria

3.1. Introduction

The presence of inert gas bubbles degrades the thermal conductivity of any fuel material and also leads to swelling[5,6]. Thoria (ThO_2) is a candidate fuel material for future reactors. In the present chapter, the behaviour of helium in the thoria lattice is studied using experiments and DFT calculations.

The behaviour of inert gases (Kr, Xe and He) inside the nuclear fuel materials (urania, thoria, and ceria) have been characterized by many authors[86–91,93,94] based on experiments and computer simulations. Mohun *et al.*[94] studied the mechanism of defect formation due to α particle irradiation in urania and thoria by irradiating with 21 MeV He^{2+} ions, where Raman scattering and luminescence results showed that although UO_2 , ThO_2 and PuO_2 share similar characteristics, the mechanism of defect creation in ThO_2 was totally different. Roudil *et al.*[90] measured the activation energy (E_a) and the diffusion coefficient (D) for the diffusion of helium in urania by nuclear reaction analysis ((d,p) reaction) and found that E_a was ~ 2 eV and D was very small $2.9 \times 10^{-17} \text{ m}^2\text{s}^{-1}$, at 1000 °C.

The calculations by Dąbrowski *et al.*[87] supports the experimental observation[86] that helium occupies octahedral interstitial position in the perfect *fcc* lattice of urania and thoria. Further, Dąbrowski *et al.*[87] showed that helium atom located in the octahedral interstitial site would cause a local increase in the lattice parameters of both urania and thoria. Based on DFT calculations, Yun *et al.*[88] have showed that helium atoms might tend to form even small clusters around the octahedral interstitial site in urania and Shao *et al.*[89] have predicted similar clustering in thoria. Using density functional theory (DFT) calculations, Lu *et al.*[91] have shown that helium diffusion is possible in thoria lattice only in the presence of Th-vacancy and this might lead to helium aggregation causing failure

of fuel. However, there is no experimental report on the behaviour of helium atoms in the lattice of thoria.

In this context, it would be interesting to study the behaviour of low concentration of helium in defective thoria. In the present work, thoria was irradiated with low energy (100 keV) He^+ ions which introduces a peak helium concentration of $\sim 4 \text{ at}\%$ along with production of Th- and O-vacancies due to displacement damage. The trapping, diffusion and ordering of helium in thoria matrix were studied using Transmission Electron Microscopy (TEM) and Grazing Incidence X-Ray Diffraction (GIXRD), and DFT based calculations were used to interpret and support the experimental findings.

3.2. Experimental and computation methods

3.2.1. Sample synthesis

Thorium nitrate (from M/s. Indian Rare Earths, India) and analytical reagent grade citric acid were used as precursors for the synthesis of thoria. The sample was synthesized by heating an aqueous solution containing thorium nitrate and citric acid on a hot plate. The combustion process involves dehydration followed by de-nitration of thorium nitrate and destruction of citric acid. The final product was a porous, fluffy, crystalline and highly free flowing powder. The resultant powder was calcined at 973 K for 5 hours in air. The synthesis procedure is explained in Ref[137]. The calcined powder was compacted with a pressure of 300 MPa by employing a double action hydraulic press and made into pellets. The pellets were sintered at 1773 K. The pellets have a density of 9.5 g/cm^3 which is 95% of the theoretical density.

3.2.2. Experimental methods

Thoria pellets were irradiated with 100 keV He^+ ions to study the behaviour of implanted helium atoms. In order to study the role of irradiation induced defects

and defects clusters, thoria pellets were irradiated also with 4 MeV Si⁺ ions. Low energy helium ion implantations were carried out using 150 kV ion accelerator.

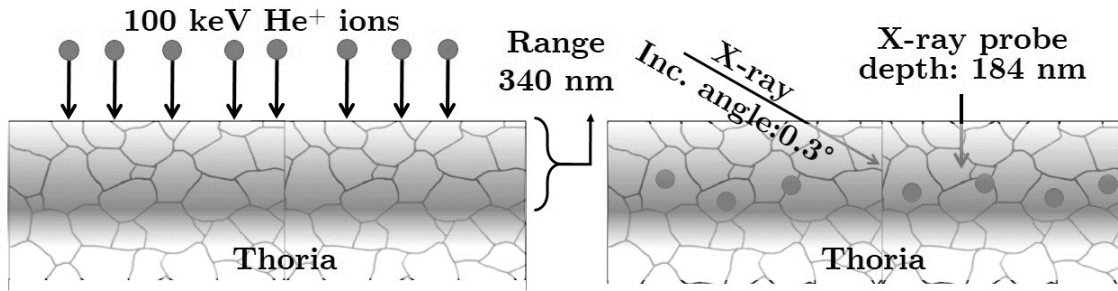


Figure 3.1 Schematic illustration of the implantation of helium ions and the probe depth of GIXRD.

The irradiations were carried out upto ion fluences 5×10^{16} ions/cm² and 1×10^{17} ions/cm². The base vacuum in the irradiation chamber was maintained at 5×10^{-7} mbar. The 4 MeV Si⁺ ion irradiation was carried out in the 1.7 MV Tandatron Accelerator. For the ion irradiation experiments, the beam current density was maintained $\sim 1 \mu\text{A}/\text{cm}^2$ on the sample, to avoid beam heating. Table 3.1 gives the details of the ion irradiation experiments, calculated using SRIM. Displacement energies for Th and O atoms, required for the SRIM calculations, were taken as 53.5 eV and 20 eV respectively as suggested by Xiao *et al.*[151].

Table 3.1 Details of ion irradiations: 100 keV He⁺ and 4 MeV Si⁺ ions on thoria.

Ion	Projected range (nm)	S _e (eV/nm)	S _n (eV/nm)	Ion fluence (ions/cm ²)	Damage at 340nm (dpa)	Concentration of Helium
100 keV He ⁺	340 (±123)	263.4	4.08	5×10^{16}	1.85	2.2 at%
				1×10^{17}	3.85	4.4 at%
4 MeV Si ⁺	1540 (±320)	3762.0	55.90	2×10^{16}	3.69	–

SRIM calculations showed that the peak of the projected range of 100 keV He⁺ ions in thoria was at a depth of 340 nm from the surface (with a straggling of 123 nm). The average kinetic energy transferred by 100 keV He⁺ ion to Th and O atoms were found to be 103 eV and 65.9 eV respectively. The average kinetic energy transferred by 4 MeV Si⁺ ion to Th and O atoms were found to be 549 eV and 242 eV respectively.

Grazing Incidence X-Ray Diffraction (GIXRD) technique was used to characterize the effects of implanted helium in the near surface of thoria samples. Bruker X-ray diffractometer (Model: D8-Discover) with Cu K_α radiation (1.541 Å) was used for the characterization. The incident angle was kept at 0.3° and the diffracted X-rays were collected from 25° to 95° , with a step size of 0.05° . The depth probed by X-rays at 0.3° in thoria is 184 nm, whereas the projected range of 100 keV He^+ ions in thoria is 340 nm. Therefore, GIXRD probes the region where helium ions are implanted along with production of defects. In the case of silicon ion irradiated sample, (the range of 4 MeV Si^+ ion is 1540 nm) the GIXRD (with the same incident angle of 0.3°) probes the same depth (184 nm) where only the damage caused by silicon ions will be present and not the implanted silicon atom.

The microstructure of all the irradiated samples were studied using LIBRA 200FE (High Resolution Transmission Electron Microscope (HRTEM)). TEM specimens were prepared by scratching the surface of the pellets using a scalpel blade and by dispersing it in the carbon coated copper grid with the help of propanol. This sample preparation method was preferred over conventional methods like focused ion beam method or ion-milling method since they introduce irradiation induced artefacts in the sample.

3.2.3. Computation details

Density functional theory (DFT) based calculations were used to find the formation energies and the binding energies of different defects in thoria and also to find the lattice parameters of different configurations. All the calculations were performed using *ab-initio* DFT methods as implemented in the plane wave based Vienna *Ab-initio* Simulation Package (VASP). The interaction between the valence electrons and the ionic core is described by projector-augmented-wave (PAW) pseudo-potentials[152]. Generalized Gradient Approximation (GGA) as parametrized by Perdew, Burke, and Ernzerhof (PBE)[145] was used as the exchange-correlation functional. GGA exchange-correlation functional reproduces

the ground-state properties of ThO₂ reasonably accurately[153]. A kinetic energy cut-off of 550 eV was found to give total energy convergence of the order of 0.001 eV/atom in the case of unit cell of ThO₂. Integration over the Brillouin zone was done using a Monkhorst-pack[154] grid of 5×5×5 k -points for the unit cell calculations and 3×3×3 k -points for a super cell containing 2×2×2 unit cells of ThO₂. Both the cell volume and ion positions were relaxed until the force on each ion was less than 0.001 eV/Å. The structural details of thoria, required for DFT calculations, were identified from the International Centre for Diffraction Data (ICDD) based on the XRD patterns. The space group was identified as 225 ($Fm\bar{3}m$). The fcc unit cell contains 4 Th atoms (Wyckoff position:(0,0,0), symmetry:4a) and 8 O atoms (Wyckoff position: ($\frac{1}{4},\frac{1}{4},\frac{1}{4}$), symmetry:8c).

The formation energies E_{form} , the energy for the formation of helium atom inside the reference system, were calculated using the expression[91],

$$E_{form} = E_{tot} - E_{ref} + E_{He}$$

Eqn. 3.1

where, E_{tot} is the total energy of the system – *i.e.*, the reference system with helium atom(s), E_{ref} is the energy of the reference system (like the perfect thoria system or the defective system with Th- or O-vacancy) and E_{He} is the energy of an isolated helium atom, calculated using DFT. A 96 atom super cell containing 2×2×2 unit cells of ThO₂ was used for the calculation of formation energy.

The possibility of ordering of helium atoms in thoria lattice was analysed by calculating the binding energy per helium atom in different configuration and different concentration of helium atoms in thoria lattice. It was calculated as

$$E_{BE}^{conf} = \frac{E_f^{conf} nHe - nE_f 1He}{n}$$

Eqn. 3.2

where, E_f^{conf} is the formation energy of n He atoms in the respective configuration and $E_f 1He$ is the formation energy of single He atom in ThO₂. A super cell containing 2×2×2 unit cells of ThO₂ was used in these calculations also.

3.3. Results

3.3.1. XRD analysis

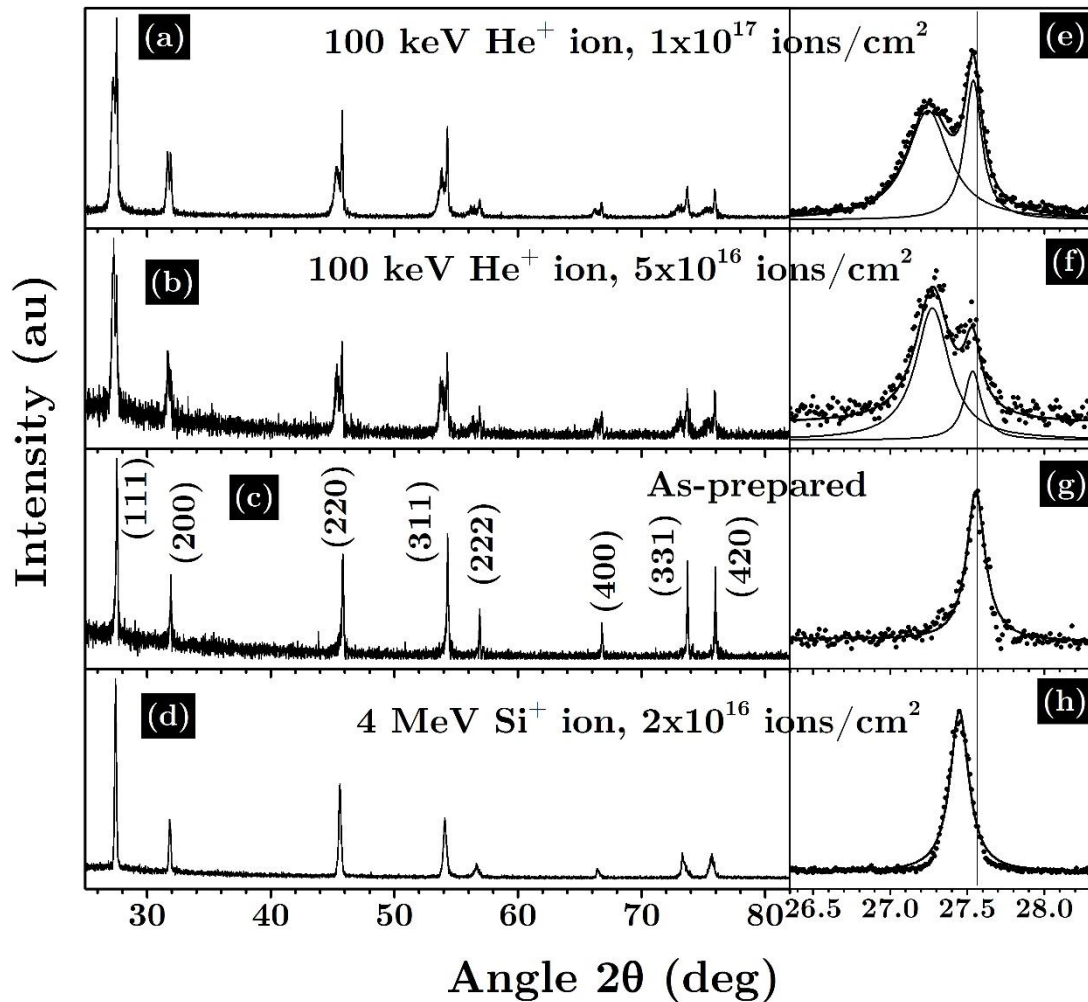


Figure 3.2 The GIXRD patterns of 100 keV He^+ ion irradiated thoria samples for the ion fluences of (a) 1×10^{17} ions/cm² and (b) 5×10^{16} ions/cm² along with (c) the as-prepared sample and (d) the thoria sample irradiated with 4 MeV Si^+ ion up to 2×10^{16} ions/cm². The plots (e), (f), (g) and (h) show the magnified view of the (111) peak in the patterns (a), (b), (c) and (d) respectively.

The GIXRD patterns of the as-prepared sample and the 100 keV He^+ ion and 4 MeV Si^+ ion irradiated samples, are shown in Figure 3.2. The structure of the as-prepared sample was identified from the GIXRD pattern of the sample, shown in Figure 3.2(c). The prominent peaks of the face centered cubic (*fcc*) system of thoria, corresponding to the planes such as (111), (200), (220), (311), etc. – as reported in PDF No.00-042-1462 in the ICDD database – were noticed in the XRD

pattern of the as-prepared sample. The space group is identified as $Fm\bar{3}m(225)$ and the lattice parameter is 5.60 Å.

Figure 3.2(a) and (b) shows the GIXRD patterns of the He^+ ion irradiated samples, upto the ion fluences of 5×10^{16} ions/cm² and 1×10^{17} ions/cm² respectively. These GIXRD patterns showed all the standard peaks of thoria, but the peaks were shifted slightly towards lower angles ($\sim 0.05^\circ$) when compared to the as-prepared sample. The slight shift may be noticed clearly in the magnified view of (111) peaks, shown in Figure 3.2(e), (f) and (g). Interestingly, a set of additional peaks were also observed in the He^+ ion irradiated samples (Figure 3.2(a) and (b)) near all the standard diffraction peaks of thoria and the additional peaks were shifted to lower 2θ values. This confirmed that the additional peaks correspond to a region in the sample where the unit cell has expanded. From the intensities of the additional peaks, it was observed that the volume fraction of expanded lattice could be small. From the peak positions, the lattice parameter of the expanded unit cell was calculated.

The standard peak (111) in the as-prepared thoria (Figure 3.2(g)) was seen at the Bragg angle 27.55° . The additional peak near (111) (Figure 3.2(e)), which appeared after irradiation upto the ion fluence of 1×10^{17} ions/cm², was seen at 27.25° . The d -spacings corresponding to these peaks were found to be 3.236 Å and 3.270 Å respectively. Therefore, the expansion (Δd) in (111) planes, after irradiation upto the ion fluence of 1×10^{17} ions/cm², was 0.034 Å, and the corresponding change in the lattice constant ($\Delta a/a_0$) was 1.07%. Similarly, in the sample irradiated upto the ion fluence of 5×10^{16} ions/cm² (Figure 3.2(f)), the lattice expansion in (111) planes was found to be 0.97%.

Figure 3.2(d) shows the XRD pattern of the thoria sample irradiated with 4 MeV Si^+ ions. There was no additional set of peaks in the case of Si^+ ion irradiated sample. However, the standard peaks of thoria have shifted towards lower 2θ value by 0.1° after Si^+ ion irradiation. The corresponding lattice expansion was found to

be 0.06% and it was comparable to the lattice expansion of 0.05% reported by Tracy *et al.*[155,156].

3.3.2. TEM analysis

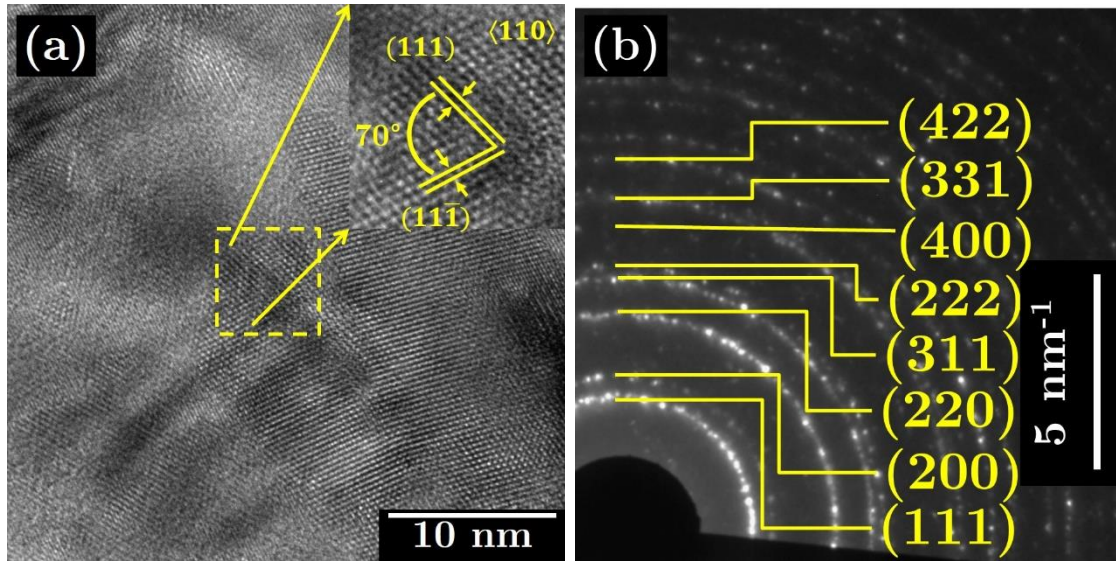


Figure 3.3 (a) The high resolution TEM image of the as-prepared thoria; the lattice fringes were indexed to (111) planes (d -spacing: 3.23 Å) and the zone axis was $\langle 110 \rangle$ (b) The electron diffraction pattern of thoria.

Figure 3.3(a) shows the high resolution TEM image of the as-prepared thoria sample. The lattice fringes in the high resolution TEM images were indexed to (111) planes of thoria, with d -spacing of 3.23 Å. The zone axis was found to be $\langle 110 \rangle$. Figure 3.3(b) shows the electron diffraction pattern recorded from the as-prepared thoria; it was indexed to *fcc* thoria system (PDF No.00-042-1462).

Figure 3.4(a) shows the bright field TEM image of the He⁺ ion irradiated thoria sample. The circles in Figure 3.4(a) show some regions in the matrix with dark contrast, which were not seen in the as-prepared sample. Figure 3.4(b) shows the histogram of the size distribution of such dark patches. Figure 3.4(c) shows the magnified view of one such dark patch in the sample irradiated upto the ion fluence of 1×10^{17} ions/cm². The lattice fringes have a d -spacing of ~ 3.23 Å, which correspond to (111) planes of thoria. The fringe widths inside and outside the dark region were compared using the intensity profiles along three lines A, B and C,

shown in Figure 3.4(c). Here, the line B alone passes through the dark region and the lines A and C are running through the perfect matrix of thoria. The peaks in the intensity profile shown in Figure 3.4(d) correspond to the position of the bright fringes in Figure 3.4(c). From the line profile, it may be noted that some of the peaks in line B were shifted with respect to the corresponding peaks in lines A and C. It showed that there was a dilation or expansion of the fringes inside the dark region. Similar lattice expansion was noted in many dark patches in the HRTEM images of the He^+ ion irradiated samples.

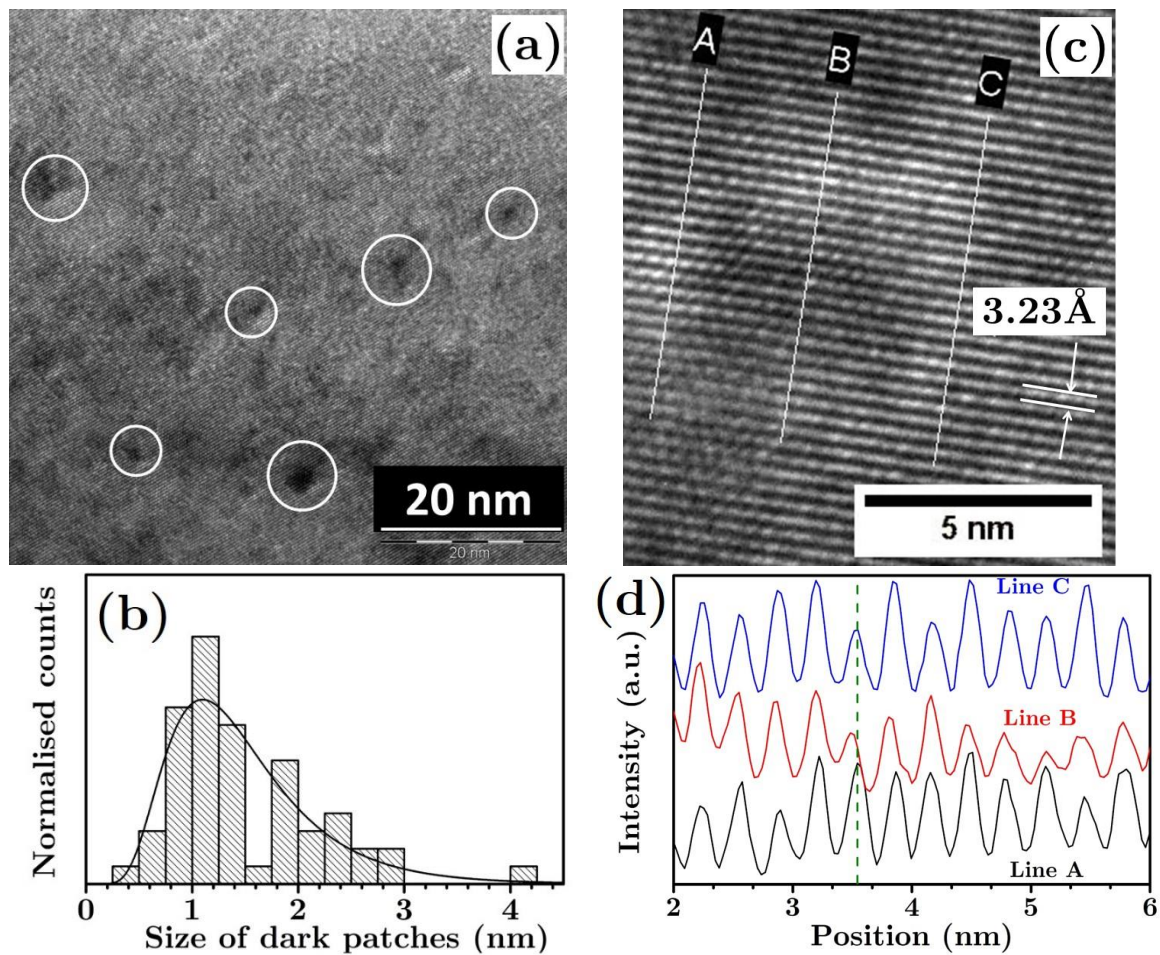


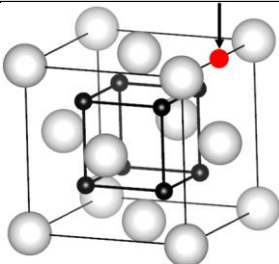
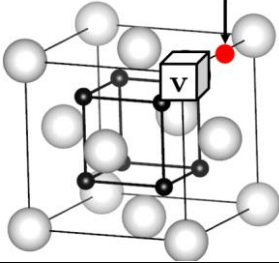
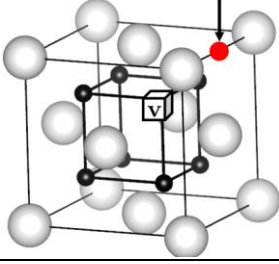
Figure 3.4 (a) The high resolution TEM image of He^+ ion irradiated thoria sample showing the presence of dark patches (b) Histogram of the size distribution of dark patches. (c) close view of one of the dark patches (d) the line profiles of intensities along the lines A, B and C across the dark patch.

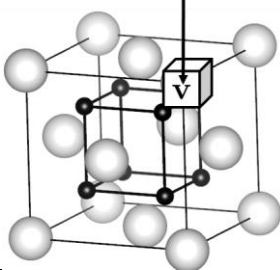
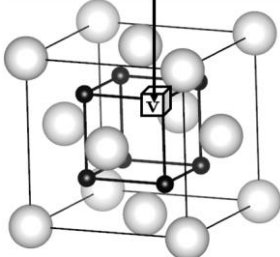
TEM observations, thus, revealed that the additional set of peaks noticed in GIXRD were due to the lattice expansion in the isolated nanometric regions of the samples.

3.3.3. DFT calculations

DFT calculations were used in the present work to understand the role of helium in the formation of isolated nanometric regions of the sample with expanded lattice. DFT calculations were carried out to find (i) the position preferred by the implanted helium atom in the defective thorium, (ii) the possibility of aggregation of interstitial helium atoms and (iii) the lattice expansion due to ordered aggregation of helium atoms in the octahedral interstitial sites. The results are discussed below.

Table 3.2 Helium formation energies at different locations in defective thorium system. (Thorium atoms are represented by white spheres, oxygen by black spheres and helium by red spheres. Vacancy is represented by a cube. The arrow mark notifies the position considered for the formation of helium atom.)

Helium formation site	Formation energy (eV)		
	DFT results	Lu <i>et al.</i> [91]	
	Octahedral interstitial	0.86	0.77
	Octahedral interstitial near a Th-vacancy	0.87	-
	Octahedral interstitial near an O-vacancy	0.81	-

Helium formation site	Formation energy (eV)	
	DFT results	Lu <i>et al.</i> [91]
 Th-vacancy	0.18	0.21
 O-vacancy	2.69	2.48

In defective thoria lattice, there are four different locations, where the implanted helium atom can possibly be accommodated: (1) octahedral interstitial site, (2) Th-vacancy, (3) O-vacancy, (4) octahedral site near Th-vacancy and (5) octahedral site near O-vacancy and all these locations are illustrated in Table 3.2. In order to identify the preferred site among them, the formation energies for helium in these locations were calculated using DFT and listed in Table 3.2. From the table, it can be seen that in the defective thoria lattice, helium prefers Th-vacancy site, which has the lowest formation energy of 0.18 eV. This value was also corroborated by the value (0.21 eV) reported by Lu *et al.*[91].

The octahedral interstitial sites and Th-vacancy sites form a sublattice in the *fcc* lattice of thoria. The sublattice is illustrated in Figure 3.5. Figure 3.5(a) shows an *fcc* unit cell of thoria, with all the octahedral interstitial sites (the body centre position and the edge centre positions) filled with helium atoms. When the network of oxygen atoms are considered separately, they form a cubic sublattice, as illustrated in Figure 3.5(b). On the other hand, the octahedral interstitial sites and the Th-vacancy sites, which have similar chemical environment in first neighbour position, form another sublattice. Lu *et al.*[91] have reported that helium atom diffuses through the sublattice of octahedral interstitial sites and Th-vacancy sites.

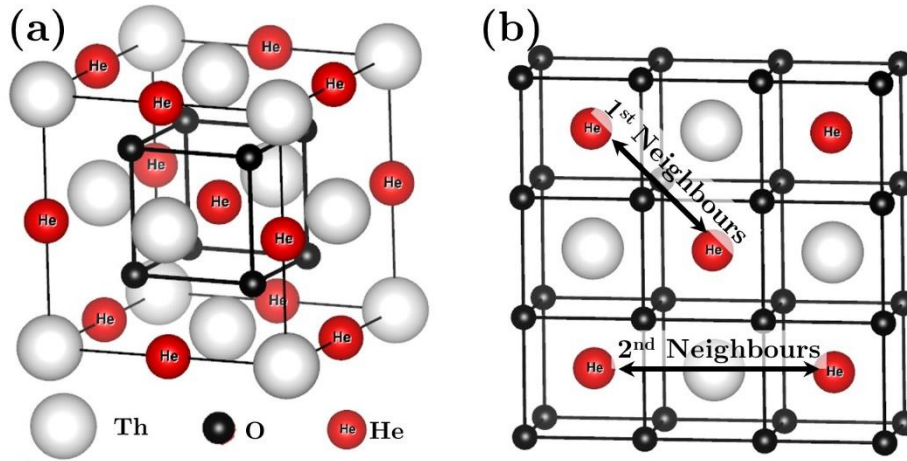


Figure 3.5 (a) The unit cell of thoria along with helium atoms in octahedral interstitial positions. (b) Illustration of the sublattice of oxygen and the sublattice of octahedral interstitial sites and Th-vacancy sites. (Thorium atoms are represented by white spheres, oxygen by black spheres and helium by red spheres with label)

The possibility of aggregation of helium atoms in the octahedral interstitial sites, in the perfect lattice of thoria, was studied by calculating the binding energies of helium atoms in 1st and 2nd neighbour positions within the octahedral interstitial sites. The binding energy values are listed in Table 3.3. A supercell consisting of $2 \times 2 \times 2$ unit cells of thoria were used for the DFT calculations.

Table 3.3 The binding energies for different configurations of helium in thoria lattice.

Configuration	Binding energy per He atom (eV)
Two He atoms in $2 \times 2 \times 2$ units cells of thoria in 2 nd neighbour position as shown in Figure 3.5(b)	- 0.011
Two He atoms $2 \times 2 \times 2$ units cells of thoria in 1 st neighbour position as shown in Figure 3.5(b)	- 0.033
Ordered system where helium decorates all the octahedral interstitial sites (Figure 3.5(a))	- 0.043

Helium atoms showed positive binding in both 1st and 2nd neighbour positions and the binding was stronger in 1st neighbour position. The binding energy per helium atom was found to be the highest (see Table 3.3) in the ordered system,

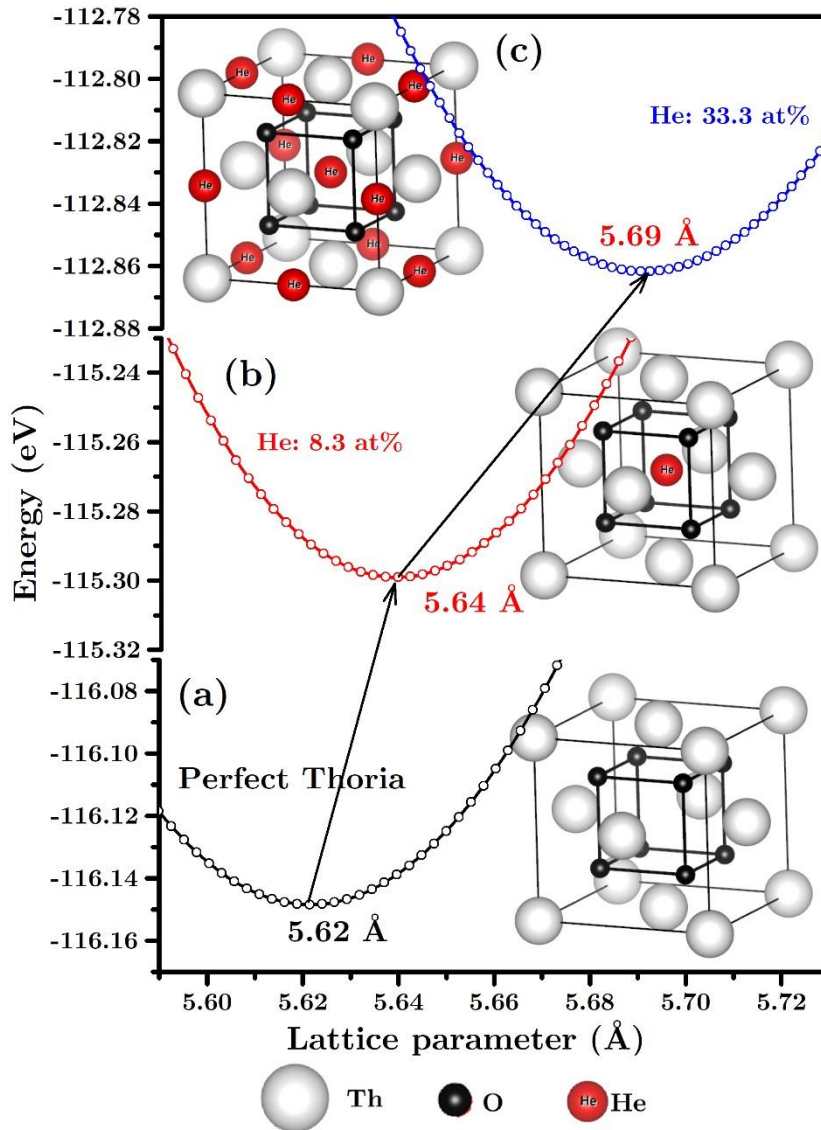


Figure 3.6 Total energies fitted to Birch-Murnaghan equation of state to obtain the lattice parameter for (a) perfect unit cell of thoria, (b) thoria with 8.33 at% of He (1He/unit cell) and (c) thoria with 33 at% of He (4He/unit cell). The lattice parameter increases with helium concentration. (Thorium atoms are represented by white spheres, oxygen by black spheres and helium by red spheres, with label)

where helium atoms filled all the octahedral interstitial sites, as shown in Figure 3.5(a). It is the configuration where all the four octahedral interstitial sites in *fcc* unit cell are occupied by helium atoms and this corresponds to the maximum concentration of helium. Helium shows the highest binding in this configuration. It implies that the helium atoms would prefer to aggregate.

Lattice parameters were calculated using DFT for (i) perfect thoria system, (ii) the system with 1 He atom per unit cell (helium concentration: 8.33 at%) and (iii) the system with 4 He atoms per unit cell (helium concentration: 33.3 at%). The third one is the system with complete ordering of helium atoms in the octahedral interstitial positions. In all the three cases, a single unit cell of ThO₂ was used for DFT calculations. First total energies were calculated for systems with different volumes and the values were fitted to Birch-Murnaghan equation of state[148] to obtain the lattice parameter (see Figure 3.6). The lattice parameter for the perfect thoria was found to be 5.62 Å, which agrees with the experimental value is 5.6 Å. The lattice parameter increased to 5.64 Å, when the system had 1 He atom per unit cell (8.33 at%). It was 5.69 Å, when the system was filled with 4 He atoms per unit cell (33 at%).

3.4. Discussion

The behaviour of the inert gas ‘helium’, inside thoria fuel was studied by irradiating thoria with 100 keV He⁺ ions and characterizing the effects using GIXRD and TEM. The GIXRD patterns of the irradiated samples showed all the standard peaks of thoria, but the peaks were shifted slightly towards lower angles (0.05°), when compared to the as-prepared sample. A set of additional peaks were also observed in the He⁺ ion irradiated samples near the standard diffraction peaks and the additional peaks were shifted to lower 2θ values. The additional peaks correspond to the regions in the sample where the unit cell has expanded. From the measured *d*-spacing it was found that the expansion (Δd) in (111) planes, after irradiation upto the ion fluence of 1×10^{17} ions/cm², was 0.034 Å, and the corresponding change in the lattice constant ($\Delta a/a_0$) was 1.07%. In the sample irradiated upto the ion fluence of 5×10^{16} ions/cm², the expansion in (111) planes was 0.97%. TEM observations revealed that the additional set of peaks noticed in GIXRD were due to the lattice expansion in the isolated nanometric regions of the

samples. Further 4 MeV Si⁺ ion irradiation, which produce approximately the same amount of damage (3.69 *dpa*) in thoria, at the same depth (340 nm), as produced by 100 keV He⁺ ions, resulted only in a small peak shift (0.1°) and did not give rise to any additional peaks. The small peak shift (0.1°) corresponds to a lattice expansion of 0.06%

The small shift (0.05°) in the standard peaks in the He⁺ ion irradiated samples, and the small shift (0.06°) in the Si⁺ ion irradiated sample were attributed to the effects of point defects and defect clusters produced during ion irradiation. Tracy *et al.*[155,156] have studied the effect of 2.2 GeV Au⁺ ions (swift heavy ion (SHI)) in thoria and have particularly investigated the expansion in the unit cell of thoria from the XRD patterns. The authors observed that irradiation induced defects and defect clusters leads to the lattice expansion. The lattice parameter systematically increased with the ion fluence and saturated at 0.05%[155,156]. Akabori *et al.*[157] have studied the effect of additives in irradiation-induced lattice expansion in thoria where fission fragment irradiation to the specimens was carried out by the recoil implantation of fission fragments from Al-U foils enriched by ²³⁵U. According to them the expansion must be related to the behaviour of irradiation-induced and doping-induced point defects, and it saturates at 0.3%. In the present case, in order to understand the role of irradiation induced damages in the lattice expansion, thoria sample was irradiated with 4 MeV Si⁺ ions. From Table 3.1, it may be noted that 4 MeV Si⁺ ions would produce approximately the same amount of damage (3.69 *dpa*) in thoria, at the same depth (340 nm), as produced by 100 keV He⁺ ions. Actually, the projected range of 4 MeV Si⁺ ions was 1.54 μm (with a straggling of 300 nm) and so the concentration of Si atoms at the depth of 340 nm was negligibly small.

Therefore, the additional peaks, which appeared after helium ion implantation, correspond to an unusual lattice expansion of 1.07%, which may not

be due to damage or defects alone. Hence the implanted helium was expected to have played a crucial role in the lattice expansion.

In the present work, the DFT calculations revealed the role of implanted helium atoms in the unusual lattice expansion. Figure 3.6 provides the lattice parameter calculated for perfect thoria system and the lattice parameters for thoria with 8.33 *at%* and 33 *at%* of helium. The lattice parameter of the perfect thoria system was 5.62 Å, which agrees with the experimental value of 5.60 Å. The value increased systematically when the concentration of helium in thoria increased. The lattice parameter was 5.64 Å (*i.e.*, 0.18% expansion) when the helium concentration was 8.33 *at%*. The lattice parameter was 5.69 Å (*i.e.*, 1.25% expansion), in the completely ordered system, where the helium concentration was the maximum of 33 *at%*. This value agreed with the lattice expansion (0.97% and 1.07%) observed experimentally in the present work. Here, the helium ion fluences were 5×10^{16} ions/cm² and 1×10^{17} ions/cm² and the concentration of implanted helium was just 1.17 *at%* and 2.35 *at%*, respectively. So, the large lattice expansion of 1.07%, implied that there was aggregation and ordering of helium in nanometric regions, where helium concentration might be ~33 *at%*.

So, from the DFT calculations, it was concluded that (i) helium atoms prefer the Th-vacancy site in the defective thoria, (ii) helium atoms diffuse through the sublattice consisting of octahedral interstitial and Th-vacancy sites and the strong binding of helium atoms results in aggregation and ordering of helium in the octahedral interstitial sites in thoria matrix, (iii) The ordered aggregation of helium results in lattice expansion of the order of 1.25%, in nanometric regions in thoria.

The number of Th-vacancy would play a crucial role in the diffusion of helium. The number of Th-vacancy could be calculated from the average kinetic energy transfer, T (from 100 keV He⁺ ions to the target atoms), and from the displacement threshold energy, E_d , as follows[25]:

$$T = E_d \ln \left(\frac{\nu E}{E_d} \right)$$

Eqn. 3.3

where, $\nu = 4 M_{\text{He}} M_t / (M_{\text{He}} + M_t)^2$, is the fraction of energy transferred from He^+ ion with mass M_{He} to the target atom with mass M_t , (either Th or O). E is the energy of the incident He^+ ion. The average energy transfer (T) to Th and O atoms were found to be 103 eV and 65.9 eV respectively. It may be recalled that the displacement threshold energy for Th and O atoms in ThO_2 are ~ 53.5 eV and ~ 20 eV respectively[151]. So, every He^+ ion would produce just one or two Th- or O-vacancies in the thoria lattice and not a dense cascade., O interstitials have high mobility compared to Th-vacancy and they have small energy barrier for migration in the matrix of thoria[158,159]. The charge imbalance, created by the high mobility of O, increases the mobility of the Th atoms also[91,160], which in turn helps the helium atoms to diffuse[91] and aggregate in the matrix.

3.5. Summary and conclusion

The aggregation and ordering of helium was studied by irradiating thoria with 100 keV He^+ ions and characterizing the effects using GIXRD and TEM.

- GIXRD and TEM analysis showed that there is a lattice expansion of 1.07% in isolated nanometric regions of the sample. The GIXRD patterns of 4 MeV Si^+ ion irradiated sample proved that damage (point defects and defect clusters) alone will not produce such a large lattice expansion.
- DFT calculations showed that helium prefers Th-vacancy site in the defective thoria system. DFT calculations also showed that helium energetically prefers to aggregate in the octahedral interstitial sites of the *fcc* lattice of thoria. The aggregation and ordering of helium atoms in the octahedral interstitial sites of thoria results in a lattice expansion of 1.25%, which is close to the experimentally observed lattice expansion (1.07%).

- The experiments and calculations confirm that the lattice expansion is due to the aggregation and ordering of helium atoms in nanometric regions of thoria.

Radiation stability of yttrium titanates

4.1. Introduction

Oxide dispersion strengthened (ODS) steels are the candidate structural materials for future nuclear reactors. In ODS steels, the dispersed oxide particles mainly provide the improved creep resistance at high temperatures compared to their conventional ferritic-martensitic counterparts[98,161]. The strength of the ODS steel is derived from the uniformly distributed, highly dense, oxide dispersoids[103,162,163]. Therefore, the high-temperature mechanical properties of ODS steel depends on the radiation stability of the dispersed Y-Ti-O oxide particles, which in turn could depend on the strength and the nature of the metal-oxygen (M-O) bonds. The predominant compositions of Y-Ti-O nanoparticles are $Y_2Ti_2O_7$ and Y_2TiO_5 . The nature of M-O bonds changes with the composition of the Y-Ti-O oxide particles. Hence a comparison of the strength and the nature of the M-O bonds in these two oxide particles ($Y_2Ti_2O_7$ and Y_2TiO_5) could help in deciding the Y-Ti-O composition of the ODS steels.

Lian *et al.*[113] and Zhang *et al.*[114] have studied the temperature dependence of the critical amorphization dose in different rare-earth titanates (pyrochlores) using ion irradiation experiments. Critical amorphization temperature (T_c) is the temperature at which the rate of crystalline recovery is equal to the rate of damage production, and above T_c , the material cannot be amorphized by ion irradiation[164,165]. The critical amorphization temperature (T_c) for $Y_2Ti_2O_7$ and Y_2TiO_5 were found to be 780 K and 623 K respectively, and the T_c value of Y_2TiO_5 is lower than that of $Y_2Ti_2O_7$. It implies that accommodation of ion-induced defects is much enhanced in Y_2TiO_5 as compared to $Y_2Ti_2O_7$. Based on these observations, the authors suggested that an increase in the amount of Y_2TiO_5 oxide particles, instead of $Y_2Ti_2O_7$, may improve the radiation resistance of the ODS steel. Further,

the degree of covalency in the M-O bonds in $\text{Y}_2\text{Ti}_2\text{O}_7$ and Y_2TiO_5 were compared earlier by Jiang *et al.*[104] using DFT calculations and it was reported that the Ti-O bonds exhibit higher covalency than the Y-O bonds and the ionic bonding dominates in both these oxides.

The radiation stability of both the oxides were studied by irradiating the oxide samples, $\text{Y}_2\text{Ti}_2\text{O}_7$ and Y_2TiO_5 , with low energy krypton ions (70 keV Kr^+ ions) and by analyzing the changes in the microstructure using GIXRD, TEM and EELS. Further, the nature of the M-O bonds of the two oxide particles $\text{Y}_2\text{Ti}_2\text{O}_7$ and Y_2TiO_5 were compared using electron energy loss spectroscopy (EELS).

4.2. Experimental and computational methods

4.2.1. Experimental methods

The powder samples of $\text{Y}_2\text{Ti}_2\text{O}_7$ and Y_2TiO_5 were synthesized by the conventional solid state reaction route from the precursor materials Y_2O_3 and TiO_2 . To synthesize $\text{Y}_2\text{Ti}_2\text{O}_7$, the precursors Y_2O_3 and TiO_2 were taken in the molecular ratio of 1:2 and the mixture was calcined at 1250 °C in air for 48 hours[131]. Y_2TiO_5 was synthesized with the same precursors Y_2O_3 and TiO_2 , taken in the molecular ratio of 1:1 and the mixture was calcined at 1500 °C in air for 24 hours[132]. The formation of the respective phases were confirmed with the X-ray diffraction patterns. The powder samples of $\text{Y}_2\text{Ti}_2\text{O}_7$ and Y_2TiO_5 were then pelletized and the pellets were sintered at 900 °C for 8 hours. The sintered pellets were used for the ion irradiation experiments.

The radiation stability of both the oxides were studied by irradiating the pellets with 70 keV Kr^+ ions at room temperature, upto 1×10^{17} ions/cm². The irradiations were carried out in 150 kV ion accelerator. The base vacuum in the irradiation chamber was maintained at 5×10^{-6} mbar and the beam current was restricted to $< 1 \mu\text{A}$ to avoid heating of the specimen. The dose rate was 5×10^{14} ions/cm²/s.

The TEM specimens were prepared by scratching the surface of the pellets using a scalpel blade and by dispersing it in the carbon coated copper grid with the help of propanol. The samples were analysed using LIBRA-200FE HRTEM. The samples were characterized using electron energy loss spectroscopy (EELS) and energy dispersive X-ray (EDS) spectroscopy techniques.

4.2.2. Computational methods

The L edges in the EELS spectra of transition metals are strongly modified by the empty $3d$ density of states, due to the strong overlap of $2p3d$ wave function, or more precisely by the intra-atomic $2p3d$ two-electron integrals; this is called multiplet effect[166]. Due to the multiplet effect, the ionization edge of a transition metal deviates significantly from the density of the ground state of the same metal.

Since the ionization edges in EELS is essentially a measure of the joint density of states, they can be calculated using DFT, particularly, DFT can predict K edges very well. But since DFT is based on single electron calculations, it cannot calculate L edges reliably. The L_{23} edges of transition metals can be reliably simulated with Crystal Field Multiplet (CFM) and Charge Transfer Multiplet (CTM) models[149,167].

In the present chapter, the Oxygen K edges and Ti L_{23} edges were simulated with CASTEP[146], the DFT code included in Materials Studio package. The Ti L_{23} edges were analyzed also using the freely available program CTM4XAS (Charge Transfer Multiplet program for X-ray Absorption Spectroscopy)[168].

4.2.2.1. Simulation of EEL spectra using DFT

CASTEP uses plane wave basis set. PAW (Projector Augmented Wave) pseudopotentials are generated in CASTEP, using on-the-fly formalism. Perdew, Burke and Erzenhof (PBE) version of generalized gradient approximation (GGA)[145] is used in the calculations to describe the exchange and the correlation effects. Brillouin zone sampling is performed using Monkhorst-Pack scheme[154]. Convergence tests were carried out in $Y_2Ti_2O_7$ and Y_2TiO_5 for both Brillouin zone

sampling and plane wave energy cutoff, until the energy converged to 0.001 eV per atom. For expanding the wave function of the valence electrons, a plane wave

Table 4.1 The crystal structure details of $Y_2Ti_2O_7$ (fcc system with the space group 227 ($Fd\bar{3}m$), setting 2). The value of the lattice parameter a is 10.09\AA (expt.) 10.15\AA (calc.).

Atoms	Wycoff position	Fractional coordinates			Formal charge	Mulliken charge
		x	y	z		
Y	16c	0.5	0.5	0.5	4	1.15
Ti	16b	0	0	0	3	1.43
O1	48f	0.329	0.125	0.125	-2	-0.72
O2	8b	0.375	0.375	0.375	-2	-0.83

cut-off value of 600 eV was used in the case of $Y_2Ti_2O_7$ and 650 eV was used in the case of Y_2TiO_5 . A mesh of $6\times 6\times 6$ k -points was considered for Brillouin zone integration in $Y_2Ti_2O_7$ and a mesh of $4\times 12\times 4$ was used in Y_2TiO_5 . The valence

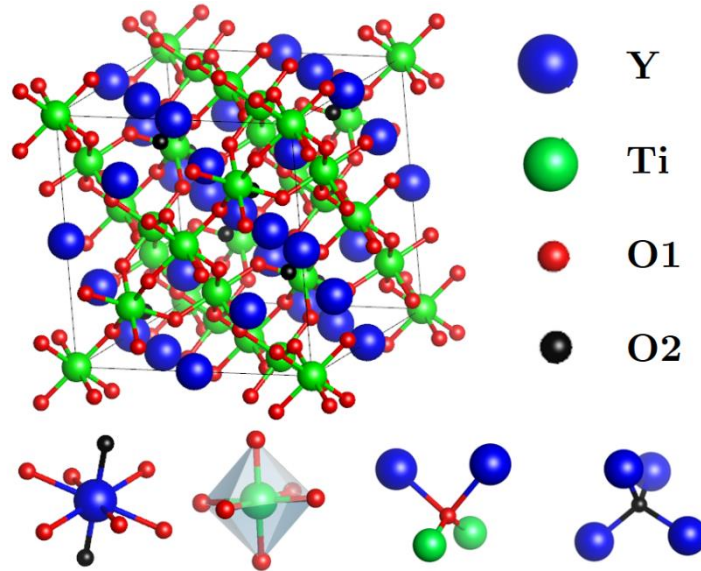


Figure 4.1 The unit cell of pyrochlore $Y_2Ti_2O_7$. Chemical environment of all the atomic species of $Y_2Ti_2O_7$ are illustrated individually.

electronic configurations used for each atomic species were: Y $4d^15s^2$; O $2s^22p^4$; Ti $3d^24s^2$. The unit cells were relaxed using DFT and the optimized lattice constants and atom positions for both the systems are given in Table 4.1 and Table 4.2. The crystal structures of both the systems are shown in Figure 4.1 and Figure 4.2.

Table 4.2 The crystal structure details of Y_2TiO_5 (orthorhombic with space group $Pnma$ (62)). The experimentally observed lattice parameters (a , b , c) are (10.33, 3.699, 11.18)Å and the calculated values are (10.40, 3.701, 11.31)Å.

Atoms	Wyckoff position	Fractional coordinates			Formal charge	Mulliken charge
		x	y	z		
Y1	4c	0.1157	0.25	0.2243	3	1.37
Y2	4c	0.1361	0.25	0.5565	3	1.35
Ti	4c	0.1739	0.25	0.8811	4	1.09
O1	4c	0.4941	0.25	0.1047	-2	-0.81
O2	4c	0.2240	0.25	0.0436	-2	-0.77
O3	4c	0.2569	0.25	0.7303	-2	-0.76
O4	4c	0.5075	0.25	0.6556	-2	-0.72
O5	4c	0.2636	0.25	0.3842	-2	-0.73

The ionization edges in the EEL spectra were calculated using CASTEP. Oxygen K-edge was generated by introducing a core hole in one of the O atom, *i.e.*, removing an electron from the 1s orbital of the O atom. Similarly, Ti L_{23} -edge was calculated by introducing a core hole in the 2p orbital of Ti atom[169].

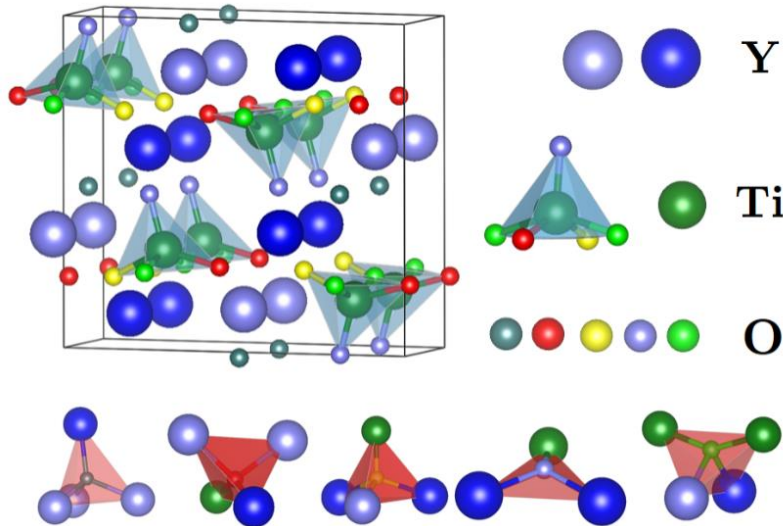


Figure 4.2 The unit cell of orthorhombic Y_2TiO_5 . Chemical environment of all the atomic species of Y_2TiO_5 are illustrated individually.

4.2.2.2. Simulation of EEL spectra using CTM4XAS

CTM4XAS uses the charge transfer multiplet program as developed by Theo Thole and modified by Haruhiko Ogasawara[170]. While simulating XAS or EELS

edges in CTM4XAS, one has to tune many parameters like the parameters related to configuration, symmetry, Slater integral reduction parameters (F_{dd} , F_{pd} , G_{pd}), spin orbit coupling values, crystal field parameters (which includes symmetry of the crystal system and the energy split $10Dq$), charge transfer parameters ($T(eg)$, U_{dd} , U_{pd} , etc.) and Lorentzian and/or Gaussian broadening values. The parameters are tuned so that the simulated spectrum matches with the experimental one. The F_{dd} and F_{pd} represent the radial parts of the $2p$ - $3d$ coulomb multi-pole interactions while G_{pd} represents the exchange multi-pole interactions[171]. The default value for F_{dd} , F_{pd} and G_{pd} is 80% of their Hartree-Fock calculated value and is shown to be close to the optimized value to simulate the multiplet spectra of atoms[172].

4.2.2.3. Stacking fault energy calculation

Stacking fault is an interruption of the normal stacking sequence of atomic planes in the structure of face centered cubic or hexagonal close packed crystal system. Stacking fault formation energy (SFE) is the excess energy associated with the intrinsic stacking faults. Molecular dynamics simulations are used to calculate the intrinsic stacking fault energy in a crystal system like *fcc* or *bcc*. The SFE is calculated as the difference between the total energy of the defective supercell and the perfect supercell. The perfect supercell is generated after reorienting the conventional *fcc* or *hcp* structure along (111) direction, so that the z -axis in the simulation cell passes normal to the layers A, B, and C. The defective supercell is the one which contains a stacking fault. The stacking fault is introduced by one of the following two methods. The supercell is divided into two parts by selecting a xy -plane at half the z -dimension. Then all the atoms in one part is shifted along x and y direction, so as to introduce an intrinsic stacking fault.

Alternatively, defective supercell is created also by slicing the perfect supercell into three parts along z direction, where the central slice will contain only one A (or B or C) layer. This slice is removed and the defective supercell is obtained by moving the top slice close to bottom slice by one layer. It may be noted that

MD uses periodic boundary conditions. In order to nullify the effect of the defect on its image during MD calculations, arbitrary empty space is introduced in this supercell in the z -direction. The total energy changes with the dimension of the empty space and saturates when the effect of the image becomes insignificant with sufficient empty space.

4.3. Results

The as-prepared and the 70 keV Kr^+ ion irradiated specimens were characterized using GIXRD, high resolution TEM and Raman scattering techniques.

4.3.1. GIXRD analysis

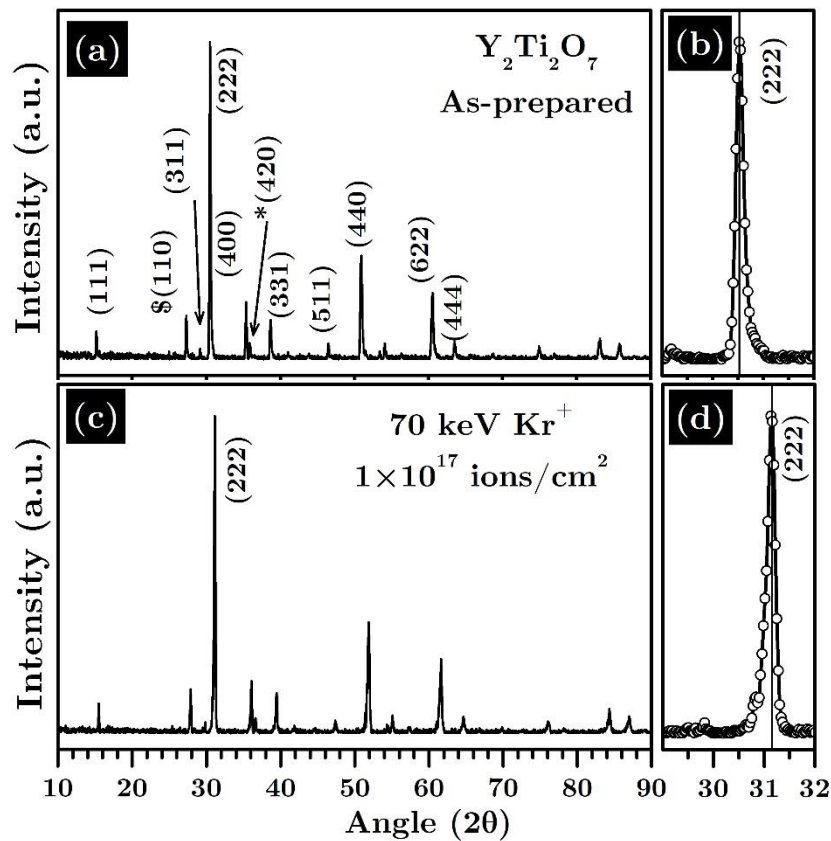


Figure 4.3 GIXRD patterns of $\text{Y}_2\text{Ti}_2\text{O}_7$ (a) as-prepared and (c) irradiated with 70 keV Kr^+ ion, upto a fluence of 1×10^{17} ions/ cm^2 . The diffraction peaks of the unreacted precursors Y_2O_3 and TiO_2 are marked with \$ and *, respectively. Plots (b) and (d) show the expanded view of the prominent peak (222). There is a shift in the (222) peak from 30.5° to 31.1° .

Figure 4.3(a) and Figure 4.3(c) show the GIXRD patterns of the as-prepared and the 70 keV Kr^+ ion irradiated $\text{Y}_2\text{Ti}_2\text{O}_7$ samples. The GIXRD pattern of the as-prepared sample is indexed to pyrochlore face centered cubic structure (JCPDS #420413). The XRD peaks of the unreacted precursors Y_2O_3 and TiO_2 were also found in the XRD and were marked with \$ and * respectively.

In the Kr^+ ion irradiated $\text{Y}_2\text{Ti}_2\text{O}_7$ sample, all the peaks were shifted towards higher 2θ values as compared to the peaks in the as-prepared sample. For instance, the magnified view of the prominent peak (222) (Figure 4.3(b) and Figure 4.3(d)), shows a shift from 30.5° to 31.1° . A shift in the XRD peak position is related to different types of internal stresses and planar faults such as stacking faults or twin boundaries[173].

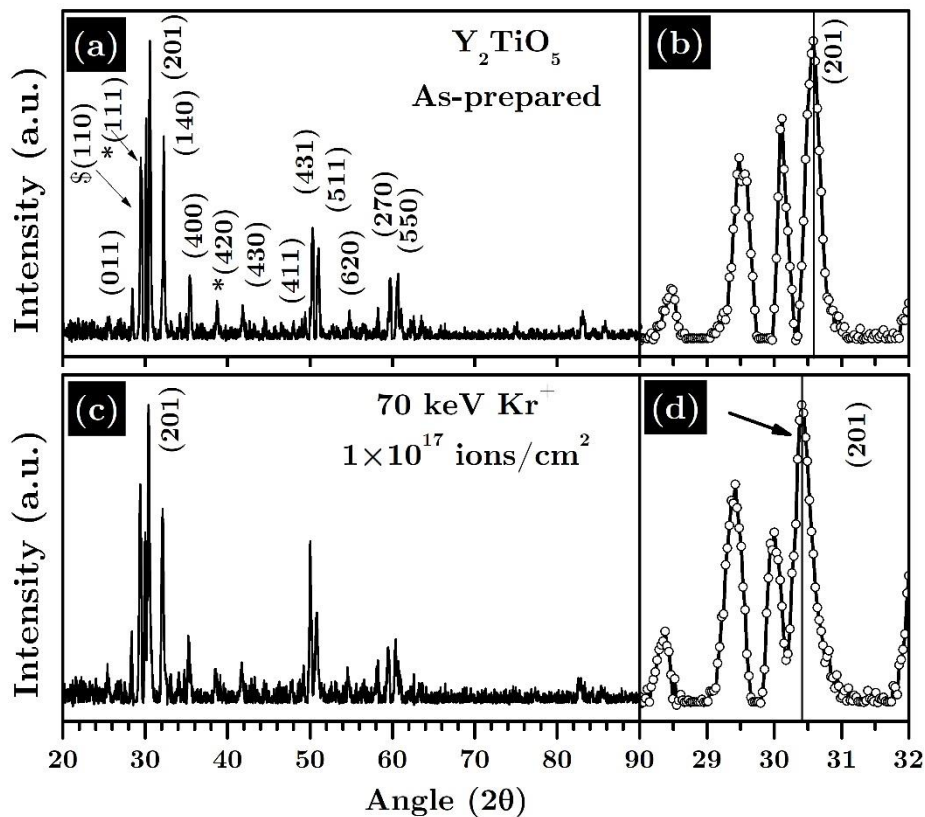


Figure 4.4 GIXRD patterns of Y_2TiO_5 (a) as-prepared and (c) irradiated with 70 keV Kr^+ ion, upto a fluence of 1×10^{17} ions/ cm^2 . The diffraction peaks of the unreacted precursors, Y_2O_3 and TiO_2 , are marked with \$ and * respectively. Plots (b) and (d) show the expanded view of the prominent peak (201). FWHM of the peak (201) has increased from 0.19° to 0.26° .

The GIXRD patterns of the as-prepared and the 70 keV Kr⁺ ion irradiated Y₂TiO₅ samples are shown in Figure 4.4(a) and Figure 4.4(c). The patterns were indexed to the orthorhombic Y₂TiO₅ (JCPDS #400795). The XRD peaks of the unreacted precursors Y₂O₃ and TiO₂ were marked with \$ and * respectively. The magnified view of the prominent peak (201) is shown in Figure 4.4(c) and Figure 4.4(d). It was observed that there was a small peak shift to lower 2θ upon irradiation (from 30.6° to 30.4°). The peak width has increased significantly from 0.19° to 0.26°. The broadening of diffraction peaks in the XRD may be caused either by the reduction in crystallite size or by strain[173].

In order to understand the peak shift in the case of Y₂Ti₂O₇ and the broadening in the case of Y₂TiO₅, the microstructure of the samples were examined under high resolution transmission electron microscope.

4.3.2. Microstructural analysis – TEM

Y₂Ti₂O₇ powders, after synthesis, were first analysed with TEM to confirm the formation of the phase. Figure 4.5(a) shows the bright field TEM image of the particles of Y₂Ti₂O₇ in low magnifications. Figure 4.5(b) shows the selected area electron diffraction (SAED) pattern, where the spots were indexed to (110), (200) and (110) planes of Y₂Ti₂O₇; the zone axis was ⟨002⟩ (JCPDS #420413). Figure 4.5(c) shows the high resolution TEM image of the crystalline matrix of Y₂Ti₂O₇, where the lattice fringes were indexed to (222) planes of Y₂Ti₂O₇ and the zone axis was identified as ⟨011⟩. Figure 4.5(d) shows the EDS spectra along with the composition of the elements Y, Ti and O in at%, which agrees with the phase of Y₂Ti₂O₇.

In order to understand the peak shift in the GIXRD pattern of the (70 keV Kr⁺ ion) irradiated sample, the microstructural changes in the surface region of the pellet was analysed using TEM. Figure 4.6 shows the high resolution TEM images of the irradiated sample, where it may be noticed that stacking faults were introduced uniformly throughout the sample as a result of ion irradiation.

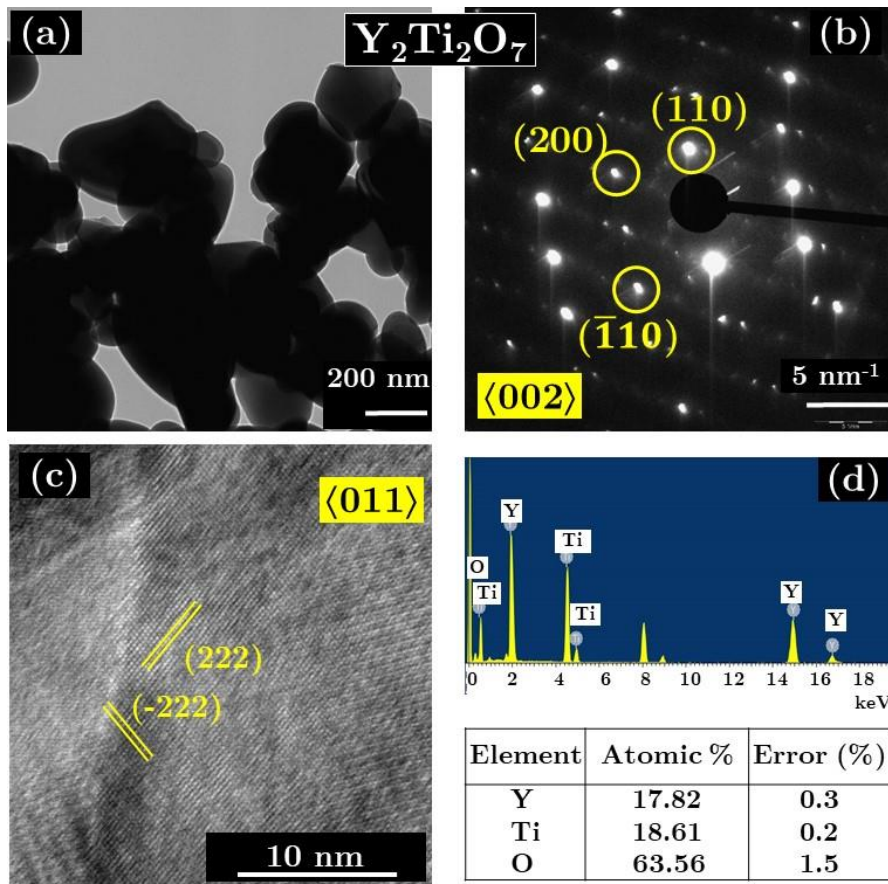


Figure 4.5 (a) TEM image showing $Y_2Ti_2O_7$ particles (b) SAED pattern of $Y_2Ti_2O_7$ (zone axis: $\langle 002 \rangle$); (c) HRTEM image showing the lattice fringes of crystalline $Y_2Ti_2O_7$ (zone axis $\langle 011 \rangle$); (d) composition analysis with EDS.

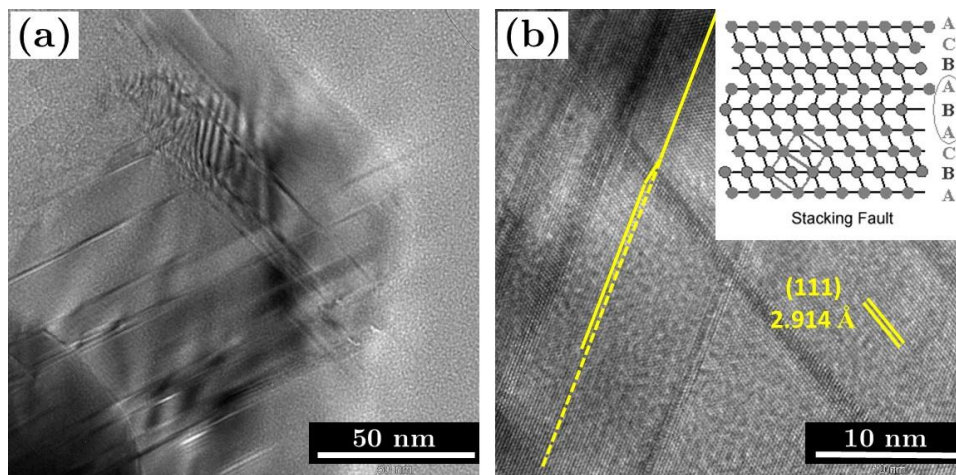


Figure 4.6 High resolution TEM images of $Y_2Ti_2O_7$ sample irradiated with 70 keV Kr^+ ions, showing the presence of stacking faults.

The HRTEM image further showed that the stacking faults were actually along (111) planes in the *fcc* pyrochlore structure of $Y_2Ti_2O_7$. It was also noticed that the

material has retained its crystal structure except for the appearance of stacking faults. The shift in the XRD peak position, noticed in $Y_2Ti_2O_7$ (Figure 4.3(d)) could be a manifestation of these stacking faults.

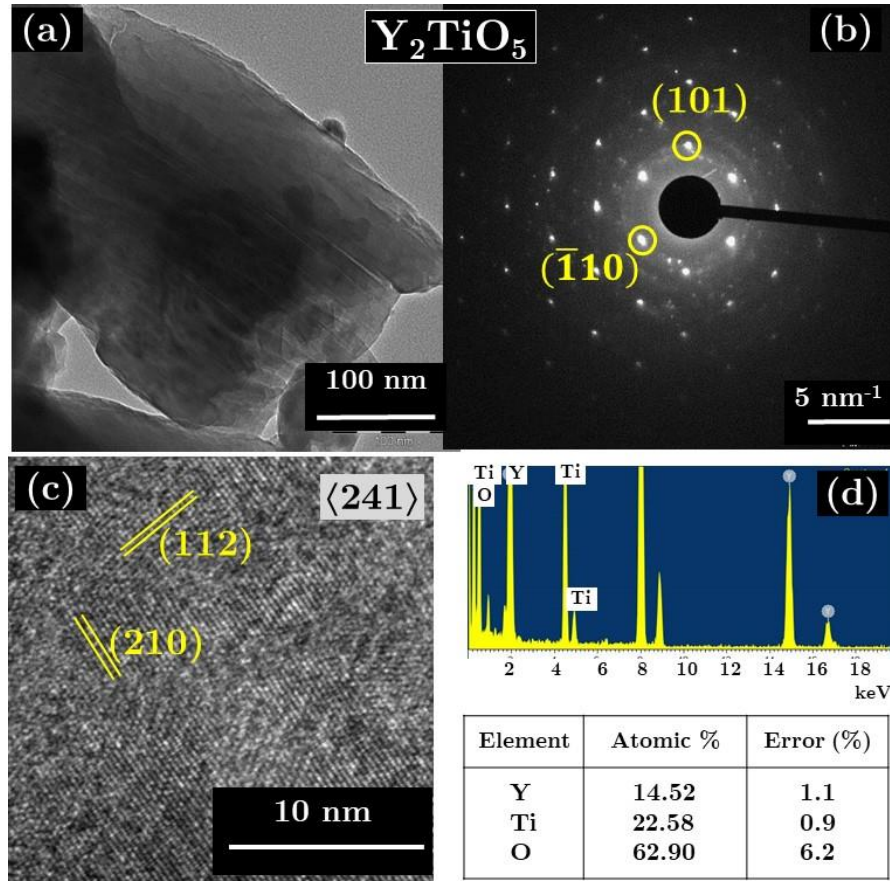


Figure 4.7 (a) TEM image showing Y_2TiO_5 particles; (b) SAED pattern from a single crystal Y_2TiO_5 particle (c) HRTEM image showing the lattice fringes of crystalline Y_2TiO_5 (zone axis: $\langle 241 \rangle$); (d) composition analysis with EDS.

The stacking fault energy in the present case was calculated using molecular dynamics (MD) simulations to be $180 \text{ meV}/\text{\AA}^2$. found and this value was found to be larger than the typical SFE in case of steels[174,175]. SFE modifies the ability of a dislocation in a crystal to glide onto an intersecting slip plane. When the SFE is low, the mobility of dislocations in a material decreases.

Similarly the phase of the Y_2TiO_5 powders synthesized, was confirmed with TEM. Figure 4.7(a) shows bright field TEM image of Y_2TiO_5 particle at low magnification. Figure 4.7(b) shows the selected area electron diffraction (SAED) pattern of Y_2TiO_5 sample and the spots were indexed to (101) and (110) planes of

the orthorhombic structure of Y_2TiO_5 (JCPDS #400795). Figure 4.7(c) shows the high resolution TEM image of the crystalline matrix. The planes were indexed to (112) and (210) planes of Y_2TiO_5 and the zone axis was identified as $\langle 241 \rangle$. Figure 4.7(d) shows the EDS spectra along with the composition of the elements Y, Ti and O, which was found to agree with the phase Y_2TiO_5 .

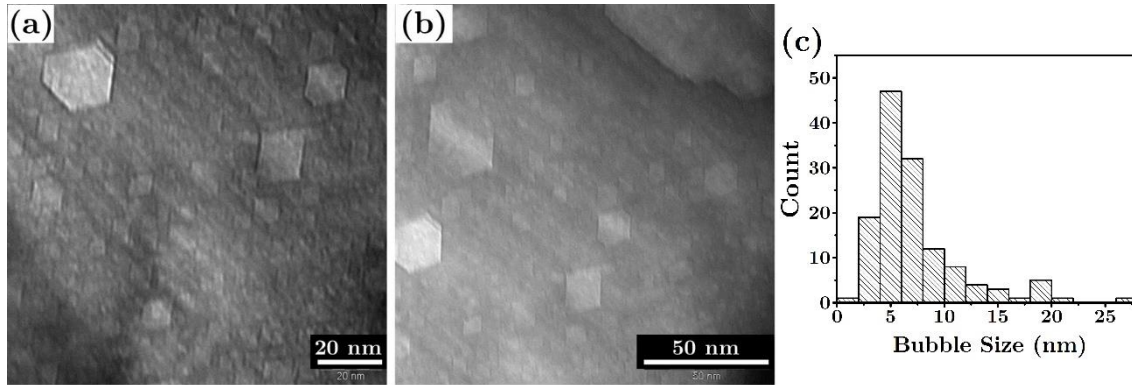


Figure 4.8 (a) and (b) bright field TEM images of Y_2TiO_5 sample irradiated with 70 keV Kr^+ ions, showing the formation of faceted krypton bubbles. (c) Histogram showing the size distribution of the bubbles

In order to understand the peak broadening in the GIXRD patterns of ion irradiated Y_2TiO_5 sample, the surface region of the pellet was analysed under TEM. From the bright field TEM images Figure 4.8(a) and (b), shows the bright field TEM images of the krypton ion irradiated Y_2TiO_5 samples. It was seen that the implanted krypton has formed faceted bubbles in the matrix. The bubbles were seen uniformly throughout the sample and all the bubbles were invariably faceted in shape. Particularly, the faces of the bubbles were clearly aligned along in particular direction in the lattice. It implied that the bubble growth was guided by the breaking of bonds along the lowest energy planes (the cleavage planes) followed by trapping of krypton and nucleation and growth of the bubble.

The swelling due to the bubbles was calculated as $S_b = \frac{\pi}{6} \Sigma d^3 / st \times 100\%$. This equation is based on basic geometry assuming spherical bubbles. Here d is the diameter of individual bubbles, s the area of the TEM image, t the sample thickness (assumed to be 50 nm). The swelling was found to be 2.34%.

4.3.3. Raman scattering analysis

The effects of 70 keV Kr^+ ion irradiation in $\text{Y}_2\text{Ti}_2\text{O}_7$ were also characterized with Raman scattering. Marianne *et al.*[176] have carried out factor group analysis of $\text{A}_2\text{B}_2\text{O}_7$ pyrochlore structures (space group $Fd3m$) and predicted the vibrational optical normal modes as follows:

$$\Gamma_{\text{optical}} = A_g^{(R)} + 3A_{2u}^{i.a} + E_g^R + 3E_u^{(i.a)} + 2F_{1g}^{(i.a)} + 7F_{1u}^{(IR)} + 4F_{2g}^R + 4F_{2u}^{i.a} \quad \text{Eqn. 4.1}$$

Here (R) denotes Raman active, (IR) denotes infrared active and ($i.a$) denotes inactive mode. More interestingly the authors have reported that there would not be any Raman active vibrations associated with A ions and B ions, while the Raman active vibrations associated with the two different O atoms would be:

$$\begin{aligned} \text{O 1} &: A_g + E_g + 3F_{2g} \\ \text{O 2} &: F_{2g} \end{aligned}$$

$$\text{Eqn. 4.2}$$

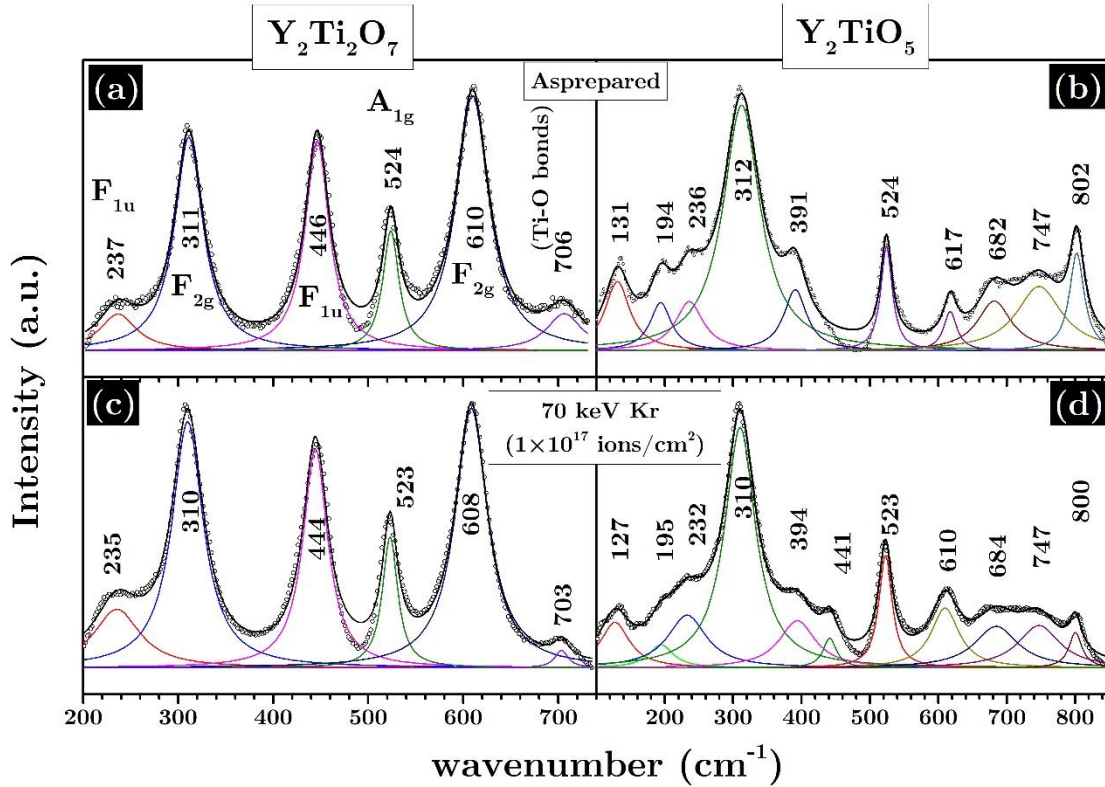


Figure 4.9 (a) and (b) show the Raman spectra of the as-prepared samples of $\text{Y}_2\text{Ti}_2\text{O}_7$ and Y_2TiO_5 respectively. (c) and (d) show the Raman spectra of $\text{Y}_2\text{Ti}_2\text{O}_7$ and Y_2TiO_5 , after irradiation with 70 keV Kr^+ ions.

Figure 4.9(a) shows the Raman scattering from the as-prepared $Y_2Ti_2O_7$ sample. The modes were identified, based on earlier works[177,178], as F_{1u} (237 cm^{-1}), F_{2g} (311 cm^{-1}), F_{1u} (446 cm^{-1}), A_{1g} (524 cm^{-1}), F_{2g} (610 cm^{-1}) and the peak at 706 cm^{-1} is associated with the vibrations of Ti-O bonds. F_{1u} modes were associated with the IR active mode which is associated with disorder, in the present case, it may appear due to grain boundaries. F_{2g} and A_{1g} were associated with the optical phonon modes. A_{1g} was associated with the vibrations of O1 atom and F_{2g} was associated with the vibrations of both O1 and O2 atoms. In $Y_2Ti_2O_7$, O1 atoms reside in a tetrahedron defined by two Y and two Ti atoms, while O2 atoms reside in a tetrahedron defined by four Y atoms (see Figure 4.1).

Table 4.3 The profile of the peaks in the Raman spectra of $Y_2Ti_2O_7$ before and after the irradiation with 70 keV Kr^+ ions (1×10^{17} ions/cm²).

Peak position (cm ⁻¹)		FWHM (cm ⁻¹)		Vibration Modes[177]
Before irradiation	After irradiation	Before irradiation	After irradiation	
237(±1.7)	236(±1.3)	47(±6.2)	59(±5.5)	F_{1u} IR active
311(±0.2)	310(±0.2)	37(±0.8)	40(±0.8)	F_{2g} O1, O2
446(±0.2)	444(±0.2)	31(±0.7)	32(±0.7)	F_{1u} IR active
524(±0.3)	523(±0.3)	21(±0.9)	20(±0.8)	A_{1g} O1
610(±0.2)	608(±0.2)	42(±0.7)	41(±0.7)	F_{2g} O1, O2
706(±1.6)	703(±2.0)	45(±5.9)	17(±5.9)	- Ti-O bond

Figure 4.9(c) shows the Raman scattering from $Y_2Ti_2O_7$ sample irradiated with 70 keV Kr^+ ions upto the ion fluence of 1×10^{17} ions/cm². It contains all the Raman modes that were present in the as-prepared sample. The position and width of all the Raman modes in the spectra are given in Table 4.3. The table shows that there was no significant change in the peak positions or the peak width, which suggest absence of any strain in the lattice and absence of any change in bond lengths.

The effects of 70 keV Kr^+ ion irradiation in Y_2TiO_5 were characterized similarly with Raman scattering. Marianne *et al.*[176] have analysed the case of

Y_2TiO_5 also, and listed the optical normal modes of Y_2TiO_5 (space group: 62, $Pnma$) as:

$$\Gamma_{\text{optical}} = 16A_g^{(R)} + 8A_u^{(i.a)} + 8B_{1g}^R + 15B_{1u}^{IR} + 16B_{2g}^R + 7B_{2u}^{IR} + 8B_{3g}^R + 15B_{3u}^R \quad \text{Eqn. 4.3}$$

where, (R) denotes Raman active mode, (IR) denotes infrared active mode and ($i.a$) denotes inactive mode. Raman active vibrations per set of ion are:

$$\text{Y } 1 : 2A_g + B_{1g} + 2B_{2g} + B_{3g} \quad \text{Eqn. 4.4}$$

and the same for rest of the ions.

Table 4.4 The peak position and FWHM of the Raman spectra of Y_2TiO_5 before and after the irradiation (70 keV Kr^+ ions, ion fluence: 1×10^{17} ions/cm²).

Peak position (cm ⁻¹)		FWHM (cm ⁻¹)		Type of bonding
Before irradiation	After irradiation	Before irradiation	After irradiation	
131(±0.8)	127(±1.0)	44(±3.3)	51(±4.5)	Translational modes involving the movements of Y cations
194(±1.6)	195(±3.7)	37(±6.3)	43(±15.0)	
236(±2.0)	233(±3.6)	50(±8.4)	69(±11.0)	
312(±0.3)	310(±0.2)	66(±1.5)	54(±1.1)	
391(±0.8)	394(±1.3)	41(±3.0)	64(±6.0)	Related to internal vibrations of the TiO ₅ groups
–	441(±0.9)	–	23(±3.8)	
524(±0.3)	523(±0.2)	20(±0.9)	24(±0.7)	
617(±1.0)	610(±0.7)	23(±3.4)	49(±3.0)	
682(±2.0)	685(±2.7)	60(±8.8)	77(±12.3)	
747(±2.1)	747(±2.5)	81(±11.3)	74(±11.7)	
802(±0.4)	800(±0.7)	26(±2.1)	23(±3.4)	

Figure 4.9(b) and Figure 4.9(d) show the Raman spectrum of the as-prepared and the 70 keV Kr^+ ion irradiated Y_2TiO_5 samples respectively. The low symmetry of the orthorhombic unit cell manifests itself in more number of Raman peaks. The peaks identified in both the spectra are listed in Table 4.4. Here the modes with low-frequency ($<300\text{-}350 \text{ cm}^{-1}$) are assigned to the translational modes involving the movements of Y cations and the vibrational frequencies above 350 cm^{-1} are related to internal vibrations of the TiO_5 groups[179] (TiO_5 polyhedra is shown in Figure

4.2.) From Table 4.4, it was observed that majority of the peaks, associated with both Y and Ti, had broadened upon irradiation. Broadening in the Raman mode is caused by the distribution in the bond lengths. Here, the broadening could be due to the bubbles (as evident from TEM observations) and other irradiation induced disorders.

4.4. Characterization of the M-O bonds

4.4.1. M-O bonds in $Y_2Ti_2O_7$ and Y_2TiO_5

The nature of the M-O bonds in the complex oxide systems $Y_2Ti_2O_7$ and Y_2TiO_5 are significantly different from that of the constituent precursor materials, Y_2O_3 and TiO_2 .

The electronic, structural, and optical properties of crystalline yttria (Y_2O_3) have already been studied extensively[180,181]. Y_2O_3 has a (fluorite like) cubic structure of space group $Ia\bar{3}(T_h^7)$ (No. 206). The unit cell contains two inequivalent cation sites, Y1 at the $8a$ site and Y2 at the $24d$ site, and one type of O at the $48e$ site. The cubic cell contains a total of 80 atoms. Yttria is far from being fully ionic, and the bonding between Y and O has a substantial covalent component. Xu *et al.*[180,181] have suggested that yttria cannot be considered as an ionic crystal, especially it cannot be described as an ionic compound like $Y_2^{+3}O_3^{-2}$, rather it should be close to $Y_2^{+2.16}O_3^{-1.44}$.

TiO_2 , has three different phases: rutile, anatase and brookite with different space groups $P4_2/mnm$ (tetragonal), $I4_1/amd$ (tetragonal) and $Pbca$ (orthorhombic) respectively[182]. The ionic and the covalent bonds in TiO_2 originate from the charge transfer between Ti and O atoms and the hybridization of Ti $3d$ and O $2p$ orbitals. The Ti-O bonds in TiO_2 is in fact more ionic than predicted by the band theory[183]. The band-theory calculation suggests that Ti e_g hybridize with O p_x+p_y orbitals to form covalent bonds, while Ti t_{2g} hybridize with O p_z to form weak bonds.

Thus the rutile structure results from the combined effect of covalency and electrostatics.

Given the variation in the nature of bonds in the precursor materials Y_2O_3 and TiO_2 , the characterization of the nature of the bonds in Y-Ti-O complexes becomes more interesting and important.

The precursor materials Y_2O_3 and TiO_2 forms different complex oxide systems such as $Y_2Ti_2O_7$, Y_2TiO_5 and $YTiO_5$ where the first two stoichiometries are most stable since they have relatively more negative heat of formation[111]. $Y_2Ti_2O_7$, Y_2TiO_5 are also the predominant oxide particles seen in ODS steels.

$Y_2Ti_2O_7$ exists in *fcc* pyrochlore structure (space group, $Fd3m, O_h^7$). The Wyckoff positions of the atoms are: Y at $16c$ ($\frac{1}{2}, \frac{1}{2}, \frac{1}{2}$), Ti at $16b$ (0, 0, 0), O1 at $48f$ ($\delta, \frac{1}{8}, \frac{1}{8}$) and O2 at $8b$ ($\frac{3}{8}, \frac{3}{8}, \frac{3}{8}$). Figure 4.1 shows the crystal structure of $Y_2Ti_2O_7$. The two non-equivalent oxygen sites, O1 and O2, differ in chemical environment: O1 atoms reside in a tetrahedron defined by two Y and two Ti atoms, while O2 atoms reside in a tetrahedron defined by four Y atoms.

The orthorhombic Y_2TiO_5 has a complicated structure (space group, Pnma or D_{2h}^{16}). All atoms take the Wyckoff position $4c$, with coordinates $x, \frac{1}{4}, z$, $(-x + \frac{1}{2}, \frac{3}{4}, z + \frac{1}{2})$, $(-x, \frac{3}{4}, -z)$ and $x + \frac{1}{2}, \frac{1}{4}, -z + \frac{1}{2}$. They lie in the mirror planes at $y = \frac{1}{4}$ or $\frac{3}{4}$. Figure 4.2 shows the orthorhombic crystal structure of Y_2TiO_5 . The Ti-O bond distances vary in the range of 1.79-1.97 Å, and the Y-O bond distances vary in the range of 2.28-2.40 Å[104].

The crystal field splitting in the $3d$ -orbital of the transition metal atom Ti is strongly influenced by the chemical environment and the symmetry of neighbour atoms. In the case of $Y_2Ti_2O_7$, the Ti atoms are octahedrally surrounded by O atoms and in Y_2TiO_5 , the Ti atoms are surrounded by 5 oxygen atoms forming a square pyramid having four-fold rotational symmetry, which is called as the C_4 (pyramidal) symmetry. The change in the symmetry around Ti atom affects the crystal field splitting in the $3d$ orbital and, in turn, its overlapping with the O $2p$ orbital.

EELS can be used to effectively characterize the nature of bonds in such complex crystal systems like $\text{Y}_2\text{Ti}_2\text{O}_7$ and Y_2TiO_5 , where the metal ions have wide variation in the coordination number, chemical environment and bond lengths. The O K-edge in the EELS corresponds to the transition of electrons from the O 1s to the empty states and the structures at the O K-edge arise from the covalent mixing of the metal (3d) and oxygen (2p) states. Therefore, any change in the chemical environment affects the crystal field splitting and ultimately modifies the pre-edge features in O K-edge.

EELS provides an average measure of the electronic density of states around every atomic species. EELS also provides information about the bond length, oxidation state, and chemical composition, with a spatial resolution down to atomic level in favourable cases[141].

4.4.2. Analysis of O K-edge and Ti L_{23} edge

Figure 4.10(a) shows the O K edge in the EEL spectra of $\text{Y}_2\text{Ti}_2\text{O}_7$, obtained experimentally and from DFT calculation. There are two different chemical environments for the oxygen atoms (O1 and O2) in the $\text{Y}_2\text{Ti}_2\text{O}_7$. The O1 site is surrounded by 2Ti and 2Y atoms whereas O2 site is surrounded by 4Y atoms. The O K edge was calculated separately for O1 and O2 by introducing core hole in 1s orbital of corresponding O atom. It is obvious that both the oxygen atoms contribute to the experimental EELS and the contribution is proportional to the multiplicity factor of the Wyckoff positions. Hence, the resultant spectrum of O K edge for $\text{Y}_2\text{Ti}_2\text{O}_7$ was calculated by superimposing the spectra from O1 and O2 in the ratio of their multiplicity factors (48 for O1 and 8 for O2).

Figure 4.10(b) shows the O K edge in the EEL spectra of Y_2TiO_5 , obtained experimentally and from DFT calculation. Y_2TiO_5 has five different chemical environments for the oxygen atoms, O1, O4 and O5 are surrounded by [4Y], [2Y, 1Ti] and [2Y, 2Ti] atoms respectively; O2 and O3 reside inside two different tetrahedra formed by [3Y, 1Ti]. EELS spectra were calculated for all the oxygen

atoms by introducing core hole in 1s. All these oxygen atoms have the same multiplicity factor of 4. So, the resultant O K-edge of Y_2TiO_5 is calculated by superimposing all the five spectra with equal weights.

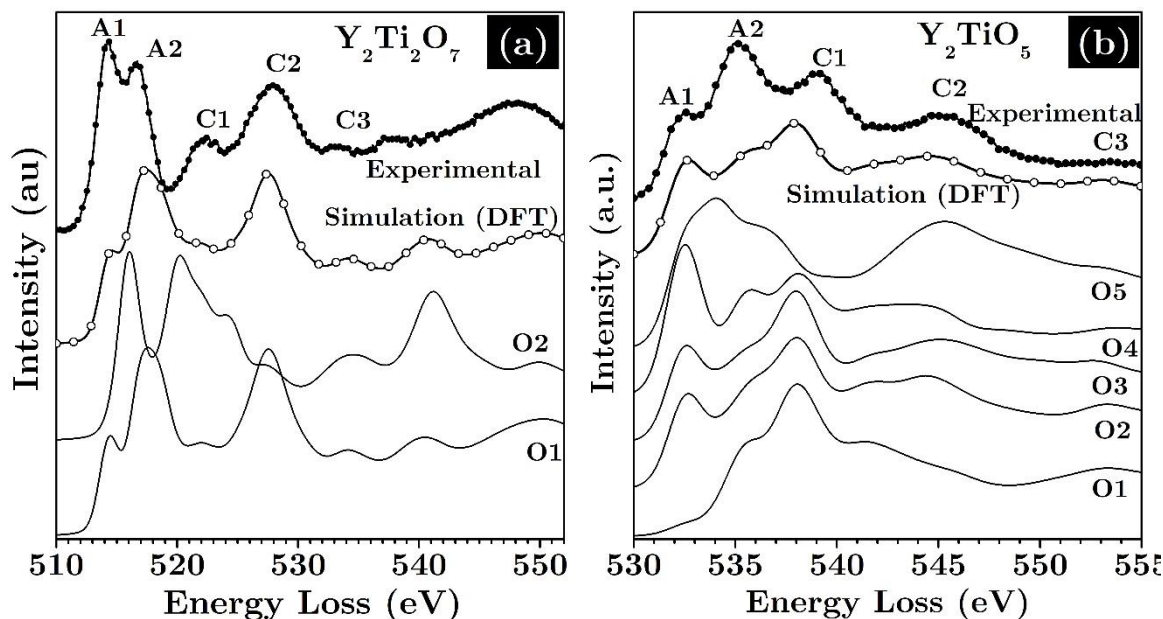


Figure 4.10 Oxygen K edges of (a) $Y_2Ti_2O_7$ and (b) Y_2TiO_5 , from EELS and DFT calculations.

All the calculated spectra are aligned based on the position of the first experimental peak. A smearing value of 0.7 eV is chosen in CASTEP in both the cases, so as to match the smearing due to the experimental energy resolution of 0.7 eV.

For any 3d transition metal oxides, the pre edge features of O K-edge in the EELS arises from the covalent mixing of the metal and the oxygen orbitals. The O K-edge can be divided into two regions: the first region is the pre-edge region with two sharp peaks near threshold and the second region is around 5 to 10 eV above the edge. The peaks in these regions are conventionally named as A1, A2 (pre edge features) and C1, C2 and C3 (second region)[184].

The peaks, A1, A2 (pre edge features) and C1, C2 and C3 (second region), are clearly noticeable in the O K-edge spectra. The pre edge features are related to the 3d states of the metal[185–187] whereas the second region is related to the 4s

and $4p$ bands of the metal[188]. The pre edge features involve the hybridization of O $2p$ orbital with Ti $3d$ orbital and hence involve multiplet effect. The energy splitting between the peaks A1 and A2 for $Y_2Ti_2O_7$ is ~ 2.4 eV and for Y_2TiO_5 it is ~ 2.5 eV. These values reasonably coincide with the crystal-field splitting between the t_{2g} and e_g peak in the corresponding Ti L_{23} edges (see Figure 4.11). The identical energy splitting is one of the evidence for the hybridization[184]. In both $Y_2Ti_2O_7$ and Y_2TiO_5 , the positions of the peaks A1 and A2 closely match with DFT calculations, but the relative intensities do not match. It is because, multiplet effect (peaks A1 and A2) cannot be predicted reliably by DFT. The peaks C1, C2 and C3 are reproduced fairly well in terms of both peak position and intensity.

It may be noted that the peaks A1 and A2 are strong in $Y_2Ti_2O_7$ compared to Y_2TiO_5 , which suggests that the Ti-O bonds in $Y_2Ti_2O_7$ are highly covalent in nature.

Titanium L_{23} edges in the EELS spectra of $Y_2Ti_2O_7$ and Y_2TiO_5 are also calculated using CASTEP. The only difference between O K-edge and Ti L-edge simulations is in using GGA+U (Hubbard-U) approach[189] to describe the localized d -orbital of Ti. An effective U value of 5.25 eV is used, as suggested by Morgan and Watson[190]. The Ti L_{23} -edge was calculated after introducing a core hole in the $2p$ orbital in Ti.

Experimental spectra record transitions involving core states that are split as a result of the spin-orbit interactions. But, the CASTEP implementation lacks spin-orbit terms. So, in order to model the experimental spectra, the calculated spectrum is modified in CASTEP by a simple but slightly approximate method. First an approximate L_3 spectrum is generated by shifting the L_2 spectrum with the experimental value of the spin-orbit splitting of the core states. Then intensity scaling is applied based on the occupancy of the respective electronic shell. The intensity ratios for L edge spectra are 2:4. Finally, the shifted and the scaled spectra are added together[190].

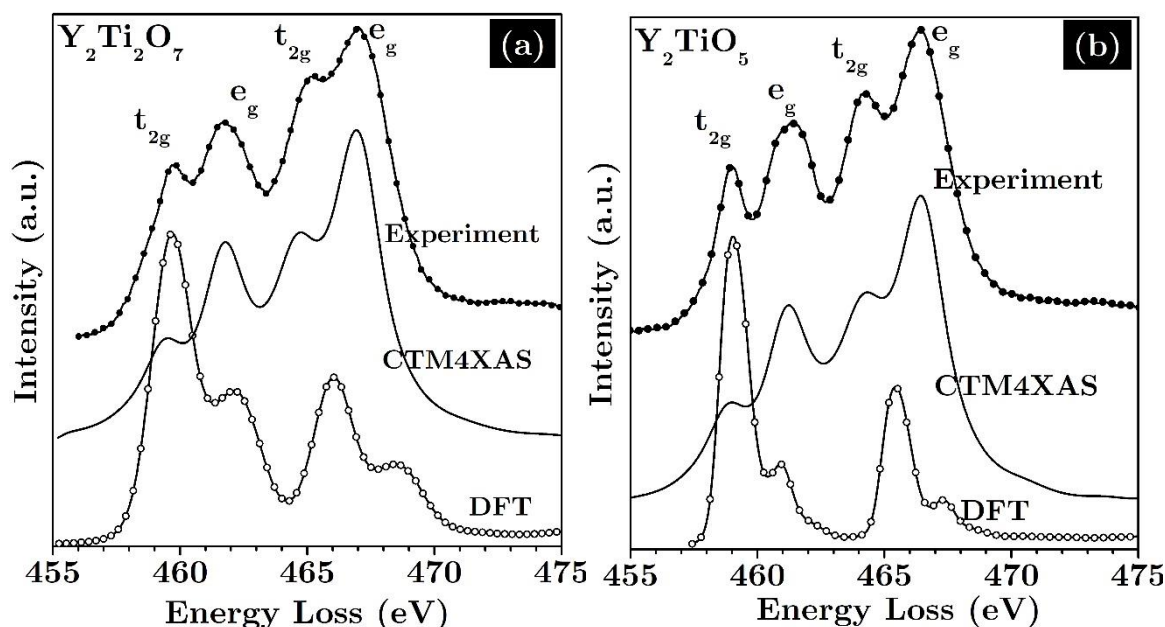


Figure 4.11 Ti L_{23} edges of (a) $Y_2Ti_2O_7$ and (b) Y_2TiO_5 , from EEL spectra, DFT calculations and from CTM4XAS.

Figure 4.11 shows the Ti L_{23} edge in the EEL spectra of $Y_2Ti_2O_7$ and Y_2TiO_5 , obtained experimentally and from DFT calculation. In both $Y_2Ti_2O_7$ and Y_2TiO_5 , the peak positions broadly matches but the intensity ratio ($L_2:L_3$) of DFT results deviate from experiments. The L_2 peak is stronger than L_3 peak in experiments, further e_g peaks are stronger compared to t_{2g} peaks. However, the DFT (CASTEP) calculations show opposite trend in the intensity ratio ($L_2:L_3$) and in the intensity of t_{2g} and e_g . This deviation is observed in both oxides.

Figure 4.11 shows also the spectra calculated using CTM4XAS ($Y_2Ti_2O_7$ and Y_2TiO_5). In $Y_2Ti_2O_7$, Ti atom is octahedrally surrounded by oxygen atoms, and hence in CTM4XAS, O_h (octahedral) symmetry is used in the case of $Y_2Ti_2O_7$. In Y_2TiO_5 , Ti is surrounded by 5 oxygen atoms forming a square pyramid having four-fold rotational symmetry. Hence C_4 (pyramidal) symmetry is used to calculate Ti L_{23} edge in the case of Y_2TiO_5 . In both the oxides, titanium exists in +4 charge state. It must be noted that the experimental Ti L_{23} edges from both the oxides have similar shape. Other parameters in CTM4XAS are tuned to simulate matching spectra. The details of the tuned parameters are as follows.

In the case of $\text{Y}_2\text{Ti}_2\text{O}_7$, the optimized atomic value of 1.0 is assumed for F_{dd} and F_{pd} as suggested in the manual[168] for CTM4XAS. If there is a core hole in $2p$, a value of 0 is suggested for G_{pd} in the manual. But, a value of 1.0 is required for our calculations, to reproduce the experimental intensity ratio ($L_2:L_3$). The energy splitting in experiments is reproduced by providing a $10Dq$ value of 3 eV for initial state and 2 eV for the final state ($10Dq$ denotes the energy separation between the t_{2g} and e_g levels). As far as charge transfer parameters are concerned, only the difference between the Hubbard U (U_{dd}) and the core hole potential (U_{pd}) is important in the analysis of EELS spectra. Here, U_{pd} was taken as 1.0 eV and U_{dd} was taken as 0.0 eV, in order to match the experimental peak intensities. It is suggested that the spin orbit coupling reduction (SO%) value should be always 1. But, $SO\%$ was taken as 0.95 to exactly reproduce the peak separations.

In the case of Y_2TiO_5 also, it is required to use a value of $G_{pd} = 1.0$ to simulate the curve with the same experimental intensity ratio ($L_2:L_3$). The values used for $10Dq$ are the same as in the case of $\text{Y}_2\text{Ti}_2\text{O}_7$, since the experimental peak separations are identical. The symmetry of ligands surrounding Ti is different in the case of Y_2TiO_5 . But the Ti L_{23} edge shape is exactly the same as $\text{Y}_2\text{Ti}_2\text{O}_7$. So, the values of U_{pd} and U_{dd} are required to be tuned. The energy splitting is reproduced by providing a value of 0.5 eV for U_{pd} and 0.0 eV for U_{dd} .

The major problem in DFT calculations is that it could not produce the intensity ratio ($L_2:L_3$) properly. The exact intensity ratio ($L_2:L_3$) is generated by CTM4XAS when $G_{pd}=1$. But, when $G_{pd} = 0$, CTM4XAS reproduces the DFT result which does not match with experiments. .

DFT gives only the ground state configurations properly. However, the calculation of L edges involves the analysis of excited levels. Particularly, the energy separation between t_{2g} and e_g varies before and after the removal of core electron. CTM4XAS can take care of this change in energy split in the initial and the final

configurations. But, DFT calculations cannot include such excited state properties and so deviations are expected.

From the analysis of EEL spectra, it was observed that there is strong overlap between the Ti 3*d* orbital and the O 2*s* orbital in Y₂Ti₂O₇ compared to Y₂TiO₅. This strong overlap is manifested in the intense pre-edge features in the O K-edge in the EEL spectra. Therefore the Ti-O bonds in Y₂Ti₂O₇ are strongly covalent in nature compared to Y₂TiO₅.

4.4.3. Electron density difference and Mulliken charge analysis

In order to get chemical insight, the electron density difference in both the oxides Y₂Ti₂O₇ and Y₂TiO₅ were calculated using DFT and plotted. Figure 4.12(a) shows the 2D plot of differential charge density in Y₂Ti₂O₇ along the plane(101) passing through origin and Figure 4.12(b) shows similar plot in Y₂TiO₅ along the plane (010) passing through $\frac{1}{4}b$ in the *y*-axis. The plots show that the Ti-O bonds are more covalent than Y-O bonds since there is more accumulation of electron density along the Ti-O bonds as compared to the Y-O bonds in both the systems.

All the oxygen atoms bonded to Ti in Y₂Ti₂O₇ are of the same type (O_{48*f*}) and the bond lengths are also the same (1.97 Å), whereas in the case of Y₂TiO₅ the five oxygen atoms have different chemical environments.

The nature of chemical bond may be analysed also using the effective ionic valence, which is defined as the difference between the formal ionic charge and the Mulliken charge on the ionic species. A value of zero for the effective ionic valence indicates a perfectly ionic bond, while values greater than zero indicate increasing levels of covalency[191].

Table 4.1 and Table 4.2 show the formal charge and the calculated Mulliken charge of individual ions in Y₂Ti₂O₇ and Y₂TiO₅; the Mulliken charge values are calculated using CASTEP. The Mulliken charges in Y₂Ti₂O₇ matched with the results in[192]. In Y₂TiO₅, the effective ionic charge on the O atoms (O₂, O₃, O₄ and two O₅ atoms), which are bonded to Ti, shows more covalent nature compared

to O1 which is bonded to Y. Further, the Ti-O bonds in $Y_2Ti_2O_7$ are more covalent compared to those in Y_2TiO_5 , which means the hybridization (of oxygen 2p orbital with titanium 3d orbital) is stronger in $Y_2Ti_2O_7$ than Y_2TiO_5 . These observations comply with our observations from the analysis of O K edges in the EELS spectra.

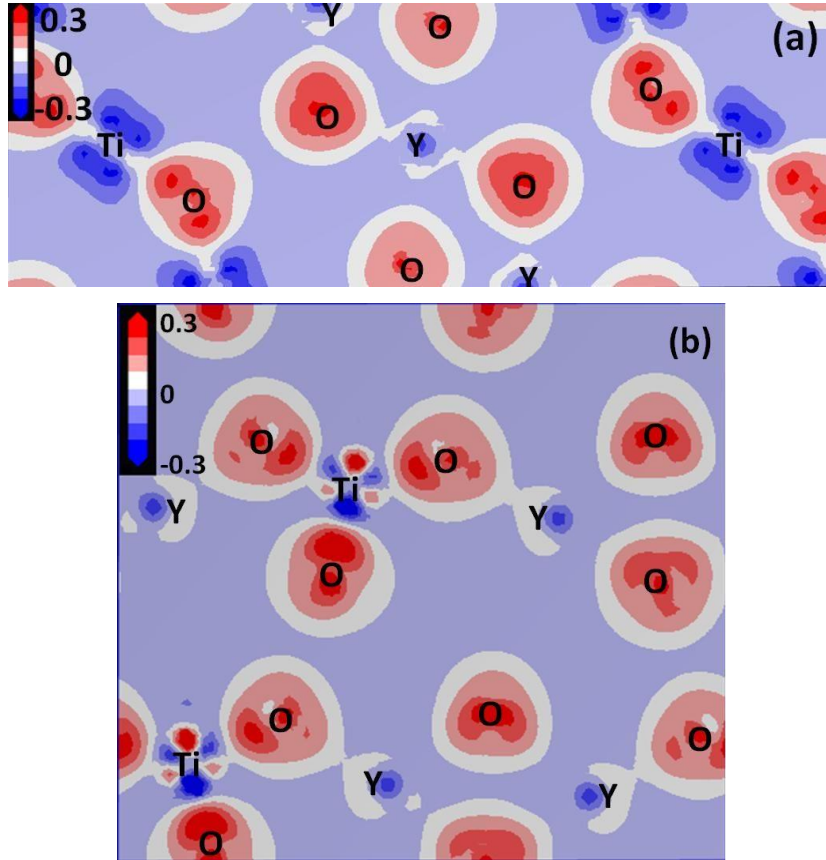


Figure 4.12 2D plot of differential charge density, showing the degree of covalency of the (Ti-O) and (Y-O) bonds in (a) $Y_2Ti_2O_7$ and (b) Y_2TiO_5 . The differential density is plotted along the (101) plane in $Y_2Ti_2O_7$ and along (010) plane in Y_2TiO_5 . The charge density fields are normalized to the number of electrons per \AA^3 .

The analysis of DFT results showed that Ti-O bonds are more covalent in both cases compared to Y-O bonds. Moreover, the Ti-O bonds in $Y_2Ti_2O_7$ is more covalent compared to Y_2TiO_5 . These observations also comply with the EELS results. The results show that $Y_2Ti_2O_7$ is more stable against irradiation and more $Y_2Ti_2O_7$ oxide particles in ODS steel will provide better radiation resistance.

4.5. Discussion

The irradiation stability of the oxide samples $\text{Y}_2\text{Ti}_2\text{O}_7$ and Y_2TiO_5 were studied by characterizing the effects of 70 keV Kr^+ ion irradiation using GIXRD and HRTEM. The GIXRD patterns showed that in the case of $\text{Y}_2\text{Ti}_2\text{O}_7$, the peaks were shifted to higher 2θ values upon irradiation and in the case of Y_2TiO_5 , the peaks have broadened upon irradiation. The HRTEM images showed the presence of irradiation-induced stacking faults in $\text{Y}_2\text{Ti}_2\text{O}_7$, and formation of krypton bubbles in Y_2TiO_5 . The stacking faults could have caused the peak shift in the XRD of $\text{Y}_2\text{Ti}_2\text{O}_7$, and irradiation induced disorder and bubbles, could have caused the broadening of the XRD peaks of Y_2TiO_5 .

It is known that stacking faults would arise from the strain that accumulates in the lattice[193]. In the case of $\text{Y}_2\text{Ti}_2\text{O}_7$ *fcc* pyrochlore system, the ion irradiation induced strain was released by the formation of stable defects namely the stacking faults. The krypton atoms might be accommodated along the stacking faults. In the case of Y_2TiO_5 orthorhombic system, stacking faults are unlikely because it is not a close-packed structure. Hence ion irradiation resulted in the formation of krypton bubbles.

In addition, the analysis of EEL spectra showed that the Ti-O bonds in $\text{Y}_2\text{Ti}_2\text{O}_7$ are strongly covalent in nature compared to Y_2TiO_5 . The DFT results also showed that Ti-O bonds in $\text{Y}_2\text{Ti}_2\text{O}_7$ is more covalent compared to Y_2TiO_5 and that Ti-O bonds are more covalent in both the oxides compared to Y-O bonds.

All these experimental and DFT results suggest that $\text{Y}_2\text{Ti}_2\text{O}_7$ is more stable against irradiation and hence more of $\text{Y}_2\text{Ti}_2\text{O}_7$ oxide nanoparticles in ODS steel may improve the high temperature radiation resistance of the ODS steel.

The present observation is in agreement with the results of molecular dynamics simulations reported by Dholakia *et al.*[194] and the analysis of the structural degree of freedom in these crystal systems carried out by the same authors, following the ideas of Zachariassen[195]. The structural degree of freedom

calculated for $\text{Y}_2\text{Ti}_2\text{O}_7$ and Y_2TiO_5 systems are -6.5 and -5.786 respectively, indicating higher radiation resistance for $\text{Y}_2\text{Ti}_2\text{O}_7$ as compared to Y_2TiO_5 . Further, MD simulations showed that after a displacement cascade event, lesser number of defects survive in $\text{Y}_2\text{Ti}_2\text{O}_7$ as compared to Y_2TiO_5 [194]. Moreover, Y_2TiO_5 is not able to fully recover its initial topology, after the cascade event is complete. Hence the authors suggested $\text{Y}_2\text{Ti}_2\text{O}_7$ has better radiation resistance compared to Y_2TiO_5 .

4.6. Summary and Conclusions

The irradiation stability of the oxide samples $\text{Y}_2\text{Ti}_2\text{O}_7$ and Y_2TiO_5 were studied by characterizing the effects of 70 keV Kr^+ ion irradiations using GIXRD and HRTEM. The metal-oxygen (M-O) bond strengths were compared based on EELS and DFT calculations.

- The irradiation stability of the oxide samples $\text{Y}_2\text{Ti}_2\text{O}_7$ and Y_2TiO_5 were studied by characterizing the effects of 70 keV Kr^+ ion irradiation using GIXRD and HRTEM.
- The GIXRD patterns showed that in the case of $\text{Y}_2\text{Ti}_2\text{O}_7$, the peaks were shifted to higher 2θ values upon irradiation and in the case of Y_2TiO_5 , the peaks have broadened upon irradiation. The HRTEM images showed the presence of irradiation-induced stacking faults in $\text{Y}_2\text{Ti}_2\text{O}_7$, and formation of krypton bubbles in Y_2TiO_5 . The stacking faults could have caused the peak shift in the XRD of $\text{Y}_2\text{Ti}_2\text{O}_7$, and irradiation induced disorder and bubbles, could have caused the broadening of the XRD peaks of Y_2TiO_5 .
- The analysis of EEL spectra showed that the Ti-O bonds in $\text{Y}_2\text{Ti}_2\text{O}_7$ are strongly covalent in nature compared to Y_2TiO_5 . The DFT results also showed that Ti-O bonds in $\text{Y}_2\text{Ti}_2\text{O}_7$ is more covalent compared to Y_2TiO_5 and that Ti-O bonds are more covalent in both the oxides compared to Y-O bonds.

- All these experimental and DFT results suggest that $\text{Y}_2\text{Ti}_2\text{O}_7$ is more stable against irradiation and hence more of $\text{Y}_2\text{Ti}_2\text{O}_7$ oxide nanoparticles in ODS steel may improve the high temperature radiation resistance of the ODS steel.

Chapter 5

Ion irradiation induced crystallization in iron phosphate glass

5.1. Introduction

Iron Phosphate Glass (IPG) has been identified as the matrix which is suitable for the disposal of fast reactor wastes. Higher waste loading capability[196], favourable glass forming characteristics and excellent chemical stability make IPG an attractive matrix for different types of nuclear wastes. Among the various compositions of IPG, the glass with Fe/P ratio of 0.67 (40 mol% Fe₂O₃, 60 mol% P₂O₅) is found to be chemically the most durable[16,127], and this is the composition of the IPG specimen studied in the present thesis.

The central issue, while disposing nuclear waste in glass matrices, is the damage produced by atomic displacements due to α -particles and the recoiling of heavy nuclei resulting from actinide decay. The amorphous nature of glasses provides the interstitial voids needed to retain the radioactive actinides and the durable random-networking of polyhedra helps in reducing their leaching rate. The concern here is whether the ion irradiation affects the relaxation processes in the glass[123], e.g., crystallization of the glass. Therefore, studies on the radiation induced relaxation processes in the wastefoms help to improve the material.

Very few reports are available in the literature on the radiation damage studies on IPG. Sun *et al.*[128] have reported the effects of electron beam and ion beam irradiations on IPG. Electron beam irradiation leads to the formation of Fe-rich and pure P phases whereas the ultra-low energy (3.5 keV Ar⁺) ion irradiation on IPG leads to the formation of Fe/FeO nanoparticles as a result of preferential sputtering during ion irradiation, *i.e.*, P and O were sputtered out at a higher rate than Fe. On the other hand, many reports explain the thermal relaxation processes in IPG. The relaxation processes results in the nucleation of crystalline phases

consisting of Fe, P and O which essentially depends on the composition of IPG. Doupovec *et al.*[197] have reported that the dominant crystalline phases produced by heat treatment of IPG are $\text{Fe}_3(\text{PO}_4)_2$ (660 °C) and FePO_4 (800 °C). Almeida *et al.*[198] have reported that the IPG glass (40 mol% Fe_3O_4 – 60 mol% P_2O_5), after heat treatment at 608 °C and 644 °C results in the formation of the crystalline phases: FePO_4 , $\text{Fe}_3(\text{PO}_4)_2$, $\text{Fe}(\text{PO}_3)_3$, $\text{Fe}(\text{PO}_3)_2$ and $\text{Fe}_7(\text{PO}_4)_6$. Zhang *et al.*[199], found that IPG glass, with Fe/P atomic ratio 0.67, is expected to undergo predominantly an eutectic phase transition at 907 °C and would crystallize into $\text{Fe}_4(\text{P}_2\text{O}_7)_3$ and $\text{Fe}(\text{PO}_3)_3$, or alternatively it may undergo congruent melting and form the crystalline phase $\text{Fe}_4(\text{P}_2\text{O}_7)_3$ at 945 °C. Kitheri *et al.*[200] have heat treated the IPG (Fe/P=0.67) at 1010 K and 1100 K and identified the phases $\text{Fe}_3(\text{P}_2\text{O}_7)_2$, $\text{Fe}_4(\text{P}_2\text{O}_7)_3$ and $\text{Fe}(\text{PO}_3)_3$. In all the reports, the $\text{Fe}^{2+}/\text{Fe}^{3+}$ ratio is found to play a crucial role in the formation of the final phases.

Ion irradiation also induces changes in the charge state of the atomic species in the glass. When the metal ions in the glass formers or the glass stabilizers change their charge state, the glassy nature is disturbed extensively. For instance, Ray *et al.*[16] analysed experimentally the effect of melting temperature and time on the crystallization and particularly on the population of $\text{Fe}^{2+}/\text{Fe}^{3+}$ ions. They have reported that the concentration of Fe^{2+} increases linearly with the melting temperature when observed from 1100 °C upto 1500 °C, and the activation energy for the crystallization process increases monotonically with the increase in the fraction of Fe^{2+} . Iron phosphate glass with the composition of 40 mol% Fe_2O_3 -60 mol% P_2O_5 , has been reported to have different ratios of $\text{Fe}^{2+}/\text{Fe}^{3+}$, by various researchers[125,126,196]. The density of this glass is found to vary depending on the concentration of Fe^{2+} in the glass. The variation in the density has significant effect on the melting temperature of the glass[126]. Hence, it is essential to study the effect of irradiation on $\text{Fe}^{2+}/\text{Fe}^{3+}$ ratio and hence the structure of IPG.

In the present thesis, the stability of IPG, with Fe/P ratio 0.67, against irradiation induced damages, were studied by carrying out ion irradiation experiments and by annealing. The microstructural changes caused by irradiation damage and heat treatment, were studied using transmission electron microscopy (TEM). The changes in the charge state of Fe atom were characterized using XAS and EEL spectroscopy.

5.2. Experimental methods

5.2.1. Synthesis of IPG

Fe₂O₃ (Fischer Scientific, purity: 99.5%) and NH₄H₂PO₄ (ammonium dihydrogen phosphate (ADP)) (Ranboxy, purity: 99%) were mixed keeping Fe/P atomic ratio as 0.67. The mixture was calcined at 673 K in platinum crucible for 1½ hour in order to facilitate the decomposition of ADP. The calcined material was melted and quenched in air at 1423 K to obtain IPG sample. The composition of the glass sample was 40 mol% Fe₂O₃ + 60 mol% P₂O₅ with Fe/P atomic ratio 0.67. The relative abundance of Fe²⁺ and Fe³⁺ ions were 4% and 96% respectively. The synthesis process has been explained in Ref.[118].

5.2.2. Ion irradiation experiments

Ion irradiation experiments were carried out using the 1.7 MV Tandatron Accelerator. 4 MeV O⁺ ions were irradiated on IPG at room temperature, up to ion fluences ranging from 5×10¹³ ions/cm² to 5×10¹⁶ ions/cm². Theoretically, it generates a damage of 0.014 dpa and 14 dpa respectively. Oxygen (self) ion was selected for the irradiation experiments, so as to avoid the effects of impurity atoms. SRIM calculations[201,202]showed that the projected range of 4 MeV O⁺ ions in IPG is 3.8 μm with a straggling of 283 nm. Table 5.1 gives the details of the irradiation experiments on IPG, such as the energy of the ion, its electronic energy loss (S_e), nuclear energy loss (S_n), the total ion fluence and the corresponding damage.

Table 5.1 Details of the irradiation experiments on IPG and the damages for different ion fluences.

Projectile	S_e (eV/nm)	S_n (eV/nm)	Fluence (ions/cm ²)	Damage (dpa)
4 MeV O ⁺ ion	2049	7.47	5×10^{13}	0.014
			5×10^{16}	14.05

The changes in the microstructures of the ion irradiated and the heat treated IPG samples were studied using LIBRA 200FE high resolution transmission electron microscope (HRTEM). Electron diffraction patterns and the high resolution bright field TEM images were used to analyze the changes in the amorphous glassy matrix. EEL spectra also was used to characterize the effects of ion irradiation on the charge state of atoms.

TEM specimen were prepared by scratching the surface of the samples with a scalpel blade. TEM grid was gently rubbed on the surface with a drop of isopropyl alcohol. The sample particles get adsorbed on TEM grid when dried. The grid was then observed under transmission electron microscope.

The changes in the charge state of Fe, *i.e.*, the change in the population of Fe²⁺ and Fe³⁺ ions, were characterized from the X-ray absorption characteristics of the IPG samples. The XANES spectra (X-ray Absorption Near Edge Structures) studies were done in the INDUS-2 synchrotron facility in RRCAT, Indore. The measurements were taken in total electron yield (TEY) mode. This mode probes a depth of ~70 nm in the specimen where the projected range of 4 MeV O⁺ ions is 3.8 μm.

5.3. Results

5.3.1. GIXRD Analysis

The effect of 4 MeV O⁺ ion irradiation in IPG was analyzed using GIXRD patterns recorded from the as-prepared and the 4 MeV O⁺ ion irradiated samples. In GIXRD, the angle of incidence was kept at 3°. Figure 5.1(a) shows the GIXRD

patterns of the as-prepared and the ion irradiated IPG samples. The GIXRD patterns showed that both the samples were amorphous in nature. Both the patterns showed an amorphous hump and there was a very small shift in the peak position: from 24.9° in the as-prepared sample to 25.8° after irradiation with 4 MeV oxygen ions. The amorphous hump correspond to a short range ordering of $\sim 1.8 \text{ \AA}$, which is close to the length of $\text{Fe}^{3+}\text{-O}$ bonds in IPG glass[203]. Actually, this 1.8 \AA maybe the manifestation of different structural motifs involved in IPG within the short range, *i.e.*, the phosphate tetrahedra ($\text{P-O} = \sim 1.5 \text{ \AA}$), the Fe tetrahedra ($\text{Fe-O} = 1.8 \text{ \AA}$) and the Fe octahedra ($\text{Fe-O} = \sim 1.94 \text{ \AA}$). The average effect of all these constituent units is seen as wide hump at 1.8 \AA in the XRD pattern.

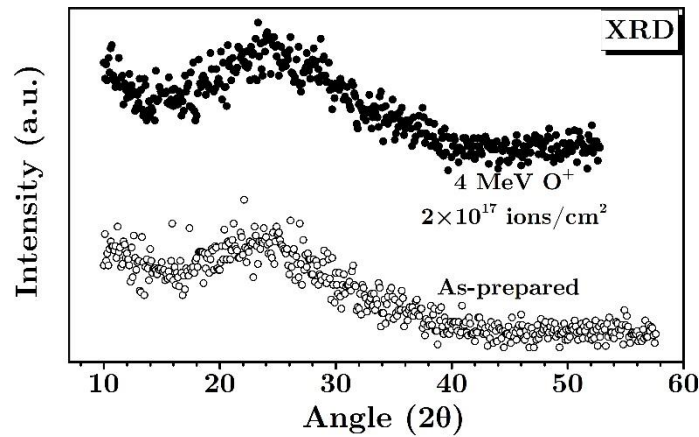


Figure 5.1 XRD patterns of the as-prepared and 4 MeV O^+ ion irradiated IPG samples. The hump corresponding to the amorphous IPG is seen in both cases.

5.3.2. TEM analysis of the microstructural changes

The electron diffraction pattern and the TEM micrographs of the as-prepared IPG sample, are shown in Figure 5.2. Figure 5.2(a) shows the selected area diffraction (SAED) pattern of the as-prepared sample. The SAED pattern did not show any diffraction spots. The SAED pattern was analyzed by plotting the line profile (Figure 5.2(b)), which is the intensity profile averaged across radial lines in the SAED pattern. (The profile was generated using ImageJ software and the 'line profile tool' provided by Carl *et al.*[204]) A broad peak (corresponding to the hollow ring in the SAED pattern, at 7.56 nm^{-1}) was observed in the line profile and the

corresponding d -spacing was 1.3 Å. Absence of any peak in the radial profile also confirmed that the sample was perfectly amorphous. Figure 5.2(c) shows a high resolution TEM image of the sample, which clearly showed the amorphous glassy nature of the sample. Figure 5.2(d) shows low magnification TEM image of the glass.

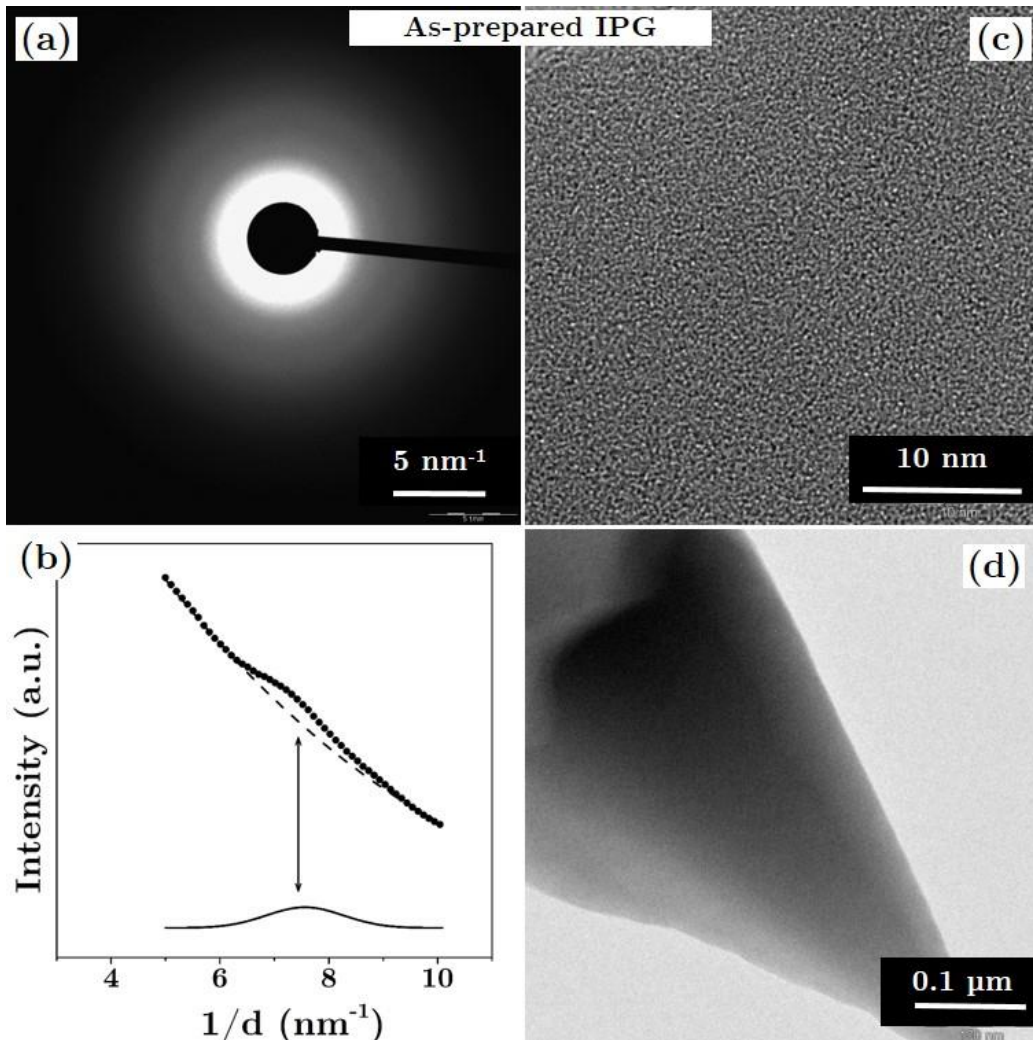


Figure 5.2 TEM micrographs of the as-prepared IPG sample; (a) The SAED pattern (b) The intensity profile averaged across radial lines in the SAED pattern (c) High resolution TEM image and (d) low magnification TEM image. The sample is perfectly amorphous.

Figure 5.3 shows the electron diffraction patterns and the TEM micrographs of the IPG sample irradiated with 4 MeV O^+ ions, upto $5 \times 10^{13} \text{ ions/cm}^2$. Figure 5.3(a) shows the SAED pattern, which contains spotty rings. The spotty rings confirmed the presence of nanocrystalline phases in the glass sample after ion

irradiation. The diffraction rings are signified by the peaks in the intensity profile, shown in Figure 5.3(b). The corresponding d -spacings were compared with all the crystalline phases consisting of the atomic species Fe, P and O, and finally indexed to the crystalline phases $\text{Fe}_4(\text{P}_2\text{O}_7)_3$, $\text{Fe}(\text{PO}_3)_3$ and P_2O_5 (with JCPDS numbers 04-010-4482, 89-8524 and 75-0389 respectively). The summary is given in Table 5.2.

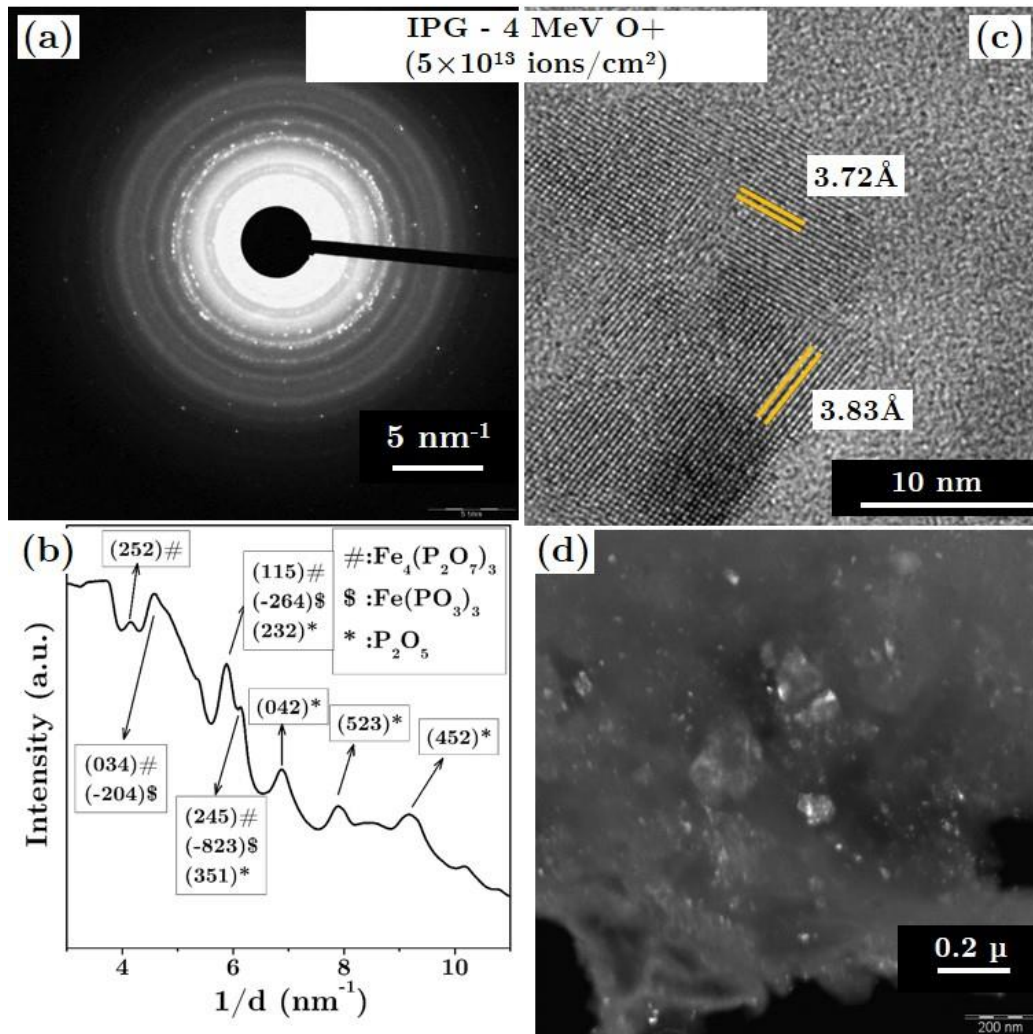


Figure 5.3 TEM micrographs of the IPG sample irradiated with 4 MeV O^+ ions up to the fluence of 5×10^{13} ions/cm²: (a) The SAED pattern containing spotty rings (b) The intensity profile averaged across radial lines of the SAED pattern (c) High resolution TEM image showing lattice fringes and (d) TEM dark field image, where the region with bright contrast corresponds to crystalline phases. Crystalline phases of $\text{Fe}_4(\text{P}_2\text{O}_7)_3$, $\text{Fe}(\text{PO}_3)_3$ and P_2O_5 are identified from the SAED pattern.

Figure 5.3(c) shows the high resolution TEM image, where the lattice fringes were clearly seen in the amorphous background. The d -values of the fringes were found to be 3.72 Å and 3.83 Å and they matched with (122) and (051) planes of $\text{Fe}_4(\text{P}_2\text{O}_7)_3$. TEM dark field image of the sample is shown in Figure 5.3(d), where the regions with bright contrast correspond to crystalline phases, which have nucleated after ion irradiation.

Table 5.2 Comparison of the d -spacing of the heat treated and the ion irradiated IPG samples with ICDD database.

IPG Sample	d values from SAED Å	$\text{Fe}_4(\text{P}_2\text{O}_7)_3$ (04-010-4482) Å (hkl)	$\text{Fe}(\text{PO}_3)_3$ (898524) Å (hkl)	P_2O_5 (750389) Å (hkl)
4 MeV O^+ 5×10^{13} ions/cm ²	2.24	2.25 (034)	2.24(204)	
	1.83	1.83 (115)	1.83(264)	1.61 (232)
	1.61	1.61 (245)	1.61(823)	1.25 (351)
	1.26			1.16 (523)
	1.16			
4 MeV O^+ 5×10^{16} ions/cm ²	2.87	2.89 (212)		
	2.28	2.28 (233)		
	1.96	1.96 (224)		1.95 (231)
	1.67	1.67 (274)		1.67 (240)
	1.40			1.40 (531)
Annealed 900 °C/5 h	1.18			1.18 (160)
	4.77		4.65(202)	
	3.01	3.03 (240)	2.71 (132)	
	2.71	2.72 (043)	2.43 (202)	
	2.44	2.44 (310)	1.92 (332)	
	1.92	1.92 (234)	1.61 (442)	
1.61	1.61 (245)	1.52(594)		
	1.50			

Figure 5.4 explains the microstructural changes in IPG after irradiation with 4 MeV O^+ ions up to a fluence of 5×10^{16} ions/cm². Figure 5.4(a) shows the SAED pattern, which contains spotty rings, confirming the presence of nanocrystalline phases in the sample. The line profile shown in Figure 5.4(b) also confirmed the presence of crystalline phases. The diffraction rings were indexed to $\text{Fe}_4(\text{P}_2\text{O}_7)_3$, and P_2O_5 . The summary is given in Table 5.2. The high resolution TEM image shown in Figure 5.4(c) clearly revealed the lattice fringes of the nanocrystals in the sample.

The lattice fringes had a d -spacing of 2.89 Å, which corresponded to (212) planes of the crystalline phase of $\text{Fe}_4(\text{P}_2\text{O}_7)_3$. Figure 5.4(d) is a bright field TEM image of the irradiated glass, taken at low magnification. While, analyzing the samples under TEM, it was noticed that the amount of the crystalline phase has increased with the ion fluence.

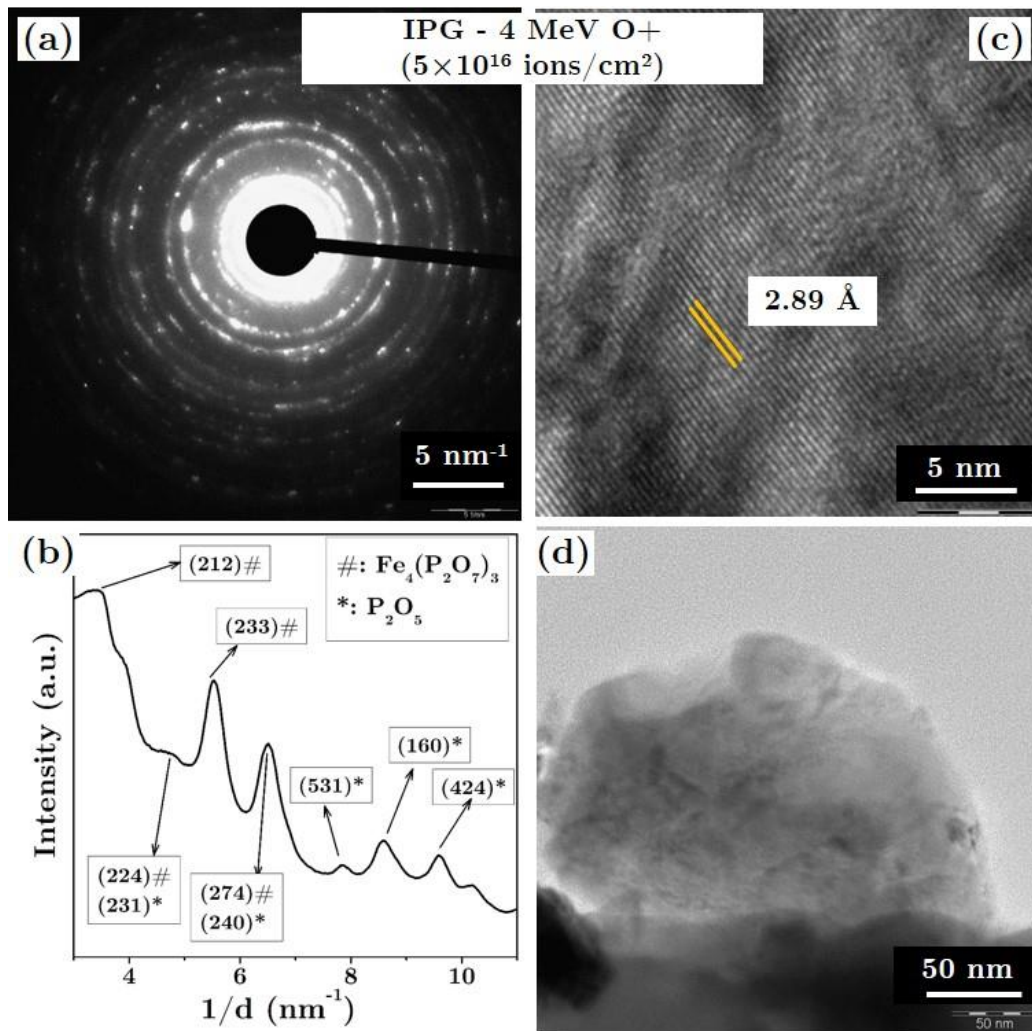


Figure 5.4 TEM micrographs of the IPG sample irradiated with 4 MeV O^+ ions up to the fluence of 5×10^{16} ions/cm²: (a) The SAED pattern containing spotty rings (b) The intensity profile averaged across radial lines in the SAED pattern (c) High resolution TEM image showing lattice fringes and (d) low magnification TEM image. Crystalline phases of $\text{Fe}_4(\text{P}_2\text{O}_7)_3$ and P_2O_5 are identified from the SAED pattern.

The IPG sample, which was annealed at 900 °C for 48 hours, was also characterized using TEM. Figure 5.5 shows a summary of the TEM analysis carried

out on this sample. The SAED pattern shown in Figure 5.5(a) consists of diffraction rings, confirming the nucleation of nanocrystalline phases in the sample upon heat treatment. The diffraction rings were analysed using the average line profile (Figure 5.5(b)) and the phases were indexed to the crystalline phases $\text{Fe}_4(\text{P}_2\text{O}_7)_3$ and $\text{Fe}(\text{PO}_3)_3$. The summary is given in Table 5.2. Figure 5.5(c) shows the high resolution TEM image where the lattice fringes had a d -spacing of 3.01 Å. The value corresponds to the (240) planes of $\text{Fe}_4(\text{P}_2\text{O}_7)_3$.

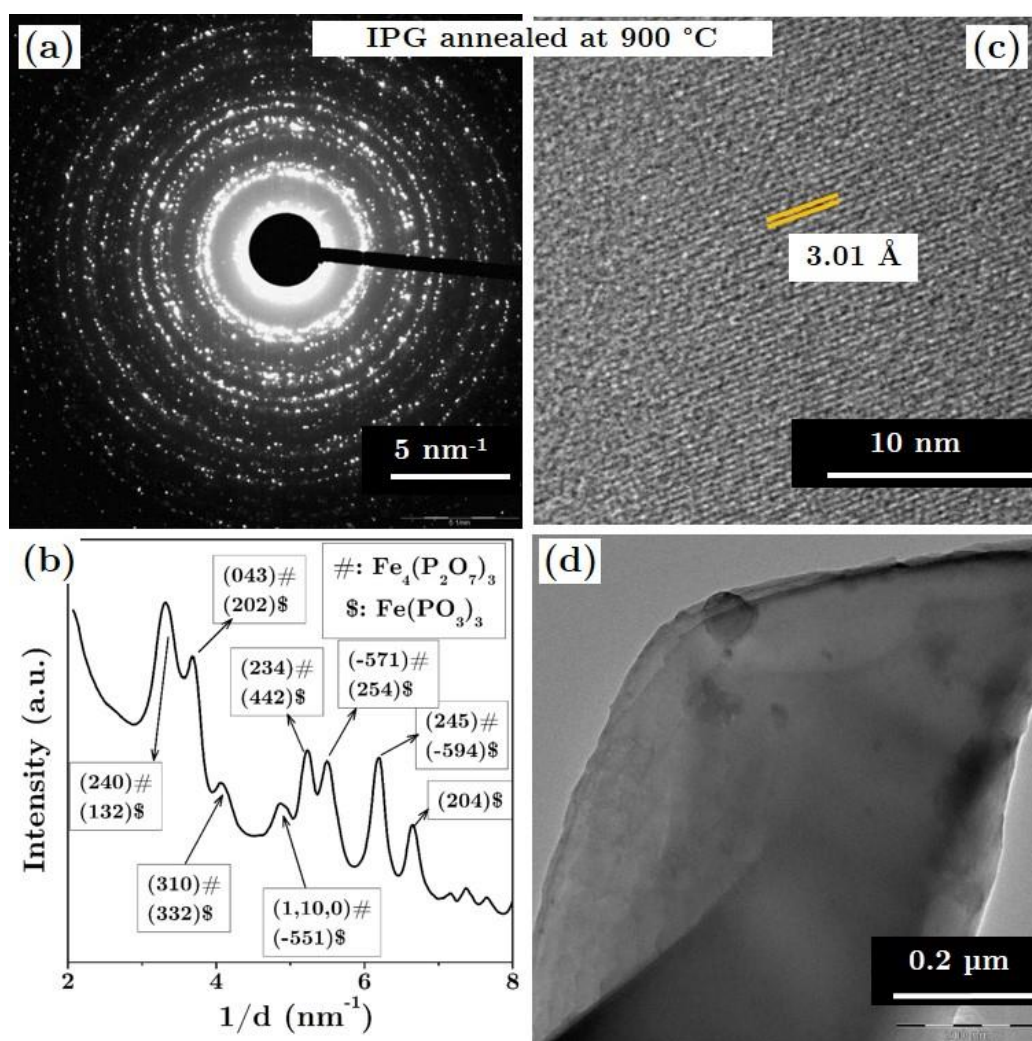


Figure 5.5 TEM micrographs of the IPG sample heat treated at 900 °C for 48h: (a) SAED pattern with spotty rings, (b) The intensity profile averaged across radial lines in the SAED pattern (c) High resolution TEM image showing lattice fringes and (d) low magnification TEM image. Crystalline phases of $\text{Fe}_4(\text{P}_2\text{O}_7)_3$ and $\text{Fe}(\text{PO}_3)_3$ are identified.

The TEM images and electron diffraction patterns were recorded from the region of the sample where the presence of Fe, P and O were confirmed, using electron energy loss spectra. So, the electron diffraction patterns and the HRTEM images confirmed that 4 MeV O^+ ion irradiation and heat treatment (900 °C/48h) has resulted in the nucleation of nanocrystals of $Fe_4(P_2O_7)_3$ and $Fe(PO_3)_3$ and P_2O_5 .

Table 5.2 shows that the ion irradiation upto 5×10^{13} ions/cm² resulted in the formation of nanocrystals of $Fe_4(P_2O_7)_3$, $Fe(PO_3)_3$ and P_2O_5 , whereas for the ion irradiation of upto 5×10^{16} ions/cm², formation of nanocrystals of $Fe_4(P_2O_7)_3$ and P_2O_5 were observed. The annealed sample showed formation of $Fe_4(P_2O_7)_3$ and $Fe(PO_3)_3$ nanocrystals.

5.3.3. Analysis of core-level spectra

X-ray absorption spectra and the EEL spectra from the as-prepared and the 4 MeV O^+ ion irradiated IPG samples were used to study the changes in the charge state of Fe atoms upon ion irradiation. For any 3d transition metal oxides, the pre edge features of O K edge in the EELS and XAS arise from the covalent mixing of the metal and the oxygen orbitals. de Groot *et al.*[188] and Zhang *et al.*[184] have attributed the pre-edge features (A1 and A2) to the 3d states of the transition metals, particularly, to the t_{2g} and e_g band-like states split by the crystal field. The peaks in the second region (5-10 eV above the edge) in O K-edge are named C1, C2, and C3 and are related to the metal 4s and 4p bands[184].

5.3.3.1. O K-edge - XAS and EELS

The O K-edge in the XAS spectra of the as-prepared and the 4 MeV O^+ ion irradiated IPG samples are shown in Figure 5.6(a). The pre-edge features A1 and A2 seen in these spectra show a signature of the change in the charge state of Fe atoms as explained by Colliex *et al.*[205]. These authors have studied the EEL spectra of the characteristic oxygen K-edge in FeO, Fe_3O_4 , α - Fe_2O_3 , and γ - Fe_2O_3 and observed that the relative intensity of the pre-edge peaks (*i.e.* $\frac{A1}{A2}$) in oxygen K-edge depends on the charge state of Fe. The authors found that $\frac{A1}{A2}$ ratio increases

when the charge state of the Fe atom increases from Fe^{2+} (in FeO) to Fe^{3+} (in Fe_2O_3). The electronic configuration of Fe^{2+} is $3d^6$ while that of Fe^{3+} is $3d^5$. So, the pre-edge features of O K-edge reflects the signature of charge state in Fe in both the spectroscopies (EELS and XAS).

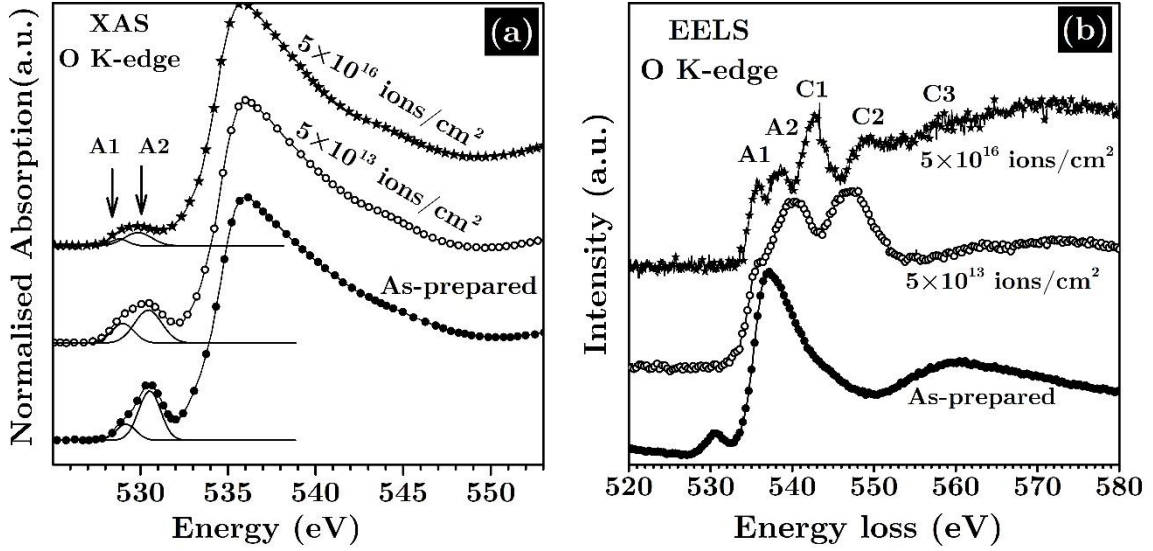


Figure 5.6 O K-edge in the (a) XAS and (b) EEL spectra from the as-prepared and 4 MeV O^+ ions irradiated IPG samples. The relative intensity of A1 peak to A2 (in XAS) decreases with ion fluence.

Table 5.3 summarizes the pre edge features (A1 and A2) of the O K-edge in XAS of the as-prepared and 4 MeV O^+ ion irradiated IPG samples (from Figure 5.6(a)). It should be noted that the intensity ratio of A1 to A2, decreases with the ion fluence, which implies that the concentration of Fe^{3+} reduces as a function of ion fluence.

Table 5.3 The pre edge features of the O K-edge in XAS of the as-prepared and 4 MeV O^+ ion irradiated IPG samples.

Ion Fluence (ions/cm ²)	Peak position(eV)		Normalized Intensity		Intensity Ratio A1/A2
	A1	A2	A1	A2	
0	531.2	532.5	0.66	0.73	0.90
5×10^{13}	531.0	532.5	0.77	0.91	0.85
5×10^{16}	530.8	531.9	0.58	0.92	0.63

The EEL spectra of the as-prepared and the 4 MeV O^+ ion irradiated IPG sample are shown in Figure 5.6(b). Here, the O K-edge of the irradiated samples contains the fine structures (C1, C2 and C3 shown in Figure 5.6(b)) which were absent in the as-prepared IPG sample. The fine structures suggest the nucleation of crystalline phases of Fe-P-O in the sample which was already evident from TEM observations (as reported in previous section 5.3.2.)

There was difference between the fine structures in the XAS and EELS patterns (Figure 5.6). It could be due to the difference in the volume probed by both techniques. The X-rays in XAS probes a volume of $\sim 500\mu\text{m} \times 500\mu\text{m} \times 70\text{nm}$, while the electron beam in EELS probes $\sim 10\mu\text{m} \times 10\mu\text{m} \times 100\text{nm}$. In the present case, XAS probed a large volume where majority of the material remained in amorphous glass phase. So XAS showed the overall changes in the charge state of Fe in the matrix. But, EEL spectra were recorded from the region where nanocrystals have nucleated and hence EELS showed the fine structures corresponding to crystalline phases.

5.3.3.2. Fe L_{23} -edge – XAS and EELS results

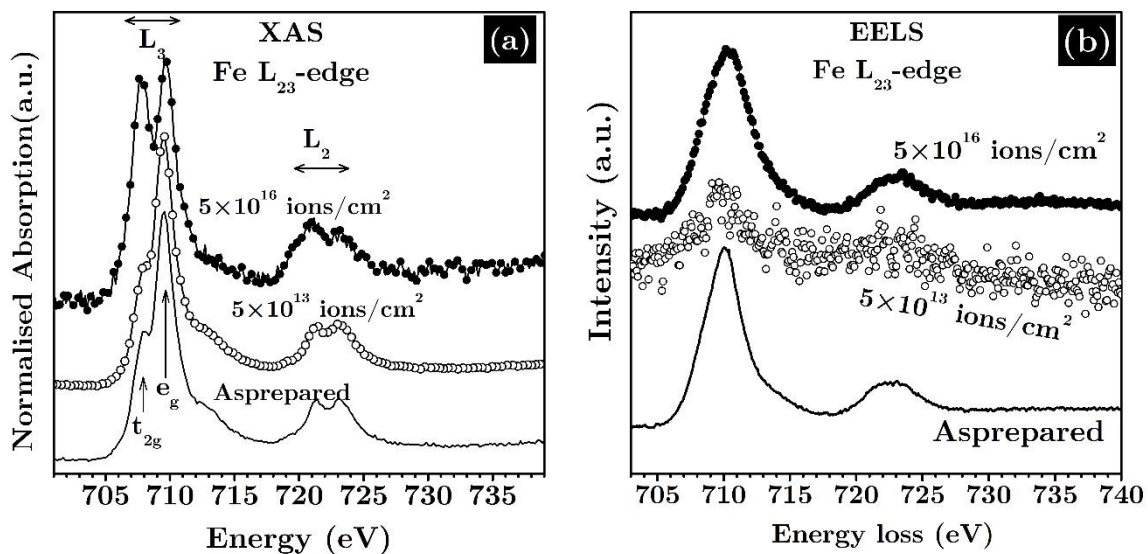


Figure 5.7 Fe L_{23} -edge in the (a) XAS and (b) EEL spectra from the as-prepared and 4 MeV O^+ ions irradiated IPG samples.

The Fe L₂₃-edges in the XAS spectra and the EEL spectra of the as-prepared and the 4 MeV O⁺ ion irradiated IPG samples are shown in Figure 5.7(a) and Figure 5.7(b), respectively. It was observed that the intensity of *t*_{2g} peak, in the L₃ edge, has increased upon ion irradiation (see Figure 5.7(a)).

van Aken *et al.*[206] have shown the usefulness of the core level spectroscopies in determining the oxidation state of iron in minerals. They have studied the Fe L₂₃ edges in the EEL spectra of a range of natural minerals containing iron with different concentrations of Fe²⁺ and Fe³⁺. The authors noticed that the relative concentration of Fe²⁺ and Fe³⁺ leaves a fingerprint in the intensities of *t*_{2g} and *e*_g peaks in the Fe L₃-edge[206]. Particularly, it was observed that the intensity of *t*_{2g} peak, in the L₃ edge, increases when the concentration of Fe²⁺ increases. So in the present case the rise in the intensity of *t*_{2g} peak implies that the concentration of Fe²⁺ has increased in the specimen. The fine structures *t*_{2g} and *e*_g were not resolved in the Fe L₃-edge in the EEL spectra (Figure 5.7(b)) because of the poor energy resolution of the technique.

The energy splitting in between *t*_{2g} and *e*_g (in L₃-edge) was 1.8 eV in the as-prepared sample and it remained almost same (1.7 eV) after irradiation with 4 MeV O⁺ ions up to ion fluence of 5×10¹³ ions/cm². The energy splitting increased to 2.0 eV when the irradiation was continued up to 5×10¹⁶ ions/cm². The split in the L₃-edge is a manifestation of the crystal field splitting which in turn depends on the chemical environment. Hence the variation in the splitting also may be attributed to the variations in the chemical environment due to ion irradiation.

5.4. Discussion

5.4.1. Mechanism of irradiation induced crystallization

The electron diffraction patterns and the HRTEM images confirmed that 4 MeV O⁺ ion irradiation has led to the nucleation of nanocrystals of Fe₄(P₂O₇)₃ and Fe(PO₃)₃ and P₂O₅ in IPG glass.

Crystallization of an amorphous solid is a complex process. In general, the amorphous to crystalline phase transformation is activated by thermal energy of the system. But in the present case, the irradiation induced crystallization could not be explained as a thermally activated process, for the following reasons.

The overall activation energy for the crystallization of the IPG synthesized by Kissinger method is 3.29 eV/atom[207] which corresponds to a very high temperature (of the order of 10^4 K). Similarly, the critical cooling rate for IPG is ~ 10 K/s[196] which is much smaller compared to metallic glasses, where the critical cooling rates are of the order of 10^3 - 10^4 K/s[208]. This implies that the glass phase of IPG is more stable compared to metallic glasses, *i.e.*, large amount of energy will be required to recrystallize IPG. Further, during ion irradiation, which is a non-equilibrium process, the quenching rate of the thermal spike would be so high (10^{12} - 10^{15} K/s) that it becomes difficult to achieve short-range order in the damage cascade[209]. Hence the possibility of spontaneous crystallization also is ruled out in the present case. Heterogeneous nucleation (*i.e.*, the role of impurity atoms in the crystallization process) also is ruled out since the irradiation was done with self-ion (O^+).

Stress driven crystallization has earlier been observed and reported in amorphous materials[210,211]. Shear bands contain homogeneously distributed excess free volume. The excess free volume in amorphous materials is the analogue of vacancies in crystalline materials[52] and the excess free volume controls the diffusion rate in amorphous materials. Excess free volume enhances atomic mobility and leads to increased short-range order and subsequent nucleation of crystalline phase at longer time scales.

In the present irradiation experiments (4 MeV O^+ ions on IPG), SRIM calculations shows that the nuclear energy loss (S_n : ~ 5.5 eV/nm) was negligible compared to the electronic energy loss (S_e : ~ 1.67 keV/nm). So the prominent mode of energy transfer was by electronic energy loss, where, the kinetic energy would be

lost exclusively by means of excitation and ionization of the electronic system of the solid. The rapid energy transfer from the ion irradiation, abnormally excites the atoms along the ion path whereas the surrounding is relatively at low temperature. The pressure wave formed in the wake of the projectile ion can generate an outgoing transient stress and strain. When the stress within an amorphous material increases beyond a critical value, shear bands (*i.e.*, excess free volume) are formed. It enhances atomic mobility and leads to increased short-range order and nucleation of crystalline phase. The amount of stress, introduced in the region around the ion tracks, plays a crucial role in this process. The problem may be quantitatively approached by calculating the local stress around the ion track, induced by single ion σ_{track} , using the visco-elastic model explained Trinkaus *et al.*[53,54] and using the equation in Ref.[52].

$$\sigma_{track} = \frac{(1 + 2\nu)}{2(1 - \nu)(5 - 4\nu)} E \alpha \Delta T^*$$

Eqn. 5.1

Here, E (72.3 GPa) is the Young's modulus of IPG, ν (0.24) is the Poisson ratio, α ($4.1 \times 10^{-5} \text{ K}^{-1}$) is the linear thermal expansion co-efficient of IPG and ΔT^* ($\sim 10^3 \text{ K}$) is the effective temperature of the ion track. (The values are taken from Ref.[212]). From *Eqn. 5.1*, the stress around the ion track is found to be 714 MPa, which is larger than the yield strength of glasses, typically 70 MPa[213], so the surrounding matrix undergoes substantial deformation resulting in shear band formation. Hence it is concluded that nanocrystals could have been nucleated in the vicinity of shear bands, induced during thermal spike process.

5.4.2. Irradiation induced changes in the charge state of Fe

Analysis of the XAS spectra revealed that the concentration of Fe^{2+} has increased and Fe^{3+} has reduced in the glass sample upon 4 MeV O^+ ion irradiation, apart from the formation of crystalline phases of $\text{Fe}_4(\text{P}_2\text{O}_7)_3$ and $\text{Fe}(\text{PO}_3)_3$.

In the present study, the composition of the glass sample was 40 *mol%* Fe_2O_3 + 60 *mol%* P_2O_5 with Fe/P atomic ratio 0.67. Kitheri *et al.*[203] have studied IPG

glass of this composition (using molecular dynamics simulations) and have reported that the IPG consists of glass phase of three systems: $\text{Fe}_4(\text{P}_2\text{O}_7)_3$, $\text{Fe}(\text{PO}_3)_3$ and $\text{Fe}_3(\text{P}_2\text{O}_7)_2$. Out of these three systems, the glass phases of $\text{Fe}_4(\text{P}_2\text{O}_7)_3$ and $\text{Fe}(\text{PO}_3)_3$ contain only Fe^{3+} ions, whereas the glass phase of $\text{Fe}_3(\text{P}_2\text{O}_7)_2$ contains both Fe^{2+} and Fe^{3+} ions.

So the rise in the amount of Fe^{2+} upon irradiation implies that glass phase of the system, $\text{Fe}_3(\text{P}_2\text{O}_7)_2$, has increased in the matrix upon irradiation, along with the nucleation of the crystalline phases of $\text{Fe}_4(\text{P}_2\text{O}_7)_3$ and $\text{Fe}(\text{PO}_3)_3$, which contain only Fe^{3+} ions. The increase in Fe^{2+} in the glass matrix could be due to the formation of crystalline phases containing Fe^{3+} .

The changes in the concentrations of Fe^{2+} and Fe^{3+} is known to influence many characteristics of the IPG glass. Huang *et al.*[214] have showed that the increase in Fe^{2+} increases the viscosity of IPG, which in turn increases the glass forming ability.

5.5. Summary and conclusion

The effects of ion irradiation (4 MeV O^+ ions, fluences: 5×10^{13} and 5×10^{16} ions/cm²) on iron phosphate glass were studied using transmission electron microscopy, and core level spectroscopy techniques.

- The electron diffraction patterns and HRTEM images revealed that IPG crystallizes upon ion irradiation. The crystalline phases nucleated during the above processes were identified as $\text{Fe}_4(\text{P}_2\text{O}_7)_3$, $\text{Fe}(\text{PO}_3)_3$ and P_2O_5 .
- The irradiation induced crystallization was explained based on stress driven crystallization mechanism. The stress around the ion track was ~ 700 MPa, which was larger than the typical yield strength of the glass (~ 70 MPa). Hence, the surrounding matrix undergoes substantial deformation resulting in the formation of shear bands. Nanocrystals could have been nucleated in the vicinity of shear bands induced during thermal spike process.

- The analysis of core level spectra (XAS and EELS) showed that the concentration of Fe^{2+} , on the whole, has increased and Fe^{3+} has reduced in IPG glass upon ion irradiation. The rise in the amount of Fe^{2+} implies that glass phase of the system, $\text{Fe}_3(\text{P}_2\text{O}_7)_2$, has increased in the matrix upon irradiation, along with the nucleation of the crystalline phases of $\text{Fe}_4(\text{P}_2\text{O}_7)_3$ and $\text{Fe}(\text{PO}_3)_3$, which contain only Fe^{3+} ions. The increase in Fe^{2+} in the glass matrix could be due to the formation of crystalline phases containing Fe^{3+} . The rise in the population of Fe^{2+} increases the viscosity of IPG, which in turn increases the glass forming ability.

Chapter 6

Summary and scope for future work

The thesis deals with radiation effects in oxides used in nuclear applications. Ion irradiation were carried out for creating damage and the effect of damage was studied by HRTEM, GIXRD and core level spectroscopy techniques such as EELS and XAS. Further DFT calculations were carried out to understand the experimental results.

Oxide materials find applications throughout the nuclear fuel cycle, from actinide-bearing ores and commercial reactor fuels to wasteforms for radionuclide disposal. Many of the critically important materials used in the nuclear industry are oxide based ceramics, like the oxide fuel materials (e.g. urania, thoria), the oxide nanodispersoids (e.g. yttrium titanates in ferritic steel) used for strengthening the metallic structural materials and the glasses used for the disposal of nuclear wastes (e.g. borosilicate glass, iron phosphate glass).

The present thesis deals with the studies on the radiation stability of oxide ceramics: (i) thorium dioxide or thoria (ThO_2), a nuclear fuel material, (ii) yttrium titanates ($\text{Y}_2\text{Ti}_2\text{O}_7$ and Y_2TiO_5), the oxide-dispersoids used for strengthening the structural material, (iii) Iron Phosphate Glass (IPG), the material proposed for the disposal of high level nuclear waste from the fast reactors.

Aggregation and ordering of helium in thoria:

The aggregation and ordering of helium was studied by irradiating thoria with 100 keV He^+ ions and characterizing the effects using GIXRD and TEM.

- GIXRD and TEM analysis showed that there is a lattice expansion of 1.07% in isolated nanometric regions of the sample. The GIXRD patterns of 4 MeV Si^+ ion irradiated sample proved that damage (point defects and defect clusters) alone will not produce such a large lattice expansion.

- DFT calculations showed that helium prefers Th-vacancy site in the defective thoria system. DFT calculations also showed that helium energetically prefers to aggregate in the octahedral interstitial sites of the *fcc* lattice of thoria. The aggregation and ordering of helium atoms in the octahedral interstitial sites of thoria results in a lattice expansion of 1.25%.
- The experiments and calculations confirm that the lattice expansion is due to the aggregation and ordering of helium atoms in nanometric regions of thoria.

Radiation stability of yttrium titanates:

The irradiation stability of the oxide samples $\text{Y}_2\text{Ti}_2\text{O}_7$ and Y_2TiO_5 were studied by characterizing the effects of 70 keV Kr^+ ion irradiations using GIXRD and HRTEM. The metal-oxygen (M-O) bond strengths were compared based on EELS and DFT calculations.

- The irradiation stability of the oxide samples $\text{Y}_2\text{Ti}_2\text{O}_7$ and Y_2TiO_5 were studied by characterizing the effects of 70 keV Kr^+ ion irradiation using GIXRD and HRTEM.
- The GIXRD patterns showed that in the case of $\text{Y}_2\text{Ti}_2\text{O}_7$, the peaks were shifted to higher 2θ values upon irradiation and in the case of Y_2TiO_5 , the peaks have broadened upon irradiation. The HRTEM images showed the presence of irradiation-induced stacking faults in $\text{Y}_2\text{Ti}_2\text{O}_7$, and formation of krypton bubbles in Y_2TiO_5 . The stacking faults could have caused the peak shift in the XRD of $\text{Y}_2\text{Ti}_2\text{O}_7$, and irradiation induced disorder and bubbles, could have caused the broadening of the XRD peaks of Y_2TiO_5 .
- The analysis of EEL spectra showed that the Ti-O bonds in $\text{Y}_2\text{Ti}_2\text{O}_7$ are strongly covalent in nature compared to Y_2TiO_5 . The DFT results also showed that Ti-O bonds in $\text{Y}_2\text{Ti}_2\text{O}_7$ is more covalent compared to Y_2TiO_5 and that Ti-O bonds are more covalent in both the oxides compared to Y-O bonds.

- All these experimental and DFT results suggest that $\text{Y}_2\text{Ti}_2\text{O}_7$ is more stable against irradiation and hence more of $\text{Y}_2\text{Ti}_2\text{O}_7$ oxide nanoparticles in ODS steel may improve the high temperature radiation resistance of the ODS steel.

Ion irradiation induced crystallization in iron phosphate glass:

The effects of ion irradiation (4 MeV O^+ ions, fluences: 5×10^{13} and 5×10^{16} ions/cm²) on iron phosphate glass were studied using transmission electron microscopy, and core level spectroscopy techniques.

- The electron diffraction patterns and HRTEM images revealed that IPG crystallizes upon ion irradiation. The crystalline phases nucleated during the above processes were identified as $\text{Fe}_4(\text{P}_2\text{O}_7)_3$, $\text{Fe}(\text{PO}_3)_3$ and P_2O_5 .
- The irradiation induced crystallization was explained based on stress driven crystallization mechanism. The stress around the ion track was ~ 700 MPa, which was larger than the typical yield strength of the glass (~ 70 MPa). Hence, the surrounding matrix undergoes substantial deformation resulting in the formation of shear bands. Nanocrystals could have been nucleated in the vicinity of shear bands induced during thermal spike process.
- The analysis of core level spectra (XAS and EELS) showed that the concentration of Fe^{2+} , on the whole, has increased and Fe^{3+} has reduced in IPG glass upon ion irradiation. The rise in the amount of Fe^{2+} implies that glass phase of the system, $\text{Fe}_3(\text{P}_2\text{O}_7)_2$, has increased in the matrix upon irradiation, along with the nucleation of the crystalline phases of $\text{Fe}_4(\text{P}_2\text{O}_7)_3$ and $\text{Fe}(\text{PO}_3)_3$, which contain only Fe^{3+} ions. The increase in Fe^{2+} in the glass matrix could be due to the formation of crystalline phases containing Fe^{3+} . The rise in the population of Fe^{2+} increases the viscosity of IPG, which in turn increases the glass forming ability.

Scope for future work:

- In the thesis it was observed that $Y_2Ti_2O_7$ and Y_2TiO_5 did not amorphize at room temperature at a high dose rate of ~ 1 dpa/s. It will be worth studying the amorphization behaviour by varying the dose rate and temperature of irradiation.
- The aggregation and ordering of helium atoms in the octahedral interstitial sites of thoria was observed in this thesis. It will be interesting to study aggregation and ordering behaviour of other inert gases like Ar, Xe, etc. in thoria by DFT based calculations and ion irradiation.
- It was observed that ion irradiation has resulted in restructuring of the grains in the case of thoria. So, in-situ irradiation and imaging experiments on thoria would provide more information on grain restructuring and on the behaviour of inert gases inside thoria.
- When the irradiated IPG samples were investigated under SEM, it was noticed that ion irradiation has distorted the surface and introduced ripples on the surface of IPG, especially the ripple patterns appears at some particular ion fluence and disappeared on further irradiation. So in-situ irradiation and imaging experiments on IPG would provide much more quantitative information on undulation and instability. In addition, in-situ irradiation cum resistivity measurement on IPG surface can be used to study the mechanism of nucleation and growth of crystalline phases.

References

- [1] Tracy C.L., Lang M., Zhang F., Park S., Palomares R.I., Ewing R.C., Review of recent experimental results on the behavior of actinide-bearing oxides and related materials in extreme environments, *Prog. Nucl. Energy*, (2018), **104**, 342–358
- [2] Lee W.E., Gilbert M., Murphy S.T., Grimes R.W., Opportunities for Advanced Ceramics and Composites in the Nuclear Sector, *J. Am. Ceram. Soc.*, (2013), **96**, 2005–2030
- [3] Devanathan R., Radiation damage evolution in ceramics, *Nucl. Inst. Methods Phys. Res. B*, (2009), **267**, 3017–3021
- [4] Birss I.R., Helium production in reactor materials, *J. Nucl. Mater.*, (1970), **34**, 241–259
- [5] Govindan Kutty T.R., Banerjee J., Arun Kumar, Thoria-based Nuclear Fuels, *Springer, London*, (2013)
- [6] Maeda K., Katsuyama K., Asaga T., Fission gas release in FBR MOX fuel irradiated to high burnup, *J. Nucl. Mater.*, (2005), **346**, 244–252
- [7] Hu S., Henager C.H., Heinisch H.L., Stan M., Baskes M.I., Valone S.M., Phase-field modeling of gas bubbles and thermal conductivity evolution in nuclear fuels, *J. Nucl. Mater.*, (2009), **392**, 292–300
- [8] Olander D., Nuclear fuels – Present and future, *J. Nucl. Mater.*, (2009), **389**, 1–22
- [9] Lemehov S.E., Sobolev V., Van Uffelen P., Modelling thermal conductivity and self-irradiation effects in mixed oxide fuels, *J. Nucl. Mater.*, (2003), **320**, 66–76
- [10] Simeone D., Costantini J.M., Luneville L., Desgranges L., Trocellier P., Garcia P., Characterization of radiation damage in ceramics: Old challenge new issues?, *J. Mater. Res.*, (2015), **30**, 1495–1515
- [11] Matzke H., Radiation damage in crystalline insulators, oxides and ceramic nuclear fuels, *Radiat. Eff. Defects Solids*, (1982), **64**, 3–33
- [12] Olander D.R., Fundamental aspects of nuclear reactor fuel elements, *California Univ., Berkeley (USA).*, (1976)
- [13] Sakasegawa H., Chaffron L., Legendre F., Boulanger L., Cozzika T., Brocq M., de Carlan Y., Correlation between chemical composition and size of very small oxide particles in the MA957 ODS ferritic alloy, *J. Nucl. Mater.*, (2009), **384**, 115–118
- [14] Donald I.W., Metcalfe B.L., Taylor R.N.J., Review The immobilization of high level radioactive wastes using ceramics and glasses, *J. Mater. Sci.*, (1997), **32**, 5851–5887
- [15] Sales B.C., White C.W., Boatner L.A., A comparison of the corrosion characteristics of synthetic monazite and borosilicate glass containing simulated nuclear defense waste, *Nucl. Chem. Waste Manag.*, (1983), **4**, 281–289

- [16] Ray C.S., Fang X., Karabulut M., Marasinghe G.K., Day D.E., Effect of melting temperature and time on iron valence and crystallization of iron phosphate glasses, *J. Non. Cryst. Solids*, (1999), **249**, 1–16
- [17] Weber W.J., Ewing R.C., Catlow C.R.A., de la Rubia T.D., Hobbs L.W., Kinoshita C., Matzke H., Motta A.T., Nastasi M., Salje E.K.H., Vance E.R., Zinkle S.J., Radiation effects in crystalline ceramics for the immobilization of high-level nuclear waste and plutonium, *J. Mater. Res.*, (1998), **13**, 1434–1484
- [18] Sickafus K.E., Grimes R.W., Valdez J.A., Cleave A., Tang M., Ishimaru M., Corish S.M., Stanek C.R., Uberuaga B.P., Radiation-induced amorphization resistance and radiation tolerance in structurally related oxides, *Nat. Mater.*, (2007), **6**, 217–223
- [19] Wang S.X., Begg B.D., Wang L.M., Ewing R.C., Weber W.J., Govidan Kutty K. V., Radiation stability of gadolinium zirconate: A waste form for plutonium disposition, *J. Mater. Res.*, (1999), **14**, 4470–4473
- [20] Sickafus K.E., Radiation Tolerance of Complex Oxides, *Science*, (2000), **289**, 748–751
- [21] Ewing R.C., Weber W.J., Lian J., Nuclear waste disposal-pyrochlore (A₂B₂O₇): Nuclear waste form for the immobilization of plutonium and “minor” actinides, *J. Appl. Phys.*, (2004), **95**, 5949–5971
- [22] Nastasi M., Michael N., Mayer J., Hirvonen J.K., James M., Press C.U., Clarke D.R., Suresh S., Ward I.M., Ion-Solid Interactions: Fundamentals and Applications, *Cambridge University Press*, (1996)
- [23] Segre E., Staub H., Bethe H.A., Ashkin J., Experimental nuclear physics. Volume-I, *John Wiley & Sons; Chapman & Hall, New York; London*, (1953)
- [24] Lindhard J., Scharff M., Energy Dissipation by Ions in the keV Region, *Phys. Rev.*, (1961), **124**, 128–130
- [25] Gary Was S., Fundamentals of Radiation Materials Science, *Springer Berlin Heidelberg, Berlin, Heidelberg*, (2007)
- [26] Ziegler J.F., Ziegler M.D., Biersack J.P., SRIM - The stopping and range of ions in matter (2010), *Nucl. Inst. Methods Phys. Res. B*, (2010), **268**, 1818–1823
- [27] Sigmund P., Theory of sputtering. I. Sputtering yield of amorphous and polycrystalline targets, *Phys. Rev.*, (1969), **184**, 383–416
- [28] Ullmaier H., Schilling W., Radiation damage in metallic reactor materials, *IAEA, International Atomic Energy Agency (IAEA)*, (1980)
- [29] Kinchin G.H., Pease R.S., The Displacement of Atoms in Solids by Radiation, *Reports Prog. Phys.*, (1955), **18**, 301
- [30] Amirthapandian S., Panigrahi B.K., Rajagopalan S., Gupta A., Nair K.G.M., Tyagi A.K., Narayanasamy A., Evidence for complete ion-beam mixing in thermally immiscible Fe/Ag multilayers from conversion electron Mössbauer spectroscopy, *Phys. Rev. B*, (2004), **69**, 165411

- [31] Amirthapandian S., Panigrahi B.K., Srivastava A.K., Dhara S., Gupta A., Sastry V.S., Nandedkar R. V., Nair K.G.M., Narayanasamy A., Ion-beam mixing in an immiscible Fe/Ag multilayer film, *J. Appl. Phys.*, (2004), **95**, 5295–5300
- [32] Praver S., Kalish R., Ion-beam-induced transformation of diamond, *Phys. Rev. B*, (1995), **51**, 15711–15722
- [33] Avasthi D.K., Some interesting aspects of swift heavy ions in materials science, *Curr. Sci.*, (2000), **78**, 1297–1303
- [34] Park S., Lang M., Tracy C.L., Zhang J., Zhang F., Trautmann C., Rodriguez M.D., Kluth P., Ewing R.C., Response of Gd₂Ti₂O₇ and La₂Ti₂O₇ to swift-heavy ion irradiation and annealing, *Acta Mater.*, (2015), **93**, 1–11
- [35] Fleischer R.L., Price P.B., Walker R.M., Ion Explosion Spike Mechanism for Formation of Charged-Particle Tracks in Solids, *J. Appl. Phys.*, (1965), **36**, 3645–3652
- [36] Wang Z.G., Dufour C., Paumier E., Toulemonde M., The Se sensitivity of metals under swift-heavy-ion irradiation: a transient thermal process, *J. Phys. Condens. Matter*, (1994), **6**, 6733–6750
- [37] M. Toulemonde, Ch. Dufour A.M. et al., Transitional thermal processes during heavy ion irradiation of crystalline inorganic insulators, *Nucl. Inst. Methods Phys. Res. B*, (2000), **167**, 903
- [38] Szenes G., General features of latent track formation in magnetic insulators irradiated with swift heavy ions, *Phys. Rev. B*, (1995), **51**, 8026–8029
- [39] Klaumünzer S., Hou M., Schumacher G., Coulomb Explosions in a Metallic Glass Due to the Passage of Fast Heavy Ions?, *Phys. Rev. Lett.*, (1986), **57**, 850–853
- [40] Klaumünzer S., Schumacher G., Dramatic Growth of Glassy Pd₈₀Si₂₀ during Heavy-Ion Irradiation, *Phys. Rev. Lett.*, (1983), **51**, 1987–1990
- [41] Balaji S., Sruthi Mohan, Amirthapandian S., Chinnathambi S., David C., Panigrahi B.K., Ion irradiation studies on the void swelling behavior of a titanium modified D9 alloy, *J. Nucl. Mater.*, (2015), **467**, 368–372
- [42] Nastasi M., Mayer J.W., Thermodynamics and kinetics of phase transformations induced by ion irradiation, *Mater. Sci. Reports*, (1991), **6**, 1–51
- [43] Pelaz L., Marqués L.A., Barbolla J., Ion-beam-induced amorphization and recrystallization in silicon, *J. Appl. Phys.*, (2004), **96**, 5947–5976
- [44] Wang L.M., Ewing R.C., Ion-Beam-Induced Amorphization of Complex Ceramic Materials—Minerals, *MRS Bull.*, (1992), **17**, 38–44
- [45] Zhuang Y.X., Jiang J.Z., Zhou T.J., Rasmussen H., Gerward L., Mezouar M., Crichton W., Inoue A., Pressure effects on Al₈₉La₆Ni₅ amorphous alloy crystallization, *Appl. Phys. Lett.*, (2000), **77**, 4133–4135

- [46] Ye F., Lu K., Pressure effect on crystallization kinetics of an Al–La–Ni amorphous alloy, *Acta Mater.*, (1999), **47**, 2449–2454
- [47] Kim J.J., Choi Y., Suresh S., Argon A.S., Nanocrystallization during nanoindentation of a bulk amorphous metal alloy at room temperature, *Science*, (2002), **295**, 654–657
- [48] He J., Kaban I., Mattern N., Song K., Sun B., Zhao J., Kim D.H., Eckert J., Greer A.L., Local microstructure evolution at shear bands in metallic glasses with nanoscale phase separation, *Sci. Rep.*, (2016), **6**, 25832
- [49] Greer A.L., Cheng Y.Q., Ma E., Shear bands in metallic glasses, *Mater. Sci. Eng. R*, (2013), **74**, 71–132
- [50] Maaß R., Löffler J.F., Shear-Band Dynamics in Metallic Glasses, *Adv. Funct. Mater.*, (2015), **25**, 2353–2368
- [51] Chen H., He Y., Shiflet G.J., Poon S.J., Deformation-induced nanocrystal formation in shear bands of amorphous alloys, *Nature*, (1994), **367**, 541–543
- [52] Rizza G., Dunlop A., Kopcewicz M., Deformation bands in metallic glasses induced by swift heavy ions, *Nucl. Inst. Methods Phys. Res. B*, (2006), **245**, 130–132
- [53] Trinkaus H., Local stress relaxation in thermal spikes as a possible cause for creep and macroscopic stress relaxation of amorphous solids under irradiation, *J. Nucl. Mater.*, (1995), **223**, 196–201
- [54] Trinkaus H., Ryazanov A.I., Viscoelastic Model for the Plastic Flow of Amorphous Solids under Energetic Ion Bombardment, *Phys. Rev. Lett.*, (1995), **74**, 5072–5075
- [55] Dammak H., Barbu A., Dunlop A., Lesueur D., Lorenzelli N., $\alpha \rightarrow \omega$ phase transformation induced in titanium during ion irradiations in the electronic slowing-down regime, *Philos. Mag. Lett.*, (1993), **67**, 253–259
- [56] Hémon S., Chailley V., Dooryhée E., Dufour C., Gourbilleau F., Levesque F., Paumier E., Phase transformation of polycrystalline Y₂O₃ under irradiation with swift heavy ions, *Nucl. Inst. Methods Phys. Res. B*, (1997), **122**, 563–565
- [57] Tiwari U., Sen N., Bandyopadhyay A.K., Kanjilal D., Sen P., Phase Transition in a Perovskite Superconductor by Radiation-Induced Lattice Excitations, *Europhys. Lett.*, (1994), **25**, 705–710
- [58] Benyagoub A., Mechanism of the monoclinic-to-tetragonal phase transition induced in zirconia and hafnia by swift heavy ions, *Phys. Rev. B*, (2005), **72**, 21–24
- [59] Benyagoub A., Evidence of an ion-beam induced crystalline-to-crystalline phase transformation in hafnia, *Eur. Phys. J. B*, (2003), **34**, 395–398
- [60] Schuster B., Lang M., Klein R., Trautmann C., Neumann R., Benyagoub A., Structural phase transition induced by swift heavy ion irradiation at high-pressure, *Nucl. Inst. Methods Phys. Res. B*, (2009), **267**, 964–968

- [61] Sickafus K.E., Matzke H., Hartmann T., Yasuda K., Valdez J.A., Chodak P., Nastasi M., Verrall R.A., Radiation damage effects in zirconia, *J. Nucl. Mater.*, (1999), **274**, 66–77
- [62] Benyagoub A., Levesque F., Couvreur F., Gibert-Mougel C., Dufour C., Paumier E., Evidence of a phase transition induced in zirconia by high energy heavy ions, *Appl. Phys. Lett.*, (2000), **77**, 3197–3199
- [63] Benyagoub A., Phase transformations in oxides induced by swift heavy ions, *Nucl. Inst. Methods Phys. Res. B*, (2006), **245**, 225–230
- [64] Donnelly S.E., The density and pressure of helium in bubbles in implanted metals: A critical review, *Radiat. Eff.*, (1985), **90**, 1–47
- [65] Luklinska Z.H., von Bradsky G., Goodhew P.J., Helium bubble growth in ferritic stainless steel, *J. Nucl. Mater.*, (1985), **135**, 206–214
- [66] Tyler S.K., Goodhew P.J., Irregular Helium Bubbles In Niobium Alloys, *J. Microsc.*, (1979), **116**, 55–63
- [67] Xiao W., Zhang X., Geng W.T., Lu G., Helium bubble nucleation and growth in α -Fe: insights from first-principles simulations., *J. Phys. Condens. Matter*, (2014), **26**, 255401
- [68] Chen J., Jung P., Hoffelner W., Ullmaier H., Dislocation loops and bubbles in oxide dispersion strengthened ferritic steel after helium implantation under stress, *Acta Mater.*, (2008), **56**, 250–258
- [69] He L., Yablinsky C., Gupta M., Gan J., Kirk M.A., Allen T.R., Transmission Electron Microscopy Investigation of Krypton Bubbles in Polycrystalline CeO₂, *Nucl. Technol.*, (2013), **182**, 164–169
- [70] Evans J.H., Mazey D.J., Evidence for solid krypton bubbles in copper, nickel and gold at 293K, *J. Phys. F Met. Phys.*, (1985), **15**, L1
- [71] Wei Q.M., Wang Y.Q., Nastasi M., Misra A., Nucleation and growth of bubbles in He ion-implanted V/Ag multilayers, *Philos. Mag.*, (2011), **91**, 553–573
- [72] Taylor C.A., Patel M.K., Aguiar J.A., Zhang Y., Crespillo M.L., Wen J., Xue H., Wang Y., Weber W.J., Bubble formation and lattice parameter changes resulting from He irradiation of defect-fluorite Gd₂Zr₂O₇, *Acta Mater.*, (2016), **115**, 115–122
- [73] Matsunaga J., Sakamoto K., Muta H., Yamanaka S., Dependence of vacancy concentration on morphology of helium bubbles in oxide ceramics, *J. Nucl. Sci. Technol.*, (2014), **51**, 1231–1240
- [74] Shen Q., Zhou W., Ran G., Li R., Feng Q., Li N., Evolution of Helium Bubbles and Discs in Irradiated 6H-SiC during Post-Implantation Annealing, *Materials*, (2017), **10**, 101
- [75] Sass S.L., Eyre B.L., Diffraction from void and bubble arrays in irradiated molybdenum, *Philos. Mag.*, (1973), **27**, 1447–1453

- [76] Mazey D.J., Evans J.H., Bubble lattice formation in titanium injected with krypton ions, *J. Nucl. Mater.*, (1986), **138**, 16–18
- [77] Harrison R.W., Greaves G., Hinks J.A., Donnelly S.E., Engineering self-organising helium bubble lattices in tungsten, *Sci. Rep.*, (2017), **7**, 7724
- [78] Hou M.D., Klaumünzer S., Schumacher G., Dimensional changes of metallic glasses during bombardment with fast heavy ions, *Phys. Rev. B*, (1990), **41**, 1144–1157
- [79] Klaumünzer S., Ion-beam-induced plastic deformation: A universal phenomenon in glasses, *Radiat. Eff. Defects Solids*, (1989), **110**, 79–83
- [80] Van Dillen T., De Dood M.J.A., Penninkhof J.J., Polman A., Roorda S., Vredenberg A.M., Ion beam-induced anisotropic plastic deformation of silicon microstructures, *Appl. Phys. Lett.*, (2004), **84**, 3591–3593
- [81] Dran J.C., Benyagoub A., Garrido F., Klaumünzer S., Dunlop A., Thomé L., Ion-beam induced plastic deformation in amorphous materials investigated by marker implantation and RBS, *Nucl. Inst. Methods Phys. Res. B*, (2002), **64**, 684–686
- [82] Zhang J., Lian J., Zhang F., Wang J., Fuentes A.F., Ewing R.C., Intrinsic Structural Disorder and Radiation Response of Nanocrystalline Gd₂(Ti_{0.65}Zr_{0.35})₂O₇ Pyrochlore, *J. Phys. Chem. C*, (2010), **114**, 11810–11815
- [83] Zhang J., Lian J., Fuentes A.F., Zhang F., Lang M., Lu F., Ewing R.C., Enhanced radiation resistance of nanocrystalline pyrochlore Gd₂(Ti_{0.65}Zr_{0.35})₂O₇, *Appl. Phys. Lett.*, (2009), **94**, 243110
- [84] Anantharaman K., Shivakumar V., Saha D., Utilisation of thorium in reactors, *J. Nucl. Mater.*, (2008), **383**, 119–121
- [85] Chen C.-F., Kelly J., Asphjell Ø., Papin P.A., Forsyth R.T., Guidry D.R., Safarik D.J., Llobet A., Processing of ThO₂/CeO₂ Ceramic Fuel, *J. Am. Ceram. Soc.*, (2014), **97**, 3062–3070
- [86] Garrido F., Nowicki L., Sattonnay G., Sauvage T., Thomé L., Lattice location of helium in uranium dioxide single crystals, *Nucl. Inst. Methods Phys. Res. B*, (2004), **219–220**, 196–199
- [87] Dabrowski L., Szuta M., Diffusion of helium in the perfect uranium and thorium dioxide single crystals, *Nukleonika*, (2013), **58**, 295–300
- [88] Yun Y., Eriksson O., Oppeneer P.M., First-principles modeling of He-clusters in UO₂, *J. Nucl. Mater.*, (2009), **385**, 72–74
- [89] Shao K., Han H., Zhang W., Wang C.Y., Guo Y.L., Ren C.L., Huai P., First-principles study of helium clustering at initial stage in ThO₂, *Chinese Phys. B*, (2017), **26**, 1–5
- [90] Roudil D., Deschanel X., Trocellier P., Jégou C., Peugeot S., Bart J.M., Helium thermal diffusion in a uranium dioxide matrix, *J. Nucl. Mater.*, (2004), **325**, 148–158

- [91] Lu Y., Yang Y., Zhang P., Thermodynamic properties and structural stability of thorium dioxide, *J. Phys. Condens. Matter*, (2012), **24**, 225801(1–10)
- [92] Grimes R.W., Miller R.H., Catlow C.R.A., The behaviour of helium in UO₂: Solution and migration energies, *J. Nucl. Mater.*, (1990), **172**, 123–125
- [93] Trocellier P., Agarwal S., Miro S., A review on helium mobility in inorganic materials, *J. Nucl. Mater.*, (2014), **445**, 128–142
- [94] Mohun R., Desgranges L., Léchelle J., Simon P., Guimbretière G., Canizarès A., Duval F., Jegou C., Magnin M., Clavier N., Dacheux N., Valot C., Vauchy R., Charged defects during alpha-irradiation of actinide oxides as revealed by Raman and luminescence spectroscopy, *Nucl. Inst. Methods Phys. Res. B*, (2016), **374**, 67–70
- [95] Runevall O., Sandberg N., Helium induced void and bubble formation in MgO, *Comput. Mater. Sci.*, (2012), **60**, 53–58
- [96] Gutierrez G., Peugeot S., Hinks J.A., Greaves G., Donnelly S.E., Oliviero E., Jégou C., Helium bubble formation in nuclear glass by in-situ TEM ion implantation, *J. Nucl. Mater.*, (2014), **452**, 565–568
- [97] Yang T., Huang X., Gao Y., Wang C., Zhang Y., Xue J., Yan S., Wang Y., Damage evolution of yttria-stabilized zirconia induced by He irradiation, *J. Nucl. Mater.*, (2012), **420**, 430–436
- [98] Odette G.R., Alinger M.J., Wirth B.D., Recent Developments in Irradiation-Resistant Steels, *Annu. Rev. Mater. Res.*, (2008), **38**, 471–503
- [99] Allen T., Busby J., Meyer M., Petti D., Materials challenges for nuclear systems, *Mater. Today*, (2010), **13**, 14–23
- [100] Zinkle S.J., Busby J.T., Structural materials for fission & fusion energy, *Mater. Today*, (2009), **12**, 12–19
- [101] Alinger M.J., Odette G.R., Hoelzer D.T., On the role of alloy composition and processing parameters in nanocluster formation and dispersion strengthening in nanostructured ferritic alloys, *Acta Mater.*, (2009), **57**, 392–406
- [102] El-Genk M.S., Tournier J.M., A review of refractory metal alloys and mechanically alloyed-oxide dispersion strengthened steels for space nuclear power systems, *J. Nucl. Mater.*, (2005), **340**, 93–112
- [103] Ukai S., Okada H., Inoue M., Nishida T., Fujiwara M., Nomura S., Shikakura S., Asabe K., Alloying design of oxide dispersion for long life FBRs core materials strengthened ferritic steel, *J. Nucl. Mater.*, (1993), **204**, 5–73
- [104] Jiang Y., Smith J.R., Robert Odette G., Prediction of structural, electronic and elastic properties of Y₂Ti₂O₇ and Y₂TiO₅, *Acta Mater.*, (2010), **58**, 1536–1543
- [105] Yamashita S., Ohtsuka S., Akasaka N., Ukai S., Ohnuki S., Formation of nanoscale complex oxide particles in mechanically alloyed ferritic steel, *Philos. Mag. Lett.*, (2004), **84**, 525–529

- [106] Klimiankou M., Lindau R., Möslang A., Energy-filtered TEM imaging and EELS study of ODS particles and Argon-filled cavities in ferritic-martensitic steels, *Micron*, (2005), **36**, 1–8
- [107] Sakasegawa H., Legendre F., Boulanger L., Brocq M., Chaffron L., Cozzika T., Malaplate J., Henry J., de Carlan Y., Stability of non-stoichiometric clusters in the MA957 ODS ferritic alloy, *J. Nucl. Mater.*, (2011), **417**, 229–232
- [108] Wu Y., Haney E.M., Cunningham N.J., Odette G.R., Transmission electron microscopy characterization of the nanofeatures in nanostructured ferritic alloy MA957, *Acta Mater.*, (2012), **60**, 3456–3468
- [109] London A.J., Santra S., Amirthapandian S., Panigrahi B.K., Sarguna R.M., Balaji S., Vijay R., Sundar C.S., Lozano-Perez S., Grovenor C.R.M., Effect of Ti and Cr on dispersion, structure and composition of oxide nano-particles in model ODS alloys, *Acta Mater.*, (2015), **97**, 223–233
- [110] London A.J., Lozano-Perez S., Santra S., Amirthapandian S., Panigrahi B.K., Sundar C.S., Grovenor C.R.M., Comparison of atom probe tomography and transmission electron microscopy analysis of oxide dispersion strengthened steels, *J. Phys. Conf. Ser.*, (2014), **522**, 012028
- [111] Ravi C., Thermodynamic stability of oxide phases of Fe-Cr based ODS steels via quantum mechanical calculations, *Procedia Eng.*, (2014), **86**, 788–798
- [112] Lian J., Wang L., Chen J., Sun K., Ewing R.C., Farmer J.M., Boatner L.A., The order-disorder transition in ion-irradiated pyrochlore, *Acta Mater.*, (2003), **51**, 1493–1502
- [113] Lian J., Chen J., Wang L.M., Ewing R.C., Farmer J.M., Boatner L.A., Helean K.B., Radiation-induced amorphization of rare-earth titanate pyrochlores, *Phys. Rev. B*, (2003), **68**, 134107
- [114] Zhang J., Zhang F., Lang M., Lu F., Lian J., Ewing R.C., Ion-irradiation-induced structural transitions in orthorhombic Ln_2TiO_5 , *Acta Mater.*, (2013), **61**, 4191–4199
- [115] Kuramoto K., Mitamura H., Banba T., Muraoka S., Development of ceramic waste forms for actinide-rich waste - Radiation stability of perovskite and phase and chemical stabilities of ZR-and AL-based ceramics, *Prog. Nucl. Energy*, (1998), **32**, 509–516
- [116] Mesko M.G., Bunker B.C., Day D.E., Immobilization of High-level Radioactive Sludges in Iron Phosphate Glasses, In: Science and Technology for Disposal of Radioactive Tank Wastes, *Springer US*, (1998)
- [117] Day D.E., Wu Z., Ray C.S., Hrma P., Chemically durable iron phosphate glass wasteforms, *J. Non. Cryst. Solids*, (1998), **241**, 1–12
- [118] Joseph K., Govindan Kutty K. V., Chandramohan P., Vasudeva Rao P.R., Studies on the synthesis and characterization of cesium-containing iron phosphate glasses, *J. Nucl. Mater.*, (2009), **384**, 262–267

- [119] Perez Jr J.M., Bickford D.F., Day D.E., Kim D.S., Lambert S.L., Marra S.L., Peeler D.K., Strachan D.M., Triplett M.B., Vienna J.D., others, Pacific Northwest National Laboratory Report, (2001), PNNL-13582
- [120] Day D.E., Ray C.S., Marasinghe K., Karabulut M., Fang X., An alternative host matrix based on iron phosphate glasses for the vitrification of specialized nuclear waste forms, (2000)
- [121] Kim C.W., Day D.E., Immobilization of Hanford LAW in iron phosphate glasses, *J. Non. Cryst. Solids*, (2003), **331**, 20–31
- [122] Day D.E., Ray C.S., Kim C.W., Final report: Iron Phosphate Glasses: an alternative for vitrifying certain nuclear wastes, *Rep. No. DEFG07 E96ER45618*, (2004)
- [123] Ojovan M.I., Lee W.E., Glassy wastefoms for nuclear waste immobilization, *Metall. Mater. Trans. A*, (2011), **42**, 837–851
- [124] Weber W.J., Ewing R.C., Angell C.A., Arnold G.W., Cormack A.N., Delaye J.M., Griscom D.L., Hobbs L.W., Navrotsky A., Price D.L., Stoneham A.M., Weinberg M.C., Radiation Effects in Glasses Used for Immobilization of High-level Waste and Plutonium Disposition, *J. Mater. Res.*, (1997), **12**, 1948–1978
- [125] Bingham P.A., Hand R.J., Hannant O.M., Forder S.D., Kilcoyne S.H., Effects of modifier additions on the thermal properties, chemical durability, oxidation state and structure of iron phosphate glasses, *J. Non. Cryst. Solids*, (2009), **355**, 1526–1538
- [126] Fang X., Ray C.S., Mogaš-Milanković A., Day D.E., Iron redox equilibrium, structure and properties of iron phosphate glasses, *J. Non. Cryst. Solids*, (2001), **283**, 162–172
- [127] Karabulut M., Marasinghe G.K., Ray C.S., Day D.E., Ozturk O., Waddill G.D., X-ray photoelectron and Mössbauer spectroscopic studies of iron phosphate glasses containing U, Cs and Bi, *J. Non. Cryst. Solids*, (1999), **249**, 106–116
- [128] Sun K., Ding T., Wang L.M., Ewing R.C., Radiation-Induced Nanostructures in an Iron Phosphate Glass, *MRS Proc.*, (2003), **792**, R3.21
- [129] Awazu K., Roorda S., Brebner J.L., Ishii S., Shima K., Structure of Latent Tracks Created by Swift Heavy Ions in Amorphous SiO₂ and Zinc Phosphate Glass, *Jpn. J. Appl. Phys.*, (2003), **42**, 3950–3957
- [130] Savchenko P.S., The nature of eutectics, *Russ J Inorg Chem*, (1959), **4**, 186–189
- [131] Wang S.X., Wang L.M., Ewing R.C., Govindan Kutty K.V., Ion irradiation of rare-earth- and yttrium-titanate-pyrochlores, *Nucl. Inst. Methods Phys. Res. B*, (2000), **169**, 135–140
- [132] Mumme W.G., Wadsley A.D., The structure of orthorhombic Y₂TiO₅, an example of mixed seven- and fivefold coordination, *Acta Crystallogr. Sect. B Struct. Crystallogr. Cryst. Chem.*, (1968), **24**, 1327–1333

- [133] Deganello F., Marci G., Deganello G., Citrate-nitrate auto-combustion synthesis of perovskite-type nanopowders: A systematic approach, *J. Eur. Ceram. Soc.*, (2009), **29**, 439–450
- [134] Aruna S.T., Mukasyan A.S., Combustion synthesis and nanomaterials, *Curr. Opin. Solid State Mater. Sci.*, (2008), **12**, 44–50
- [135] Levashov E.A., Mukasyan A.S., Rogachev A.S., Shtansky D.V., Self-propagating high-temperature synthesis of advanced materials and coatings, *Int. Mater. Rev.*, (2017), **62**, 203–239
- [136] Marinšek M., Zupan K., Maèek J., Ni–YSZ cermet anodes prepared by citrate/nitrate combustion synthesis, *J. Power Sources*, (2002), **106**, 178–188
- [137] Sanjay Kumar D., Ananthasivan K., Venkata Krishnan R., Amirthapandian S., Dasgupta A., Studies on the synthesis of nanocrystalline Y₂O₃ and ThO₂ through volume combustion and their sintering, *J. Nucl. Mater.*, (2016), **479**, 585–592
- [138] Murugasen P., Sagadevan S., Shajan D., Preparation, techniques and tools used for investigating glasses: An overview, *Int. J. Chem. Sci.*, (2015), **13**, 693–713
- [139] Jeol, Glossary of TEM terms, n.d.
- [140] Poswal A.K., Agrawal A., Yadav A.K., Nayak C., Basu S., Kane S.R., Garg C.K., Bhattachryya D., Jha S.N., Sahoo N.K., Commissioning and first results of scanning type EXAFS beamline (BL-09) at INDUS-2 synchrotron source, In: (2014), 649–651
- [141] Egerton R.F., Electron energy-loss spectroscopy in the TEM, *Reports Prog. Phys.*, (2009), **72**, 16502
- [142] Williams David B., Barry Carter C., Transmission Electron Microscopy: A Textbook for Materials Science, *Springer US*, (2009)
- [143] Perdew J.P., Kurth S., Density Functionals for Non-relativistic Coulomb Systems in the New Century, *Springer-Verlag, Berlin Heidelberg*, (2003)
- [144] Perdew J.P., Yue W., Accurate and simple density functional for the electronic exchange energy: Generalized gradient approximation, *Phys. Rev. B*, (1986), **33**, 8800–8802
- [145] Perdew J.P., Burke K., Ernzerhof M., Generalized Gradient Approximation Made Simple, *Phys. Rev. Lett.*, (1996), **77**, 3865–3868
- [146] Clark S.J., Segall M.D., Pickard C.J., Hasnip P.J., Probert M.I.J., Refson K., Payne M.C., First principles methods using CASTEP, *Zeitschrift Für Krist. - Cryst. Mater.*, (2005), **220**, 567–570
- [147] CASTEP Guide, *Materials Studio*, (2014), 1–219
- [148] Birch F., Finite Elastic Strain of Cubic Crystals, *Phys. Rev.*, (1947), **71**, 809–824
- [149] Groot F. De, Multiplet effects in X-ray spectroscopy, *Coord. Chem. Rev.*, (2005), **249**, 31–63

- [150] Thole B.T., Van Der Laan G., Butler P.H., Spin-mixed ground state of Fe phthalocyanine and the temperature-dependent branching ratio in X-ray absorption spectroscopy, *Chem. Phys. Lett.*, (1988)
- [151] Xiao H.Y., Zhang Y., Weber W.J., Ab initio molecular dynamics simulations of low-energy recoil events in ThO₂, CeO₂, and ZrO₂, *Phys. Rev. B*, (2012), **86**, 054109
- [152] Kresse G., Furthmüller J., Efficient iterative schemes for ab initio total-energy calculations using a plane-wave basis set, *Phys. Rev. B*, (1996), **54**, 11169–11186
- [153] Wang B.-T., Shi H., Li W.-D., Zhang P., First-principles study of ground-state properties and high pressure behavior of ThO₂, *J. Nucl. Mater.*, (2010), **399**, 181–188
- [154] Monkhorst H.J., Pack J.D., Special points for Brillouin-zone integrations, *Phys. Rev. B*, (1976), **13**, 5188–5192
- [155] Tracy C.L., Lang M., Pray J.M., Zhang F., Popov D., Park C., Trautmann C., Bender M., Severin D., Skuratov V.A., Ewing R.C., Redox response of actinide materials to highly ionizing radiation, *Nat. Commun.*, (2015), **6**, 6133
- [156] Tracy C.L., McLain Pray J., Lang M., Popov D., Park C., Trautmann C., Ewing R.C., Defect accumulation in ThO₂ irradiated with swift heavy ions, *Nucl. Inst. Methods Phys. Res. B*, (2014), **326**, 169–173
- [157] AKABORI M., FUKUDA K., Effect of Additives on Irradiation-Induced Change of Lattice Parameter in ThO₂, *J. Nucl. Sci. Technol.*, (1991), **28**, 841–847
- [158] Ando K., Oishi Y., Hidaka Y., Self-diffusion of oxygen in single crystal thorium oxide, *J. Chem. Phys.*, (1976), **65**, 2751–2755
- [159] Xiao H.Y., Zhang Y., Weber W.J., Stability and migration of charged oxygen interstitials in ThO₂ and CeO₂, *Acta Mater.*, (2013), **61**, 7639–7645
- [160] Xiao H.Y., Zhang Y., Weber W.J., Trapping and diffusion of fission products in ThO₂ and CeO₂, *J. Nucl. Mater.*, (2011), **414**, 464–470
- [161] Garner F.A., Radiation Damage in Austenitic Steels, In: Comprehensive Nuclear Materials, *Elsevier*, (2012), 33–95
- [162] Charint I., Murty K.L., Structural materials issues for the next generation fission reactors, *J. Oper. Manag.*, (2010), **62**, 67–74
- [163] Hirata A., Fujita T., Wen Y.R., Schneibel J.H., Liu C.T., Chen M.W., Atomic structure of nanoclusters in oxide-dispersion-strengthened steels, *Nat. Mater.*, (2011), **10**, 922–926
- [164] Wang S.X., Wang L.M., Ewing R.C., Irradiation-induced amorphization: Effects of temperature, ion mass, cascade size, and dose rate, *Phys. Rev. B*, (2001), **63**, 1–8
- [165] Weber W.J., Models and mechanisms of irradiation-induced amorphization in ceramics, *Nucl. Inst. Methods Phys. Res. B*, (2000), **166–167**, 98–106

- [166] Ikeno H., de Groot F.M.F., Stavitski E., Tanaka I., Multiplet calculations of L(2,3) x-ray absorption near-edge structures for 3d transition-metal compounds., *J. Phys. Condens. Matter*, (2009), **21**, 104208
- [167] Miedema P.S., Ikeno H., De Groot F.M.F., First principles multiplet calculations of the calcium L23 x-ray absorption spectra of CaO and CaF₂, *J. Phys. Condens. Matter*, (2011), **23**, 145501
- [168] Stavitski E., de Groot F.M.F., The CTM4XAS program for EELS and XAS spectral shape analysis of transition metal L edges, *Micron*, (2010), **41**, 687–694
- [169] Gao S.-P., Pickard C.J., Perlov A., Milman V., Core-level spectroscopy calculation and the plane wave pseudopotential method., *J. Phys. Condens. Matter*, (2009), **21**, 104203
- [170] Kotani A., Ogasawara H., Interplay between intra-atomic multiplet coupling and interatomic hybridization in core-level spectroscopy, *J. Electron Spectrosc. Relat. Phenom.*, (1997), **86**, 65–72
- [171] Grayson S., Theoretical simulation of resonant inelastic X-ray scattering in transition metal oxides, Trinity College, Dublin, (2012)
- [172] Stavitski E., de Groot F.M.F., CTM4XAS 5.2 Manual, Version 1, (2008)
- [173] Ungár T., Microstructural parameters from X-ray diffraction peak broadening, *Scripta Mater.*, (2004), **51**, 777–781
- [174] Li R., Lu S., Kim D., Schönecker S., Zhao J., Kwon S.K., Vitos L., Stacking fault energy of face-centered cubic metals: thermodynamic and ab initio approaches, *J. Phys. Condens. Matter*, (2016), **28**, 395001
- [175] Schramm R.E., Reed R.P., Stacking fault energies of seven commercial austenitic stainless steels, *Metall. Trans. A*, (1975), **6**, 1345–1351
- [176] Glerup M., Nielsen O.F., Poulsen F.W., The Structural Transformation from the Pyrochlore Structure, A₂B₂O₇, to the Fluorite Structure, AO₂, Studied by Raman Spectroscopy and Defect Chemistry Modeling, *J. Solid State Chem.*, (2001), **160**, 25–32
- [177] Johnson M.B., James D.D., Bourque A., Dabkowska H.A., Gaulin B.D., White M.A., Thermal properties of the pyrochlore, Y₂Ti₂O₇, *J. Solid State Chem.*, (2009), **182**, 725–729
- [178] Chernyshev V.A., Petrov V.P., Nikiforov A.E., Phonon spectra of YTiO₃ and Y₂Ti₂O₇: Ab initio calculations, *Opt. Spectrosc.*, (2014), **116**, 864–867
- [179] Paques-Ledent M.T., Infrared and Raman studies of M₂TiO₅ compounds (M = rare earths and Y): Isotopic effect and group theoretical analysis, *Spectrochim Acta. A*, (1976), **32**, 1339–1344
- [180] Xu Y.-N., Gu Z., Ching W., Electronic, structural, and optical properties of crystalline yttria, *Phys. Rev. B*, (1997), **56**, 14993–15000

- [181] Ching W.Y., Xu Y.-N., Electronic and optical properties of yttria, *Phys. Rev. Lett.*, (1990), **65**, 895–898
- [182] Shang-Di Mo, Ching W.Y., Electronic and optical properties of three phases of titanium dioxide: Rutile, anatase, and brookite, *Phys. Rev. B*, (1995), **51**, 13023–13032
- [183] Jiang B., Zuo J.M., Jiang N., Keeffe M.O., Spence J.C.H., Charge density and chemical bonding in rutile, TiO₂, *Acta Crystallogr. Sect. A*, (2003), **59**, 341–350
- [184] Zhang J., Visinoiu A., Heyroth F., Syrowatka F., Alexe M., Hesse D., Leipner H.S., High-resolution electron energy-loss spectroscopy of Ba, *Phys. Rev. B*, (2005), **71**, 064108
- [185] Kucheyev S.O., van Buuren T., Baumann T.F., Satcher J.H., Willey T.M., Meulenberg R.W., Felter T.E., Poco J.F., Gammon S.A., Terminello L.J., Electronic structure of titania aerogels from soft x-ray absorption spectroscopy, *Phys. Rev. B*, (2004), **69**, 245102
- [186] Van Aken P.A., Liebscher B., Styrsa V.J., Core level electron energy-loss spectra of minerals: pre-edge fine structures at the oxygen K-edge, *Phys. Chem. Miner.*, (1998), **25**, 494–498
- [187] Minasian S.G., Keith J.M., Batista E.R., Boland K.S., Bradley J.A., Daly S.R., *et al.*, Covalency in metal-oxygen multiple bonds evaluated using oxygen K-edge spectroscopy and electronic structure theory, *J. Am. Chem. Soc.*, (2013), **135**, 1864–1871
- [188] De Groot F.M.F., Grioni M., Fuggle J.C., Ghijsen J., Sawatzky G.A., Petersen H., Oxygen 1s X-ray-absorption edges of transition-metal oxides, *Phys. Rev. B*, (1989), **40**, 5715–5723
- [189] Anisimov V.I., Solovyev I. V., Korotin M.A., Czyżyk M.T., Sawatzky G.A., Density-functional theory and NiO photoemission spectra, *Phys. Rev. B*, (1993), **48**, 16929–16934
- [190] Morgan B.J., Watson G.W., Polaronic trapping of electrons and holes by native defects in anatase TiO₂, *Phys. Rev. B*, (2009), **80**, 233102
- [191] Segall M.D., Shah R., Pickard C.J., Payne M.C., Population analysis of plane-wave electronic structure calculations of bulk materials, *Phys. Rev. B*, (1996), **54**, 16317–16320
- [192] Srivastava A.M., Brik M.G., Comparative ab initio study of electronic, optical and chemical bonding properties of pyrochlores, Y₂B₂O₇ (B=Ti⁴⁺, Sn⁴⁺), *J. Lumin.*, (2010), **130**, 2368–2376
- [193] Demortière A., Leonard D.N., Petkov V., Chapman K., Chattopadhyay S., She C., Cullen D.A., Shibata T., Pelton M., Shevchenko E. V., Strain-Driven Stacking Faults in CdSe/CdS Core/Shell Nanorods, *J. Phys. Chem. Lett.*, (2018), **9**, 1900–1906

- [194] Dholakia M., Chandra S., Mathi Jaya S., A comparative study of topology and local disorder in Y₂O₃, Y₂TiO₅, and Y₂Ti₂O₇ crystals, *J. Appl. Phys.*, (2019), **125**, 025104
- [195] Zachariasen W.H., The atomic arrangement in glass, *J. Am. Chem. Soc.*, (1932), **54**, 3841–3851
- [196] Joseph K., Asuvathraman R., Venkata Krishnan R., Ravindran T.R., Govindaraj R., Govindan Kutty K. V., Vasudeva Rao P.R., Iron phosphate glass containing simulated fast reactor waste: Characterization and comparison with pristine iron phosphate glass, *J. Nucl. Mater.*, (2014), **452**, 273–280
- [197] Doupovec J., Sitek J., Kákoš J., Crystallization of iron phosphate glasses, *J. Therm. Anal.*, (1981), **22**, 213–219
- [198] Almeida F.J.M., Martinelli J.R., Partiti C.S.M., Characterization of iron phosphate glasses prepared by microwave heating, *J. Non. Cryst. Solids*, (2007), **353**, 4783–4791
- [199] Zhang L., Schlesinger M.E., Brow R.K., Phase Equilibria in the Fe₂O₃-P₂O₅ System, *J. Am. Ceram. Soc.*, (2011), **94**, 1605–1610
- [200] Joseph K., Ghosh S., Govindan Kutty K. V., Vasudeva Rao P.R., Crystallization kinetics, stability and glass forming ability of iron phosphate and cesium loaded iron phosphate glasses, *J. Nucl. Mater.*, (2012), **426**, 233–239
- [201] Ziegler J.F., Biersack J.P., The Stopping and Range of Ions in Matter, In: Treatise on Heavy-Ion Science, *Springer US, Boston, MA*, (1985), 93–129
- [202] Ziegler J.F., The stopping and range of ions in matter, (2013)
- [203] Joseph K., Jolley K., Smith R., Iron phosphate glasses: Structure determination and displacement energy thresholds, using a fixed charge potential model, *J. Non. Cryst. Solids*, (2015), **411**, 137–144
- [204] Carl P., Radial Profile (Extended) Tool for ImageJ, (2017)
- [205] Colliex C., Manoubi T., Ortiz C., Electron-energy-loss-spectroscopy near-edge fine structures in the iron-oxygen system, *Phys. Rev. B*, (1991), **44**, 11402–11411
- [206] van Aken P.A., Liebscher B., Styrsa V.J., Quantitative determination of iron oxidation states in minerals using Fe L 2,3 -edge electron energy-loss near-edge structure spectroscopy, *Phys. Chem. Miner.*, (1998), **25**, 323–327
- [207] Joseph K., Venkata Krishnan R., Govindan Kutty K.V., Vasudeva Rao P.R., Kinetics of nonisothermal crystallization of Cs₂O–Fe₂O₃–P₂O₅ glasses, *Thermochim. Acta*, (2011), **512**, 67–70
- [208] Carter J., Fu E.G., Martin M., Xie G., Zhang X., Wang Y.Q., Wijesundera D., Wang X.M., Chu W.-K., Shao L., Effects of Cu ion irradiation in Cu₅₀Zr₄₅Ti₅ metallic glass, *Scripta Mater.*, (2009), **61**, 265–268

- [209] Toulemonde M., Dufour C., Paumier E., Transient thermal process after a high-energy heavy-ion irradiation of amorphous metals and semiconductors, *Phys. Rev. B*, (1992), **46**, 14362–14369
- [210] Katakam S., Santhanakrishnan S., Vora H., Hwang J.Y., Banerjee R., Dahotre N.B., Stress-induced selective nano-crystallization in laser-processed amorphous Fe–Si–B alloys, *Philos. Mag. Lett.*, (2012), **92**, 617–624
- [211] Matthews D.T.A., Ocelik V., Bronsveld P.M., De Hosson J.T.M., An electron microscopy appraisal of tensile fracture in metallic glasses, *Acta Mater.*, (2008), **56**, 1762–1773
- [212] Rouxel T., Elastic Properties and Short-to Medium-Range Order in Glasses, *J. Am. Ceram. Soc.*, (2007), **90**, 3019–3039
- [213] Narottam P.B., Doremus R.H., Handbook of Glass Properties, *Elsevier*, (1986)
- [214] Huang W., Day D.E., Ray C.S., Kim C.W., High temperature properties of an iron phosphate melt containing high chrome nuclear waste, *J. Nucl. Mater.*, (2005), **346**, 298–305